Studies on Highly Localized Excitation of PbS Quantum Dots on Metal Nanostructures

金属ナノ構造上における PbS 量子ドットの
局在励起に関する研究

Xiaowei Li

Graduate School of Chemical Sciences and Engineering
Hokkaido University

2016

Contents

Chapter 1

General Introduction

Photoelectrochemistry, the conversion of sunlight to electrical or chemical (redox) energy, is a promising technology to feasibly solve the energy problem that the global world faces in the future. Since the discovery of photovoltaic phenomenon performed by Becquerel in 1839,[1] and was well understood until Brattain and Garrett launched the modern era of photoelectrochemistry in 1954,[2] the system of semiconductor materials of controlled impurity content contacting electrolyte exposed to light has been attracted tremendous interest and attained continuous development. Worldwide photovoltaic capacity has been reached to 227 GW in 2015, enormously exceeding 2.6 GW in 2004.[3] And the direct production of electric fuels by utilizing solar energy, for example, the conversion of abundant materials of H_2O or CO_2 to fuels of H_2 or CH_3OH, is considered to possess promoted competitiveness with fossil fuel. However, limitations such as high cost, inadequate sunlight absorption and boundary of conversion efficiency remain to be solved for universal applications.

At present, crystalline silicon wafers with thickness around 180 ~ 300 μm occupy most of the solar-cell market and the major cost results from the silicon materials and processing. Therefore, thin-film solar cells in scales of several micrometers or hundred nanometers that can be deposited on cheap module-sized substrates such as glass or plastic are considered to have advantage, especially for scarce materials such as In and Te with small quantities in Earth's crust. In addition, a variety of semiconductors such as GaAs and CdTe have been exploited, but the small absorbance of near-bandgap light limit their application. And as visible light (400 to 700 nm) possess a large percentage in sunlight at Earth's surface with relatively high irradiance than infrared or ultraviolet light, techniques that advance efficient visible light trapping inside thin-film solar cells enjoys considerable advantages. The sensitization of solar cells by diverse dye molecules (DSSC) is a technically and economically credible alternative concept to present day p–n junction photovoltaic devices,[4] but the temperature stability of liquid electrolyte as well as costly ruthenium still ask for improved design for thin-film solar cells.

Owing to quantum confinement, colloid semiconductor quantum dots (CSQDs) enjoy a

considerable advantage of tunable electronic and optical properties with variation in size, shape and composition though diverse synthetic techniques,[5-7] so that CSQDs recently have been investigated as sensitizer for thin-film solar cells thanks to their high light absorption cross sections as well as enhanced stability compared with conventional dyes. Recent research hotspots have been focused on multiple exciton generation of narrow bandgap CSQDs, which is a process that a high energy photon excites more than two pairs of electrons or holes in semiconductor and credibly exceed the Shockley-Queisser limit of ~33% by traditional photoenergy devices.[8-11]

Another encouraging approach to enhance photon trapping is the metallic nanostructure supporting localized surface plasmonic resonance (LSPR). The noble metal's free electrons strongly oscillate in phase with the varying electric field of the incident light, giving rise to an intensive local electric field, which powers the excitation of more electrons and holes[12] and consequently break a limit of photoenergy conversion via changing photoenergy localization by simply changing the structure of the metal at the nanometer scale.[13, 14]

1.1 Semiconductor quantum dots

The investigation of materials at the nano-scale has gained a great deal of interest as it fills the gap between bulk and atoms or molecules, thus improving our understanding of fundamental chemical and physical properties and advancing new applications related to photon absorption such as photoenergy conversion, diode emitter and molecular detection. Lead chalcogenide CSQDs enjoys the advantage of narrow bandgap energy, e.g. 0.41 eV for lead sulfide (PbS) QDs, so that quantum confinement and/or multiple exciton generation can be easily obtained and sensibly they can be adapted to match the bandgap value of TiO_2 which is ideal for a single junction solar quantum converter.[15]

1.1.1 Fundamental concepts related to CSQDs

Properties of bulk PbS

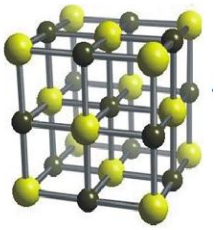

Figure 1.1 Rock salt

Bulk PbS is a compound that has a rock salt structure with a lattice constant a = 5.936 Å, as shown in Figure 1.1. It is available in nature in a highly symmetrical crystallized form. Pb^{2+} and S^{2-} ions occupy the lattice sites in the rock-salt crystal structure alternatively.[16] Each Pb atom is surrounded by 6 atoms of S, which are arranged at the corners of the surrounding octahedron and viceversa. The Bravais lattice has an fcc Brillouin zone with a Pb ion at (0 0 0) and a S ion at (½ ½ ½).

Quantum confinement

When the radius of the nanoparticle (NP) is smaller than the exciton Bohr radius (R_{ex}, as given in Eq.1), the nanoparticle behaves as quantum dots and exhibit quantum-confinement effects, that is the continuous energy spectrum becomes discrete, the bandgap increases, and thus nonlinear optical properties are expected to be greatly enhanced, as Figure 1.2 illustrated.

$$R_{ex} = \frac{h^2 \varepsilon}{e^2}\left(\frac{1}{m_e} + \frac{1}{m_h}\right) \quad (1)$$

Where h is the Planck's constant, ε is the bulk optical dielectric constant, e is the electron charge, and m_e and m_h are respectively the effective masses of the electron and hole.

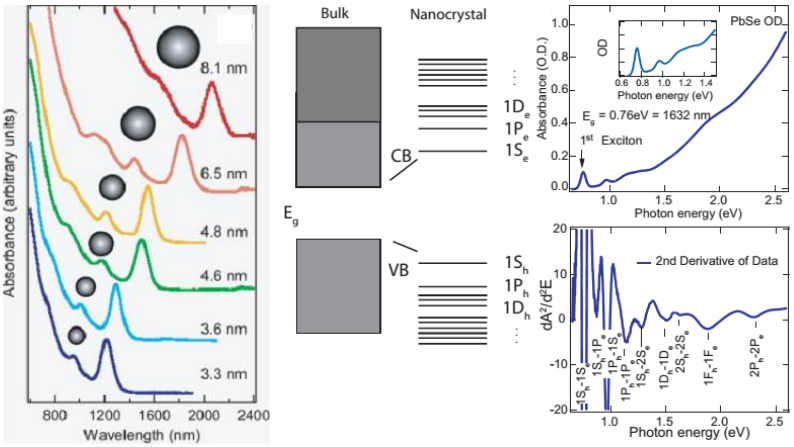

Figure 1. 2. (Left) Linear absorption spectra of a series of PbSe QDs with series average diameter. Strong excitonic absorption and a blue-shift of the onset are signatures of quantum confinement in NCs. (Middle) In NCs the quantum confinement produces discrete states in the conduction and valence bands. (Right) Transitions between these states can be seen in the absorption spectrum.[17]

As the key properties of bulk PbS and CdS[18] summarized in Table 1.1, PbS has a relatively larger dielectric constant, comparable and smaller electron and hole effective masses, which leads to a larger exciton Bohr radius of exciton (R_{ex} = 18 nm) than that of CdS (R_{ex} = 3 nm), and a strong regime of confinement where both electrons and holes are more easily confined in PbS QDs.

Table.1.1 Electronic properties of bulk PbS and CdS

	Band gap	Effective mass		Static dielectric constant	Bohr radius
	E_g(300 K) eV	m_e	m_h	ε_r	R_{ex} nm
PbS	0.41	~0.1m_0	0.1m_0	170	18
CdS	2.53	0.2m_0	0.7m_0 (⊥), 5m_0(∥)	8.9	3

m_0 is the electron mass in vacuum.

In addition, PbS with a bulk bandgap of 0.41 eV at 300 K, quite smaller than that of CdS (2.53 eV), presents excellent size tenability across the near infrared region, and PbS QDs with size variation are easily prepared with inexpensive and relatively safe synthesis. The combination of the large exciton Bohr radius and the narrow band gap leads to large confinement energies for carriers and hence to an absorption edge at energies much larger than that of bulk PbS. Thus modifying the band gap of QDs opens up possibilities for even a wider range of applications.

Determination of QDs energy levels

Taken the effect of non-parabolicity of the conduction and valence bands into account, hyperbolic model achieved a better agreement between the measured and calculated dependence of the energy of the electron-hole recombination (E_g(QD)) on the QD diameter (R) for nanoparticles,[19] as written in the following equation.

$$E_g(\mathrm{QD}) = \sqrt{E_g{}^2(\mathrm{bulk}) + \frac{h^2 E_g(\mathrm{bulk})}{2\mu R^2}} \qquad (2)$$

Where $\mu = m_e m_h/(m_e+m_h)$ is the exciton reduced mass, R is the quantum dot radius, h is the Planck

constant.

The change in quantum confinement imparted by reducing the QD size serves to raise the conduction band edge (CB), thus potentially increasing injection yields. The CB energy of QDs can be estimated using the following zeroth-order approximation of the effective-mass model:[20]

$$E_{\mathrm{CB}}(\mathrm{QD}) = E_{\mathrm{CB}}(\mathrm{bulk}) + (E_g(\mathrm{QD}) - E_g(\mathrm{bulk})(\frac{m_h}{m_e + m_h}) \quad (3)$$

Where E_{CB} is the conduction band energy (versus vacuum), E_{g} is the bandgap, and m_{h} and m_{e} are the effective hole and electron masses in the bulk semiconductor. As m_{e} of PbS is relatively small than m_{h}, shift of E_{CB} is consequently larger than E_{VB}.

Colloidal QDs

Since the percentage of surface atoms can be very high in small QDs, the dangling bonds formed by the excess ion on the nanocrystals surface may lead to the formation of additional states inside the band gap of QD, affecting the electrical and optical properties. Thus the surface of a QD has to be passivated with a larger band gap organic or inorganic material,[21] as presented in Figure 1.3.

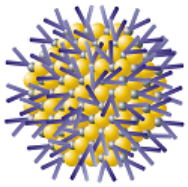

Figure 1.3. A schematic of a single colloidal QD with its surrounding

In complement to the control over the QD bandgap by tune the nanocrystal size, the electronic properties of colloidal QD can also be tuned through modification of the QD surface chemistry via ligand exchange.[22, 23] Choosing a suitable capping agent assists the functionalization of the QDs, their solubilization in aquatic electrolyte and enhances carrier confinement. A wide variety of ligand chemistries have been utilized for PbS QDs, including thiols,[24] carboxylic acids,[25] primary amines,[26] halide ions,[27] inorganic shells,[5, 28] oligomeric alkyl phosphine[29] or a hybrid passivation.[30]

1.1.2 Multiple excitation generation (MEG)

Shockley and Queisser calculated that the maximum solar to electrical energy conversion efficiency for single band gap (E_g) semiconductor absorber to be 31%,[31] based on the assumption that only one band edge electronic excited state can be generated per absorbed photon, with all photon energy (E_{hv}) in excess of the band gap energy being dissipated as heat. This limitation has been shown to be accurate in bulk inorganic semiconductors in where carrier thermalization plays a major role;[32] but in semiconductor nanostructures, an increased efficiency of 45%[33] can be achieved because of the electronic structure associated with carrier confinement in three dimensions through a process which called multiple exciton generation (MEG) (or carrier multiplication, CM): based on the impact ionization (II) mechanism, an inverse Auger process, photogenerated carriers with excess energy greater than the energy gap can create secondary electron-hole pairs via impact ionization of the filled band, as shown in Figure 1.4. Through this process, two (or more) electron-hole pairs are collected from each photon instead of just one. Optical measurements of various nanomaterial systems have identified signatures of MEG, including single-walled carbon nanotubes (SWCNT)[34] as well as quantum dots (QDs) or QD thin film of CdSe,[35] InAs[36] and Si.[37] Narrow bandgap semiconductors, especially lead chalcogenide, have been attracted huge interest in MEG for improving photovoltaic device performance via multiple-exciton generation or multiple-exciton collection effects.[9, 10, 38-42]

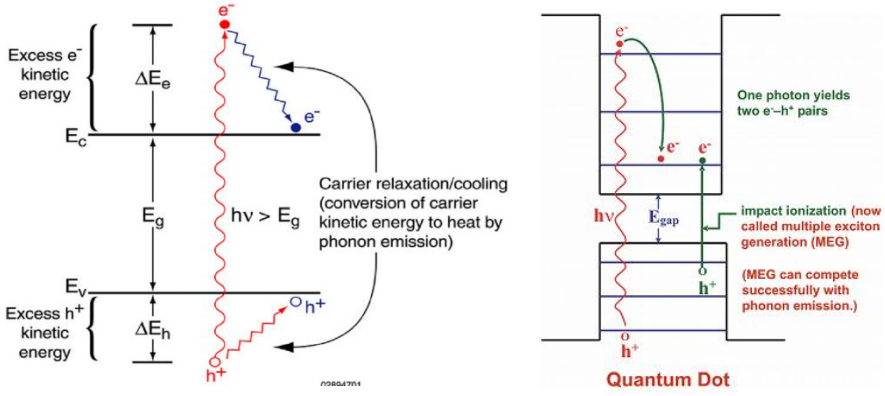

Figure 1.4. (Left) Hot carrier relaxation/cooling in semiconductors.[43] (Right) Enhanced photovoltaic efficiency in QD solar cells by impact ionization.[44]

In bulk semiconductor, besides in compliance with the energy conservation, impact ionization also requires the momentum to be conserved, pertaining to both the electron-hole pair photogeneration and

impact ionization process within the electronic band structure, thus consequently elevate the photon energy threshold for MEG above the simple $2E_g$ level. While in quantized nanocrystal, especially three-dimensional (3D) spatial confined quantum dots (QDs), decline in energy to overcome a threshold for MEG is available because of relaxed momentum conservation and suppressed cooling by phonon emission due to the phonon bottleneck which originates from the mismatch between the electronic gaps and phonon frequencies in the presence of sparse electronic structure. Figure 1.5 gives an example of size-dependent quantum efficiency and MEG threshold of bulk and quantized PbS measured via transient absorption in pump-probe experiments,[45] showing decreased threshold of MEG for PbS QDs with relative small diameter.

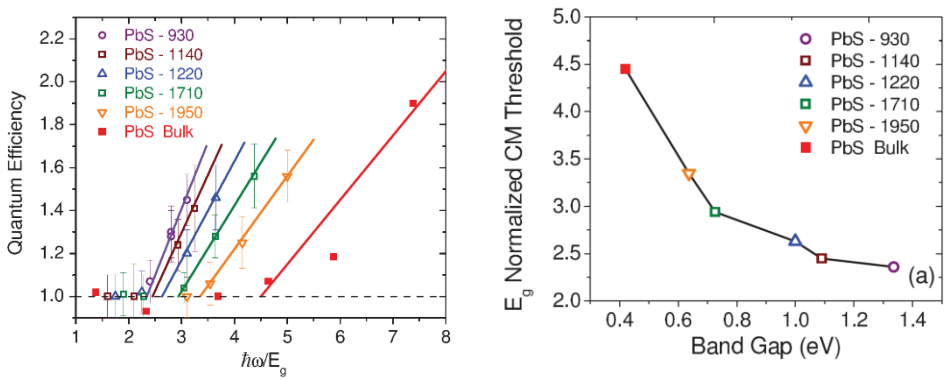

Figure 1.5. (Left) Spectral dependence of the carrier multiplication for five different sizes of PbS QDs compared to bulk PbS. (Right) Carrier-multiplication energy threshold (a) normalized by the sample band gap.

1.1.3 Transition measurements related to PbS QDs

There have been several different types of spectroscopic measurements: transient (pump-probe) absorption (TA) spectroscopy is to monitor the intraband transitions (e.g. $1S_e$-$1P_e$) of the newly created excitons in the mid-IR, time-resolved photoluminescence (TRPL) to monitor the effects of multi excitons on the PL decay dynamics, transient THz spectroscopy to probe the increased far infrared absorption of multi excitons, and quasi-CW photoluminescence spectroscopy to observe the PL red shift and line shape changes due to multi excitons.[33] These methods are useful to determine the inter- or intraband relaxation processes including exciton lifetime of electron-hole pairs, electron injection times from photoexcited PbS QDs and the hole transfer time from PbS QDs to a hole acceptor.

Exciton and biexciton lifetime of PbS QDs

The absorbance spectroscopy was used to determine the lifetime of electron and hole pairs generated in PbS QDs. Figure 1.6 shows both the exciton lifetime[46] and the biexciton lifetime[47] decrease as the size of PbS QDs because of enhanced Coulomb interaction by relatively strong quantum confinement

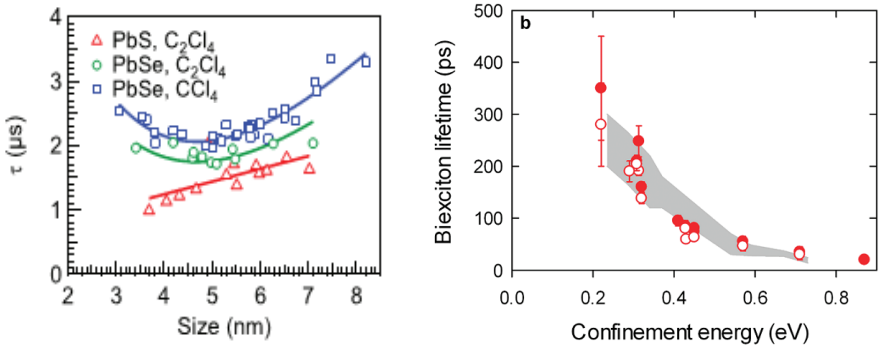

Figure 1.6. (Left) Size-dependent lifetime of PbS QDs calculated from optical parameters in reasonable agreement with experimental values obtained through time-resolved luminescence measurements.[48] (Right) Biexciton lifetimes of colloid PbS QDs as measured by TA (solid circles) and PL up-conversion (open circles) agree very well with PbSe (gray shaded area encompasses the ± single standard deviation).

Electron injection from excited PbS QDs into TiO_2

By using the fluorescence transients, the size-dependent fluorescence decays of PbS QDs and PbS-TiO_2 composite were investigated,[49] as shown in Figure 1.7. The smaller PbS QDs produced a faster electron injection into TiO_2 NPs because of enlarged CB position and boosted bandgap energy. However, this time resolution of TRPL limited the accurate detection of ultrafast electron transfer dynamic as reported at time scale less than 10 fs.[50]

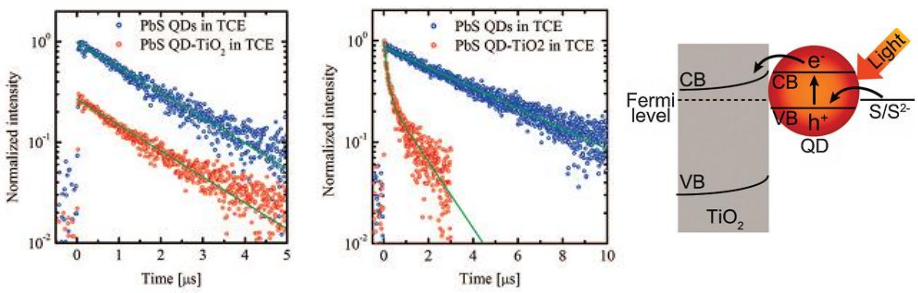

Figure 1.7. The fluorescence decays of PbS QDs (blue circles) and PbS-TiO_2 composite (red circles) in TCE for PbS QDs with diameter of 4.8 nm (left) and 3.4 nm (middle). Fluorescence lifetime of PbS-TiO_2: 4.8 nm: 1.7 μs, 3.4 nm: ~1 μs. (Right) Schematic illustration of photo-induced charge separation

of the QDs/TiO_2 system.[51]

Hole transfer from PbS QDs to a hole acceptor

Hole transfer times from excited PbS QDs to a hole acceptor of spiro-OMeTAD molecule was determined around 1 ps,[52] as shown in Figure 1.8; hole transfer time from excited CdSe on TiO_2 to 0.1 M S^{2-} solution were measured as 0.13 and 11.7 ns.[53]

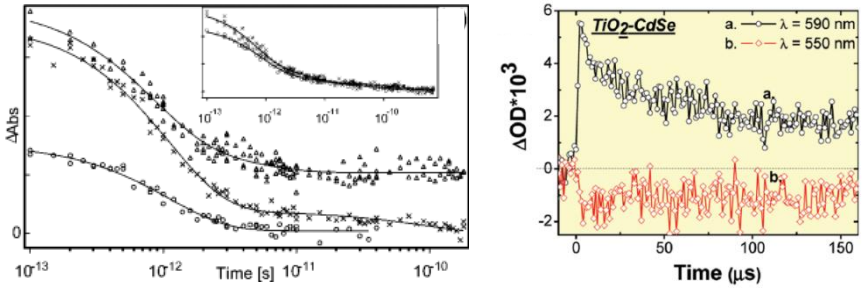

Figure 1.8. (Left) Transient absorption kinetics of PbS-ZrO_2 (O), PbS-TiO_2 (x), and PbS-TiO_2 spin-coated with hole conductor solution (triangles) at the excitation light wavelength of 600 nm and the probe light wavelength of 1400 nm (778 nm in the case of the inset). (Right) Transient absorption kinetics of CdSe/TiO_2 film in contact with 0.1 M Na_2S electrolyte recorded after 532 nm laser pulse excitation at probe wavelengths of 550 and 590 nm.

1.2 Localized surface plasmonic resonance (LSPR)

The optical properties of metal NPs have long been of interest in physical chemistry since Faraday investigated colloidal gold in the middle 1800s. To date, improvements in classical wet chemistry methods as well as new lithographic techniques have advance the synthesis of noble metal nanostructures with a wide range of shapes, sizes and dielectric environments, and made it possible to tune the electrical and optical properties of localized surface plasmonic resonance (LSPR).

1.2.1 Fundamental concepts

Polarizability and local electric field

Consider a homogeneous spherical nanoparticle under the irradiation of plane wave light, as presented in Figure 1.9.[54] The nanoparticle sphere with a diameter a (under the condition of $a \ll \lambda$) has a

wavelength dependent complex dielectric constant $\varepsilon(\omega)$, here ω is the angular frequency. The sphere is surrounded by a homogeneous, infinitely large, non-absorbing and nonmagnetic medium with the dielectric constant ε_m. The electric field of light is

$$E = E_0 \exp(-\omega t)x \tag{4}$$

Where E_o is a constant, x is the unit direction vector and t the time interval.

Conceptually, the conduction electrons in the nano sphere are displaced by the external electric field to create a negative charge center on one end and a positive charge center on the other end, forming a dipole. If ω is not very high, the dipole can oscillate fast enough to follow the phase of E. The first order of dipole moment p is linearly proportional to E, as

$$p = \varepsilon_m \alpha E \tag{5}$$

Where α is the static polarizability of the sphere is given as:

$$\alpha = 4\pi\varepsilon_0 a^3 \frac{\varepsilon - \varepsilon_m}{\varepsilon + 2\varepsilon_m} \tag{6}$$

The denominator reaches a minimum at:

$$\mathrm{Re}(\varepsilon(\omega)) = -2\varepsilon_m \tag{7}$$

This is where the enhancement of absorption, scattering and local electric field comes from.

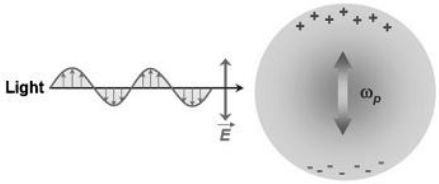

Figure 1.9. Schematic image of plasmon oscillation for a metal nano sphere Interaction of the electromagnetic wave with a metal causes the free electrons to coherently oscillate at the plasmon frequency (ω_p) against the immobile positive-ion lattice.

Plasmonic resonance frequency

Based on the Drude model, the dielectric function of the metals can be expressed as:

$$\varepsilon(\omega) = 1 - \frac{\omega_p^{\ 2}}{\omega^2 + i\gamma\omega} = \varepsilon_1(\omega) + i\gamma\varepsilon_2(\omega)$$
$$\varepsilon_1(\omega) = 1 - \frac{\omega_p^{\ 2}}{1+\omega^2\tau^2}, \varepsilon_2(\omega) = \frac{\omega_p^{\ 2}\tau}{\omega(1+\omega^2\tau^2)} \quad (8)$$

Where ε_1 and ε_2 are respectively the real part and the imaginary part of ε, τ is the relaxation time of the free electron and $\gamma=1/\tau$ is the intraband damping frequency.

The plasma frequency ω_p of a bulky metal is given by

$$\omega_p = \sqrt{ne^2/\varepsilon_o m} \quad (9)$$

Where n is the number density of electrons, e the electric charge, and m the effective mass of the electron.

The resonant frequency ω_{LSPR} can be determined from Eq.11 to be

$$\omega_{LSPR} \approx \omega_p / \sqrt{1+2\varepsilon_m} \quad (10)$$

Eq.10 indicates that the resonant wavelength is red-shifted if the surrounding medium has a higher dielectric constant in reference with vacuum.

Absorption, scattering and extinction

Mie[55, 56] presented a solution to Maxwell's equations2-4 that describes the extinction spectra (extinction) scattering + absorption) of spherical particles of arbitrary size. The cross sections for absorption and scattering can be calculated via the Poynting vector, then the extinction cross section can be obtained by summing up, as expressed by

$$C_{abs} = 4\pi k a^3 \mathrm{lm}(\frac{\varepsilon-\varepsilon_m}{\varepsilon+2\varepsilon_m})$$
$$C_{sca} = \frac{8\pi}{3} k^4 a^6 (\frac{\varepsilon-\varepsilon_m}{\varepsilon+2\varepsilon_m})^2$$
$$C_{ext} = \frac{9\omega\varepsilon_m^{\ 3/2}V}{c} \frac{\varepsilon_2}{(\varepsilon_1+2\varepsilon_m)^2+\varepsilon_2^{\ 2}} \quad (11)$$

Where $k=2\pi/\lambda$ is the wavenumber, V is the volume of sphere and c is the speed of light in vacuum. Similarly, at the resonance frequency that satisfies $\varepsilon_1=-2\varepsilon_m$, the cross sections are enhanced. For nanoparticles with $a << \lambda$, C_{sca} is much smaller than C_{abs}.

1.2.2 Influences of nanoparticle shape and size

Distinct spectral responses can be attained by tuning geometrical shapes or sizes of noble metal nanostructures, which affect polar mode of LSPR and result in multipolar resonances in different directions characterized as multiple resonant peaks, as shown in Figure 1.10. In addition, the location of an abrupt shape change bring out strongly enhanced local electromagnetic field than that in a nanosphere of the same the volume.[57]

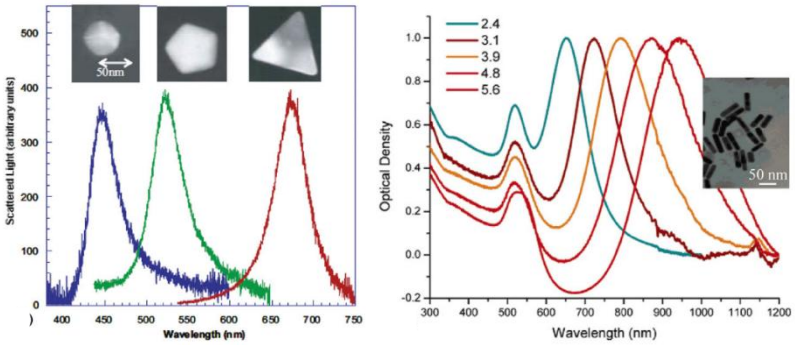

Figure 1.10. (Left) Scattering spectra of single Ag NPs in different shapes.[58] (Right) Absorption spectra of gold nanorods of different aspect ratios with longitudinal and transverse polar modes.[59]

1.2.3 LSPR sensitized solar cells

Plasmonic photovoltaic devices based on noble metal nanoparticles (NPs) is another approach to advance the photoenergy conversion owing to the localized surface plasmon resonance (LSPR).[22, 60] A junction between n-type TiO_2 NP contact the Au surface is formed as an initial difference in Fermi levels (chemical potential of electrons) exists between the two phases such that electrons are transferred to the metal upon contact to equalize the Fermi levels and establish a thermodynamic equilibrium. This equilibration process creates a positive space charge layer and bend the conduction and valence band edges of TiO_2 (Figure 1.11), resulting in a potential barrier at the interface known as Schottky junction against further electron transfer into the TiO_2 (as indicated by E). Visible light absorption in Au NP (as depicted by A) induce the generation of a plasmon which decays into a hot electron-hole pair within the metal via Landau damping on time scales of a few to tens of femtoseconds,[61, 62] then the hot electron with sufficient energy go across the Schottky junction and fed into the conduction band of TiO_2 (as depicted by C). The existence of the energy barrier prevent

recombination of injected hot electron and holes in the Au region, thus can enhance photoelectric conversion efficiency.

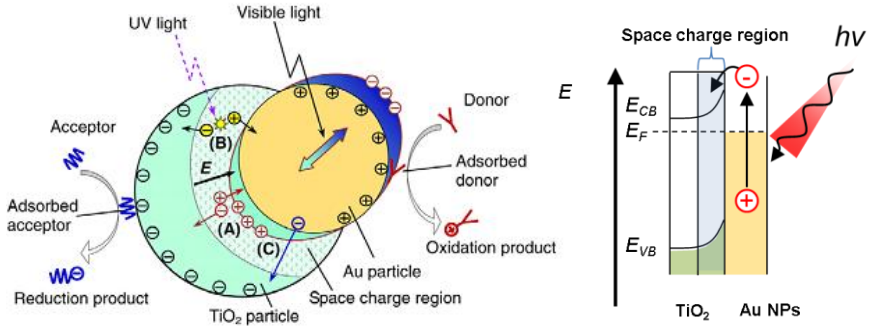

Figure 1.11. (Left) Schematic presentation of the major mechanisms[63] and (right) energy diagrams of plasmonic Au/TiO_2 solar cell.

1.3 Surface-enhanced Raman spectroscopy

Raman scattering cross sections (10^{-29} cm^2 $molecule^{-1}$) for most molecules are several orders of magnitude below those in optical absorption or emission spectroscopy. Consequently lack of sensitivity remains one of the key limitations. The discovery of surface-enhanced Raman scattering (SERS) opened a new avenue for Raman spectroscopy. Plasmonic surfaces enhance the Raman scattered light from molecules on or near the surface by 10^8 to 10^{12} times.[64] SERS spectroscopy has been widely employed for chemistry,[65] biology[66] and medicine,[67, 68] by utilizing various nanoparticle size, shape, and spacing parameters, and massively parallel. As a result of large optical fields and resonance-related effects, the Raman cross section for a molecule on a surface is enhanced by factors of up to 10^6. The enhanced mechanism of SERS is normally attributed to electromagnetic (EM) through interaction with surface plasmon excitations and chemical (CM) enhancement through charge transfer interaction of the absorbed molecule with the metal surface.[69-71], in which the former term is responsible for the major portion of SERS enhancement.

During the past few decades, SERS active substrates have been developed significantly. Besides coinage metals and their alloys that have been extensively employed owing to their large enhancement through surface plasmon resonance (SPR), semiconductor QDs have also been validated the enhancement with a factor on the order as high as 10^3 to 10^6 times [72-74] as SERS active substrates and induced increasing attention due to the widespread application in both SERS spectroscopy and

material fields. Especially PbS QDs which play a notable role in SERS both by physical and chemical mechanism: PbS QDs intensely enhance the electromagnetic field generated by localized surface plasmon resonance, and transfer carriers to surfactant thus modify Raman spectrum.

1.3.1 Electromagnetic mechanism (EM)

Electromagnetic enhancement is due primarily to localized surface plasmon resonance. Metals can be considered as a plasma of electrons composed of polarizable, free electrons (mobile), and a positive ion core (immobile). Interaction of the electromagnetic wave with a metal causes the free electrons to coherently oscillate at the plasmon frequency (ω_p) against the immobile positive ion lattice. Although the increase in the local electric field is usually modest, the enhancement in the inelastically scattered light intensity scales to the fourth power, causing a remarkable SERS effect. However, the enhancement effects are highly localized and decay rapidly as the separation between the analyte and the metal particles increases, making SERS a truly surface-sensitive technique.

Besides nano-structured metals that used to generate 'hot-spots', i.e. the localized confinement of high electromagnetic fields in small spaces for SERS, there has been a growing interest in theoretical and experimental studies of strongly coupled dielectric QDs with metal NP system.[75] High field enhancements for SERS have been observed from various non-metallic materials, such as metal NPs and PbS QDs.[76] It has been reported that higher real and imaginary parts (n, k) of the refractive index of a dielectric NP lead to bigger electric fields in the gap of NP and metallic substrate.[77] PbS has a high refractive index and thus can induce high field enhancements when placed near a metallic NP. Although PbS QDs do not possess a plasmon resonance by themselves, their presence increases the electric field in the gap between the QDs and metal NPs significantly, because the fact that the charge oscillations of the metallic NP are screened by those induced in the dielectric media, resulting in localized hybridized NP plasmon confined to the gap between them. Finite-difference time-domain (FDTD) calculations[78] have investigated that coupling PbS QDs with noble metal NPs will enhance the electric-field generated by localized surface plasmon resonance, and the enhancement is strongly

dependent on their sizes and distance, as shown in Figure 1.12 .

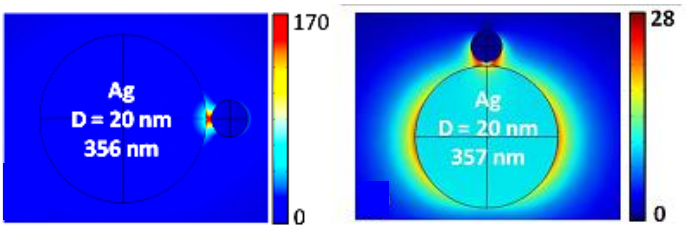

Figure 1.12. Electric field in the gap between a PbS QD (D= 4.4 nm) placed 0.6 nm away from an Ag NP (D= 20 nm) with the light polarization parallel (left) and perpendicular (right) to the dimer axis.

1.3.2 Chemical mechanism (CM)

Chemical effect is another independent mechanism that enhances the Raman-scattering cross section of the analyte adsorbed on the metal surface. The rationale behind the prediction of this secondary, independent, and relatively weak enhancement is the dependence of the enhancement on the chemical nature of the analyte molecule or structure. Whereas electromagnetic enhancement is a chemically non-selective mechanism, more than two orders of difference in the enhancement can be observed, due only to the chemical-enhancement mechanism. The electronic states of the analyte molecule are either shifted or broadened due to either the interaction with metal or the origin of new electronic states, resulting in additional enhancement often termed as chemical enhancement. The proximity between the metal or semiconductor and the analyte molecules adsorbed on the surface causes electronic coupling by a charge-transfer mechanism (CT), as shown in Figure 1.13 resulting in resonant intermediate states and thereby enhancing Raman scattering.[68, 69]

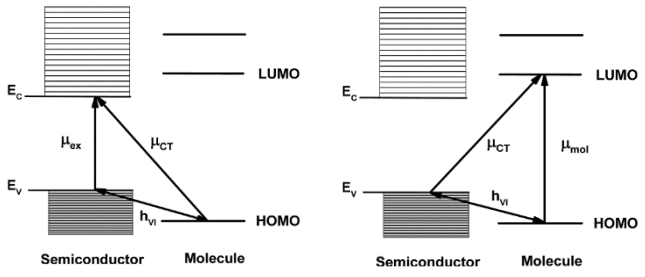

Figure 1.13. The charge-transfer process between semiconductor and molecule: CT resonance is coupled to (left) exciton resonance and (right) the molecular resonance.

Surface-enhanced Raman spectra of 4-mercaptopyridine on PbS QDs was investigated as a function of nanoparticle size and excitation wavelength, and was ascribed to CT mechanism dependent on quantum confinement.[76]

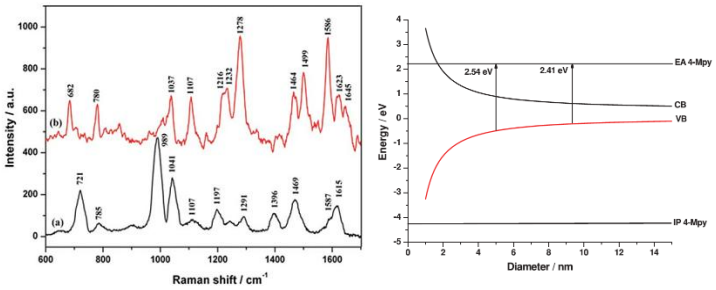

Figure 1.14. (Left) Comparison of the Raman spectrum of (a) 4-Mpy powder with that of (b) 4-Mpy adsorbed on 8.9 nm PbS quantum dot. Excitation is at 514.5 nm. . (Right) CT from size-dependent VB of PbS QDs to LUMO of 4-Mpy.

1.3.3 Phonon mode of semiconductor via Raman

A phonon is a quantum mechanical description of an elementary vibrational motion in which a lattice of atoms or molecules uniformly oscillates at a single frequency.[16] The normal modes of vibration of a crystal and to calculate their energies (or frequencies, ω) as a function of their wavevector q. The relationship ω (q) is called phonon dispersion.

Optical phonon confinement

Only when the grain size is smaller than typically 20 lattice parameters, the periodicity of the crystal is interrupted, in an isolated grain the phonon can get reflected from the boundaries and remain confined within the grain, named phonon confinement. Optical as well as acoustical phonons get confined within the particle.

The consequence of phonon confinement is noticeable in the vibrational spectra. Uncertainty principle arises from the wave properties inherent in the quantum mechanical description of nature, giving a statement that the position and momentum of a particle cannot be simultaneously measured with arbitrarily high precision.

$$\Delta q \Delta r \geq h / 4\pi \qquad (12)$$

Where Δq is the momentum uncertainty (wavevector uncertainty), Δr is the size uncertainty, h is the Planck constant. The size uncertainty is related to the size of particle, nano structured crystal has much more prominent wavevector uncertainty than bulk crystal because of the drastically reduced size, so that Δq cannot be neglect as in the case of bulk crystal.

Based on the wavevector selection rule of visible Raman scattering in bulk crystals, Raman spectral can only originate from the phonons at $q \approx 0$ and the Raman spectral peaks are the narrow spectral lines at bulk frequency of ω_0 (Figure 4). But in nanostructured crystal, the wavevector uncertainty leads to the relaxation of the selection rule of $q \approx 0$ in visible Raman scattering, and then the phonons in the region of wavevector Δq can join the Raman scattering process, resulting in broadened spectral bands linewidth. In the case that the dispersion relation of the optical phonons in the Brillouin zone is negative (Figure a ω_0), phonons of smaller energy dominate in the scattering process, leading to red-shifted Raman shift.

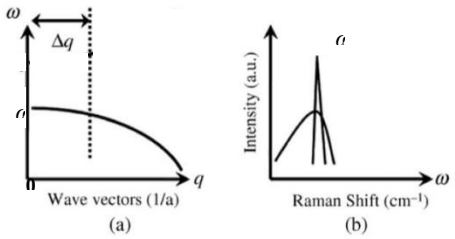

Figure 1.15. (a) Typical dispersion curves of bulk semiconductors and (b) expected Raman spectral features of nanostructured material.

Phonon mode of microcrystal PbS

Figure 1.16 gives an example of Raman spectra for microcrystal PbS,[79] presenting LO mode with characteristics of decreased peak frequency and increased FWHM as the crystalline size decreases.

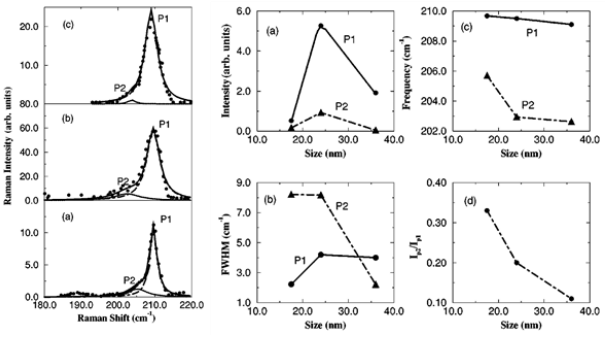

Figure 1.16. (Left) Raman spectra of microcrystal PbS with average size of (a) 17.5, (b) 24, and (c) 36 nm excited by 514.5 nm. (Right) size-dependent Raman intensity, FWHM, frequency and intensity

ratio.

The aim and outline of this study

Plasmon induced strong electromagnetic field could be applied to quantized nanoparticles in electrochemistry environment during the photon-matter interaction involving molecule detection, photoelectric conversion, photoluminescence and strong coupling. In this sense, plasmonic gold nanostructures with controlled size and shape were well designed to couple with lead sulfide quantum dots (PbS QDs) varied in size and bandgap energy from near infrared to visible light.

Solar cell of layered PbS QDs/TiO_2/Au NPs/TiO_2 substrate was fabricated and the morphology was characterized by SEM-EDS; size-dependent band edge positions of PbS QDs were estimated based on absorption spectra; photoluminescence of PbS QDs on TiO_2/Au NPs/TiO_2 were obtained by electrochemical fluorescence spectroscopy and image mapping (Chapter 2).

Highly ordered Au nanodimer array were fabricated as substrate; surface modification of oleic acid molecule surrounding size-controlled PbS QDs were characterized by surface-enhanced Raman scattering both in air and under electrochemical environment (Chapter 3). Photocurrent and generation of polysulfur of PbS QDs/TiO_2/Au/TiO_2 system were simultaneously detected by electrochemical surface-enhanced Raman scattering (Chapter 4).

Enhancement on photoelectric conversion efficiency under visible light irradiation was confirmed by TiO_2/Au/TiO_2 which was sensitized by size-controlled PbS QDs with different capping ligands owing to metallic resonance (Chapter 5) and combination of multiple exciton generation (Chapter 6).

Strong coupling between PbS QDs and Au bowtie nanodimers were observed by dark-filed scattering spectroscopy and image mapping techniques (Chapter 7).

References

1. Becquerel, A. E. *Comptes Rendus des Séances Hebdomadaires* **1839,** 9, 561-567.
2. Brattain, W. H.; Garrett, C. G. B. *Bell System Technical Journal* **1955,** 34, (1), 129-176.
3. *Renewables 2016 Global Status Report*; http://www.ren21.net/status-of-renewables/global-status-report/, **2016**.
4. Grätzel, M. *Journal of Photochemistry and Photobiology C: Photochemistry Reviews* **2003,** 4, (2), 145-153.
5. Maikov, G. I.; Vaxenburg, R.; Sashchiuk, A.; Lifshitz, E. *ACS Nano* **2010,** 4, (11), 6547-6556.

6. Sowers, K. L.; Swartz, B.; Krauss, T. D. *Chemistry of Materials* **2013,** 25, (8), 1351-1362.
7. Zhuang, Z.; Peng, Q.; Li, Y. *Chemical Society Reviews* **2011,** 40, (11), 5492-5513.
8. Sukhovatkin, V.; Hinds, S.; Brzozowski, L.; Sargent, E. H. *Science* **2009,** 324, (5934), 1542-1544.
9. Sambur, J. B.; Novet, T.; Parkinson, B. A. *Science* **2010,** 330, (6000), 63-66.
10. Semonin, O. E.; Luther, J. M.; Choi, S.; Chen, H.-Y.; Gao, J.; Nozik, A. J.; Beard, M. C. *Science* **2011,** 334, (6062), 1530-1533.
11. Yuan, M.; Liu, M.; Sargent, E. H. *Nature Energy* **2016,** 1, 16016.
12. Nabika, H.; Takase, M.; Nagasawa, F.; Murakoshi, K. *The Journal of Physical Chemistry Letters* **2010,** 1, (16), 2470-2487.
13. Zhang, X.; Chen, Y. L.; Liu, R. S.; Tsai, D. P. *Reports on progress in physics. Physical Society* **2013,** 76, (4), 046401.
14. Kumar, J.; Wei, X.; Barrow, S.; Funston, A. M.; Thomas, K. G.; Mulvaney, P. *Physical Chemistry Chemical Physics* **2013,** 15, (12), 4258-4264.
15. Kamat, P. V.; Tvrdy, K.; Baker, D. R.; Radich, J. G. *Chemical Reviews* **2010,** 110, (11), 6664-6688.
16. Kittel, C., Chapter 4: Phonons I. Crystal Vibrations. In *Introduction to solid state physics*, 8th edition ed.; John Wiley and Sons Inc.: **2005**; pp 89-104.
17. Beard, M. C.; Ellingson, R. J. *Laser & Photonics Reviews* **2008,** 2, (5), 377-399.
18. Pankove, J. I., *Optical processes in semiconductors*. Dover publications: New York, **1971**.
19. Wang, Y.; Suna, A.; Mahler, W.; Kasowski, R. *The Journal of Chemical Physics* **1987,** 87, (12), 7315-7322.
20. Leventis, H. C.; O'Mahony, F.; Akhtar, J.; Afzaal, M.; O'Brien, P.; Haque, S. A. *Journal of the American Chemical Society* **2010,** 132, (8), 2743-2750.
21. Alivisatos, A. P. *Science* **1996,** 271, (5251), 933-937.
22. Brown, P. R.; Kim, D.; Lunt, R. R.; Zhao, N.; Bawendi, M. G.; Grossman, J. C.; Bulović, V. *ACS Nano* **2014,** 8, (6), 5863-5872.
23. Boles, M. A.; Ling, D.; Hyeon, T.; Talapin, D. V. *Nat Mater* **2016,** 15, (2), 141-153.
24. Gaponik, N.; Talapin, D. V.; Rogach, A. L.; Hoppe, K.; Shevchenko, E. V.; Kornowski, A.; Eychmüller, A.; Weller, H. *The Journal of Physical Chemistry B* **2002,** 106, (29), 7177-7185.
25. Hickey, S. G.; Waurisch, C.; Rellinghaus, B.; Eychmüller, A. *Journal of the American Chemical Society* **2008,** 130, (45), 14978-14980.
26. Cooper, J. K.; Franco, A. M.; Gul, S.; Corrado, C.; Zhang, J. Z. *Langmuir* **2011,** 27, (13), 8486-8493.
27. Crisp, R. W.; Kroupa, D. M.; Marshall, A. R.; Miller, E. M.; Zhang, J.; Beard, M. C.; Luther, J. M. *Scientific Reports* **2015,** 5, 9945.
28. Thon, S. M.; Ip, A. H.; Voznyy, O.; Levina, L.; Kemp, K. W.; Carey, G. H.; Masala, S.; Sargent, E. H. *ACS Nano* **2013,** 7, (9), 7680-7688.
29. Kim, S.; Bawendi, M. G. *Journal of the American Chemical Society* **2003,** 125, (48), 14652-14653.
30. Ip, A. H.; Thon, S. M.; Hoogland, S.; Voznyy, O.; Zhitomirsky, D.; Debnath, R.; Levina, L.; Rollny, L. R.; Carey, G. H.; Fischer, A.; Kemp, K. W.; Kramer, I. J.; Ning, Z.; Labelle, A. J.; Chou, K. W.; Amassian, A.; Sargent, E. H. *Nat Nano* **2012,** 7, (9), 577-582.
31. Shockley, W.; Queisser, H. J. *Journal of Applied Physics* **1961,** 32, (3), 510-519.
32. Wolf, M.; Brendel, R.; Werner, J. H.; Queisser, H. J. *Journal of Applied Physics* **1998,** 83, (8), 4213-4221.
33. Nozik, A. J. *Chemical Physics Letters* **2008,** 457, (1–3), 3-11.
34. Wang, S.; Khafizov, M.; Tu, X.; Zheng, M.; Krauss, T. D. *Nano Letters* **2010,** 10, (7), 2381-2386.

35. Franceschetti, A.; Zhang, Y. *Physical Review Letters* **2008,** 100, (13), 136805.
36. Schaller, R. D.; Pietryga, J. M.; Klimov, V. I. *Nano Letters* **2007,** 7, (11), 3469-3476.
37. Beard, M. C.; Knutsen, K. P.; Yu, P.; Luther, J. M.; Song, Q.; Metzger, W. K.; Ellingson, R. J.; Nozik, A. J. *Nano Letters* **2007,** 7, (8), 2506-2512.
38. Hardman, S. J. O.; Graham, D. M.; Stubbs, S. K.; Spencer, B. F.; Seddon, E. A.; Fung, H.-T.; Gardonio, S.; Sirotti, F.; Silly, M. G.; Akhtar, J.; O'Brien, P.; Binks, D. J.; Flavell, W. R. *Physical Chemistry Chemical Physics* **2011,** 13, (45), 20275-20283.
39. Yang, Y.; Rodríguez-Córdoba, W.; Lian, T. *Nano Letters* **2012,** 12, (8), 4235-4241.
40. El-Ballouli, A. a. O.; Alarousu, E.; Usman, A.; Pan, J.; Bakr, O. M.; Mohammed, O. F. *ACS Photonics* **2014,** 1, (3), 285-292.
41. Midgett, A. G.; Luther, J. M.; Stewart, J. T.; Smith, D. K.; Padilha, L. A.; Klimov, V. I.; Nozik, A. J.; Beard, M. C. *Nano Letters* **2013,** 13, (7), 3078-3085.
42. Schaller, R. D.; Klimov, V. I. *Physical Review Letters* **2004,** 92, (18), 186601.
43. Nozik, A. J. *Annual Review of Physical Chemistry* **2001,** 52, (1), 193-231.
44. Nozik, A. J. *Physica E: Low-dimensional Systems and Nanostructures* **2002,** 14, (1–2), 115-120.
45. Nootz, G.; Padilha, L. A.; Levina, L.; Sukhovatkin, V.; Webster, S.; Brzozowski, L.; Sargent, E. H.; Hagan, D. J.; Van Stryland, E. W. *Physical Review B* **2011,** 83, (15), 155302.
46. Moreels, I.; Lambert, K.; Smeets, D.; De Muynck, D.; Nollet, T.; Martins, J. C.; Vanhaecke, F.; Vantomme, A.; Delerue, C.; Allan, G.; Hens, Z. *ACS Nano* **2009,** 3, (10), 3023-3030.
47. Stewart, J. T.; Padilha, L. A.; Qazilbash, M. M.; Pietryga, J. M.; Midgett, A. G.; Luther, J. M.; Beard, M. C.; Nozik, A. J.; Klimov, V. I. *Nano Letters* **2012,** 12, (2), 622-628.
48. Jamie, H. W.; Elizabeth, T.; Andrew, R. W.; Norman, R. H.; Halina, R.-D. *Nanotechnology* **2005,** 16, (2), 175.
49. Hyun, B.-R.; Zhong, Y.-W.; Bartnik, A. C.; Sun, L.; Abruña, H. D.; Wise, F. W.; Goodreau, J. D.; Matthews, J. R.; Leslie, T. M.; Borrelli, N. F. *ACS Nano* **2008,** 2, (11), 2206-2212.
50. Yang, Y.; Rodríguez-Córdoba, W.; Xiang, X.; Lian, T. *Nano Letters* **2012,** 12, (1), 303-309.
51. Kawawaki, T.; Tatsuma, T. *Physical Chemistry Chemical Physics* **2013,** 15, (46), 20247-20251.
52. Plass, R.; Pelet, S.; Krueger, J.; Grätzel, M.; Bach, U. *The Journal of Physical Chemistry B* **2002,** 106, (31), 7578-7580.
53. Chakrapani, V.; Baker, D.; Kamat, P. V. *Journal of the American Chemical Society* **2011,** 133, (24), 9607-9615.
54. Noguez, C. *The Journal of Physical Chemistry C* **2007,** 111, (10), 3806-3819.
55. Mie, G. *Annalen der Physik* **1908,** 330, (3), 377-445.
56. Bohren, C. F.; Huffman, D. R., Absorption and Scattering by a Sphere. In *Absorption and Scattering of Light by Small Particles*, Wiley-VCH Verlag GmbH: **2007**; pp 82-129.
57. Kelly, K. L.; Coronado, E.; Zhao, L. L.; Schatz, G. C. *The Journal of Physical Chemistry B* **2003,** 107, (3), 668-677.
58. Mock, J. J.; Barbic, M.; Smith, D. R.; Schultz, D. A.; Schultz, S. *The Journal of Chemical Physics* **2002,** 116, (15), 6755-6759.
59. Huang, X.; El-Sayed, I. H.; Qian, W.; El-Sayed, M. A. *Journal of the American Chemical Society* **2006,** 128, (6), 2115-2120.
60. Nair, G.; Zhao, J.; Bawendi, M. G. *Nano Letters* **2011,** 11, (3), 1136-1140.
61. Hartland, G. V. *Chemical Reviews* **2011,** 111, (6), 3858-3887.
62. Sönnichsen, C.; Franzl, T.; Wilk, T.; von Plessen, G.; Feldmann, J.; Wilson, O.; Mulvaney, P. *Physical Review*

Letters **2002,** 88, (7), 077402.

63. Zhang, X.; Chen, Y. L.; Liu, R.-S.; Tsai, D. P. *Reports on Progress in Physics* **2013,** 76, (4), 046401.
64. Smith, E.; Dent, G., Surface-Enhanced Raman Scattering and Surface-Enhanced Resonance Raman Scattering. In *Modern Raman Spectroscopy – A Practical Approach*, John Wiley & Sons, Ltd: **2005**; pp 113-133.
65. Kneipp, K.; Kneipp, H.; Itzkan, I.; Dasari, R. R.; Feld, M. S. *Chemical Reviews* **1999,** 99, (10), 2957-2976.
66. Kneipp, J.; Kneipp, H.; Kneipp, K. *Chemical Society Reviews* **2008,** 37, (5), 1052-1060.
67. Nabiev, I.; Chourpa, I.; Manfait, M. *Journal of Raman Spectroscopy* **1994,** 25, (1), 13-23.
68. Lane, L. A.; Qian, X.; Nie, S. *Chemical Reviews* **2015,** 115, (19), 10489-10529.
69. George C. Schatz, M. A. Y., Richard P. Van Duyne, Electromagnetic Mechanism of SERS. In *Surface-Enhanced Raman Scattering: Physics and Applications*, K. Kneipp; M. Moskovits; H. Kneipp, Eds. Springer-Verlag Berlin Heidelberg: New York, **2006**; pp 19-45.
70. Ronald L. Birke, J. R. L., Surface-Enhanced Raman Scattering. In *Spectroelectrochemistry: Theory and Practice*, R.J. Gale, Ed. Springer US: Plenum Press, New York, **1998**; pp 263-348.
71. Lombardi, J. R.; Birke, R. L. *Accounts of Chemical Research* **2009,** 42, (6), 734-742.
72. Livingstone, R.; Zhou, X.; Tamargo, M. C.; Lombardi, J. R.; Quagliano, L. G.; Jean-Mary, F. *The Journal of Physical Chemistry C* **2010,** 114, (41), 17460-17464.
73. Li, W.; Zamani, R.; Rivera Gil, P.; Pelaz, B.; Ibáñez, M.; Cadavid, D.; Shavel, A.; Alvarez-Puebla, R. A.; Parak, W. J.; Arbiol, J.; Cabot, A. *Journal of the American Chemical Society* **2013,** 135, (19), 7098-7101.
74. Cong, S.; Yuan, Y.; Chen, Z.; Hou, J.; Yang, M.; Su, Y.; Zhang, Y.; Li, L.; Li, Q.; Geng, F.; Zhao, Z. *Nat Commun* **2015,** 6.
75. Hakami, J.; Wang, L.; Zubairy, M. S. *Physical Review A* **2014,** 89, (5), 053835.
76. Fu, X.; Pan, Y.; Wang, X.; Lombardi, J. R. *The Journal of Chemical Physics* **2011,** 134, (2), 024707.
77. Hutter, T.; Huang, F. M.; Elliott, S. R.; Mahajan, S. *The Journal of Physical Chemistry C* **2013,** 117, (15), 7784-7790.
78. Hutter, T.; Mahajan, S.; Elliott, S. R. *Journal of Raman Spectroscopy* **2013,** 44, (9), 1292-1298.
79. Nanda, K.; Sahu, S.; Soni, R.; Tripathy, S. *Physical Review B* **1998,** 58, (23), 15405-15407.

Chapter 2

Determination of Optical and Electronic Properties of PbS Quantum Dots at Electrified Interfaces

2.1 Introduction

Photoluminescence, the radiated process for the recombination of electron-hole pair excited by light irradiation with energy larger than the bandgap, also plays a significant role in quantum dots (QDs) sensitized photoelectrochemical cell system besides the process of electron injection. To date, modification of fluorescence of emitters such as dyes or semiconductor QDs nearby noble metals has been widely discussed owing to surface plasmon resonance (SPR).[1, 2] Surface plasmon-assisted fluorescence enhancement[3-6] or quenching[7-9] is strongly dependent on the distance between the emitter and the metal surface.

Photoelectrochemistry has been regarded as a robust approach to modulate electric and/or chemical change of semiconductor electrode contacting electrolytes as the Fermi level of the system is able to be controlled by a polarized potential of a three-electrode system.[10, 11] For a QDs sensitized n-type semiconductor, such as TiO_2, the overall amount of electron-hole pairs generated in QDs excited by photon leading to the formation of excited electrons and holes. The photoluminescence processes could keep as constant under light irradiation with a constant intensity via the recombination of excited electrons and holes. As the Fermi level is controlled by an applied polarized potential, the amount of excited electron injected into the conduction band of TiO_2 is tunable so that the simultaneous photoluminescence measurements will provide an information of number of excited electrons and holes contribute to the generation of photocurrent. A positive potential can benefit the electron injection owing to an improved charge separation efficiency and thus a decreased photoluminescence intensity is expected.

In this chapter, characterization of PbS QDs used in the thesis and plasmonic photoenergy conversion system were performed by various methods. Multilayered electrode of TiO_2/Au/TiO_2 was

well fabricated by using liquid phase deposition (LPD) and electric beam vaporization; the morphology was characterized by SEM-EDS. Absorption and emission spectra of colloid PbS QDs varied in size was obtained, presenting typical quantum confinement effect with bandgap energy altered from near infrared to visible light; band energy positions were estimated according to the 1st exciton peak. Quantitative analysis of the composition of PbS QDs were performed by ICP-AES; drop casting of PbS QDs with a designed amount of deposition was utilized to sensitize the multilayered electrode. Electrochemical photoluminescence and simultaneous photocurrent measurements using TiO_2 and TiO_2/Au/TiO_2 electrodes sensitized by size-controlled PbS QDs with bandgap energy of near-infrared (OP-1101) and visible light (OP-682) were respectively carried out. Decreased photoluminescence was observed at the positive polarization, leading to increased photocurrent. Fluorescence microscopic imaging of OP-682/TiO_2/Au/TiO_2 presents spatially resolved potential-dependent photoluminescence properties.

2.2 Experimental

2.2.1 PbS QDs used in the study

Oleic acid (OA)-capped PbS QDs used in the present study were prepared by hot injection method based on Hines method.[12] Surface modification of long chain molecule OA was exchanged into short chain molecule of 3-mercaptopropionic acid (MPA). Briefly, 3-MPA was dissolved in methanol with the concentration of 10 mM; pH of the solution was adjusted to 11 by TMAH. The solution was degassed for 30 min by Argon. Then different volume of 200 μM original OA-capped PbS QDs was added into 1 mL of the MPA solution to dilute the original solution for various folds.

The PbS QDs were named according to the absorption maximum (Figure 2.4), as OP-1344, OP-1101, etc. with capping ligands of OA and MP-537 with capping ligands of MPA. Their average bandgap (E_g) were determined by the 1st exciton peak as 0.9, 1.1, 1.4, 1.6, 1.7, 1.8 and 2.3 eV. The average diameters were estimated to be 4.8, 3.7 2.7, 2.4, 2.3, 2.1 and 1.6 nm in diameter[13] respectively in reference of the 1st exciton peak.

2.2.2 Quantitative analysis of PbS QDs

The quantity of lead in colloid PbS QDs was analyzed via inductively coupled plasma atomic emission spectroscopy (ICPE-9000, SHIMADZU). Synthesized PbS QDs dispersed in hexane was added into ethanol and centrifuged in order to dissolve oleic acid as organics cool the plasma. Then the supernatant was removed and evaporated. Dilute nitric acid was chosen to completely digest the brown solid PbS into $Pb(NO_3)_2$ by accompanied with H_2S exhaust, because HNO_3 in a high concentration generates solid S or $PbSO_4$ that would clog the nebulizer and underestimate the quantity of Pb[14].

Lead nitrate dissolved in dilute nitric acid was used as the standard solution with a series of diluted concentration. Three measurements for each sample by detection wavelength of 220.353 nm yielded relative standard deviation (RSD) below 1.2% for three times measurements of each sample. The background was well corrected and the range for integration was properly selected. Calibration curve of the standard solution series was established by linear fitting with correlation coefficient better than 0.997 (see Figure A2.1 in Appendix). Digested QDs solution was estimated according to this curve, and mole concentration of PbS was calculated for the colloid PbS QDs solution (see Table A.2.2 in Appendix).

2.2.3 Morphology and element mapping

The morphology and element mapping of the electrode were measured in the University of Manchester by scanning electron microscopes (Philips XL30 FEG SEM) equipped with energy dispersive spectroscopy (EDS) analytical system (Rontec, now Bruker). SEM images were captured by using 10.0 kV electron beam with a magnification of 250,000 times and EDS mapping and spectrum were accumulated for 10 min by 20.0 kV electron beam with a magnification of 62,500 times.

2.2.4 Sensitization of PbS QDs

OA-capped PbS QDs (OP-682 and OP-1101, named following their 1st exciton peak) was diluted in argon-degased dehydrated hexane. The PbS QDs dispersion was drop-casted onto the surface of

TiO_2/Au/TiO_2 substrate with a particle density of 1.2E+12 cm^{-2} for both OP-682 and OP-1101 based on quantity analysis via ICP-AES. After solvent evaporation, EC-FL measurements were taken on these samples.

2.2.5 Preparation of plasmonic electrode

Thin TiO_2 film was deposited on a well washed 2×2.5 cm^2 conductive FTO glass with a deposition area of 2×2 cm^2 for 12 h by 0.1 M $(NH4)_2TiF_6$ and 0.2 M H_3BO_3 at 25 °C via liquid phase deposition (LPD). The dried substrate was annealed at 500 °C for 5 h for the crystallization of TiO_2 NPs in consideration of the available heating upper limit around 550 °C for FTO glass. Au film with a thickness of 5 nm was deposited on the TiO_2 substrate using the electric beam vaporization (0.20 nm/s, θ = 0 °; Quartz Crystal Monitor CRTM-6000, ULVAC; 3KWE-type electron gun, ANELVA; Compound Molecular Pump TG-800F-B, OSAKA VACCUM LTD), and the substrate was annealed at 500 °C for 30 min to quickly form gold nanoparticles with satisfactory average size for good scattering efficiency. Then LPD method with a deposition time of 1 h was once again performed to form a 2nd layer of TiO_2 thin film covering the gold NPs (Figure 2.1).

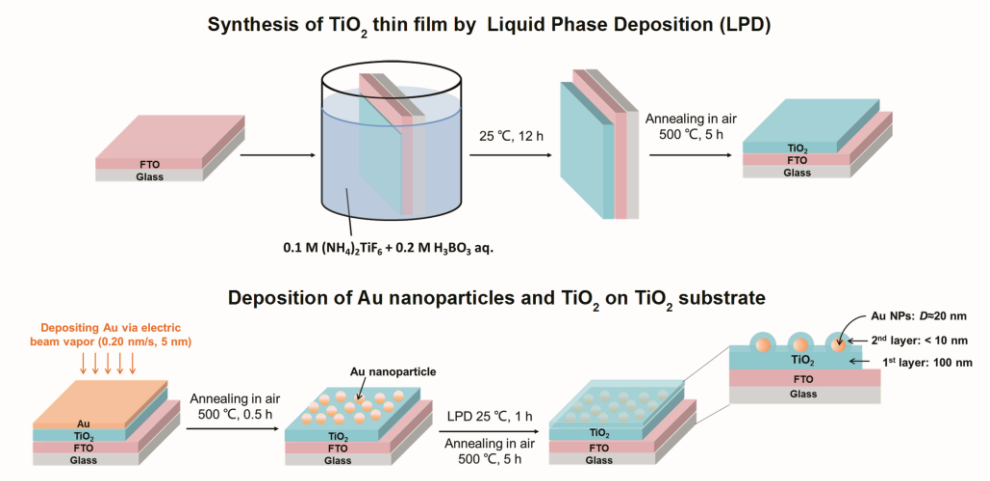

Figure 2.1. Schematic presentation of the preparation of TiO2/Au/TiO2 electrode.

2.2.6 Electrochemical photoluminescence measurement

Electrochemical fluorescence measurements were performed via a three-electrode system in electrolyte of 0.05 M Na_2S and 0.1 M NaOH aqueous solution (pH=13). Hand-made Ag/AgCl (sal.

KCl) and Pt narrow sheet or plate were respectively used as the reference and counter electrodes.

Near-infrared emission spectra of OP-1101 was measured by Fluorolog®3 spectrofluorometer (FL3C-2iHR, HORIBA) equipped with a single- or double-grating monochromator in the excitation and emission paths in an "L" configuration. The electrochemical cell was settled in the compartment with well-adjusted angle to collect a maximum fluorescence light (Figure 2.2a). Excitation light of 450, 500, 550 or 600 nm from a 450 W xenon lamp was cut off by using 700 nm filters (SCF-50S-70R, SIGMA KOKI Co., Ltd.) to avoid the overtone in the fluorescence spectrum. Potential was polarized from -0.6 to +0.5 V by an electrochemical workstation (EC-lab® software, BioLogic Science Instrument) to tune the Fermi level of TiO_2 and photocurrent generated by excitation was recorded during simultaneous fluorescence spectrum detected by a NIR photomultiplier tube (PMT) module (iHR320 Imaging Spectrometer) cooled with liquid nitrogen. Excitation and emission slit widths were both set as 14 nm, fluorescence spectrum was obtained by a grating of 600 g/mm, BLZ=1000 scanned in the infrared reign with increment of 1 nm. For size-controlled colloid PbS QDs in hexane and sensitized substrates in air, a cuvette or solid sample holder was used in the compartment.

Visible emission spectra of OP-682 was obtained by an inverted microscopy (OLYMPUS IX-71) equipped with an objective lens (10x, NA=0.70, W.D.=0.1-1.3 mm, LUCPlanFLN) and a Xenon lamp (IX-HLSH1000, OLYMPUS) (Figure 2.2b). Excitation light was narrowly selected by filter cubes transmitting blue light in wavelength region of 460-495 nm (U-MWIB3; emission filter: 510IF; dichromatic mirror: 505 nm; OLYMPUS) and green light in wavelength region of 520 -550 nm (U-MWIG2, emission filter: 580IF; dichromatic mirror: 565 nm; OLYMPUS). The output laser intensity was tunable via a FS filter yielding an estimated spot size of irradiation, ~1 μm, and was measured via power meter (OPHIR Japan LTD.). Polarized potential was well controlled from -0.8 to +0.5 V by a potentiostat (HSV-110, Hokuto Denko). Measurements at each potential were repeated for 3 times under visible light irradiation for 10 s and irradiation cut-off interval of 60 s. Simultaneous fluorescence spectrum and photocurrent were measured and recorded during irradiation with intensity of 0.65 and 0.4 mW for green and blue light, respectively. A spectrograph with a grating of 150 g/mm, BLZ=800 (ISOPlane SCT-320, Princeton Instruments) and a CCD camera (C9018, Hamamatsu Photonics) were used to disperse emitted photons and register spectrum. Spectrum was captured with

a slit width of 50 μm with the resolution of 0.4 nm. Image mapping was obtained with a slit width of 50 μm with exposure of 1 s and irradiation cut-off interval of 40 s at respective potential.

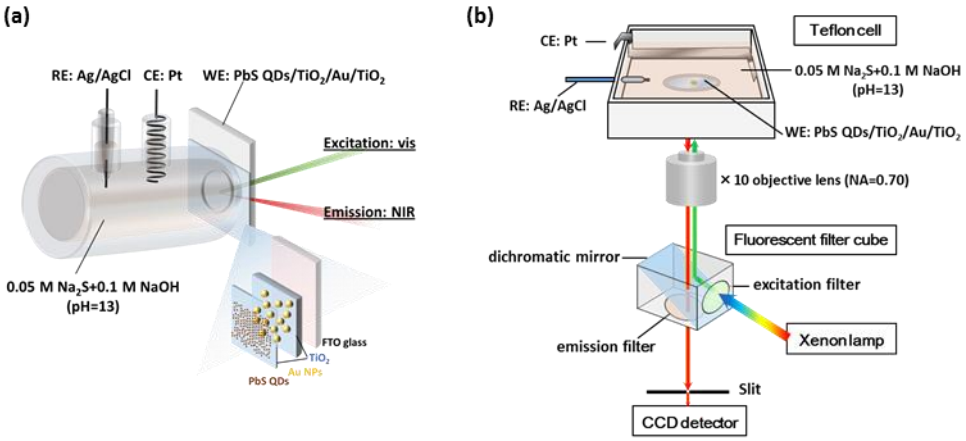

Figure 2.2. The cells for electrochemical luminescence measurements: (a) a glass cell with adjusted angle in the compartment and (b) a Teflon cell set upon an invert microscopy equipped with fluorescent filter cube.

2.3 Results and Discussion

2.3.1 SEM-EDS characterization of PbS QDs-sensitized plasmonic electrodes

The electrode was prepared layer-by-layer including respectively depositing thin TiO_2 film on FTO glass for 12 h via liquid phase deposition method (LPD), gold film with thickness of 5 nm on the TiO_2 via electric beam vaporization, and a 2nd thin TiO_2 film on Au for 1 h via LPD. Annealing process up to 500 ^oC was utilized to form nanoparticles based on crystallization of TiO_2 as well as aggregation of Au atoms. Then, drop casting of size-controlled PbS QDs based on ICPE quantitative analysis were performed onto the substrate.

Bare titanium dioxide and plasmonic substrates before and after the sensitization of PbS QDs were measured via scanning electron microscopy (SEM) equipped with energy-dispersive X-ray spectroscopy (EDS). Figure 2.3 gives the details of SEM image (top row, 250,000x, 10 kV), EDS element mapping images (middle row, 62,500x, 20 kV) and the corresponding spectrum (bottom row) of TiO_2 (the 1st column), TiO_2/Au/TiO_2 (the 2nd column), OP-1344/TiO_2 (the 3rd column) and OP-1344/TiO_2/Au/TiO_2 (the 4th column). Gold nanoparticles, with an average size around 20 nm, are well

dispersed on the TiO_2 surface without dissolution even after deposition of PbS QDs according to SEM images. Element mapping by EDS illustrates the uniform distribution of Ti (red) and Sn (green, coming from the FTO glass (F doped SnO)) elements on bare TiO_2 substrate, Au (orange) on plasmonic substrate and Pb (blue) on sensitized substrate. EDS spectrums based on the element mapping identify the existence of Au around 2.1 keV (orange area) in comparison with bare TiO_2 substrate, as well as the existence of Pb element at 2.34 keV (azure area) after sensitization even in the resolution limitation of SEM for the PbS QDs with average diameter less than 5 nm. PbS QDs was loaded 5 times of the maximum amount for the photocurrent measurements in order to get obvious counts for EDS.

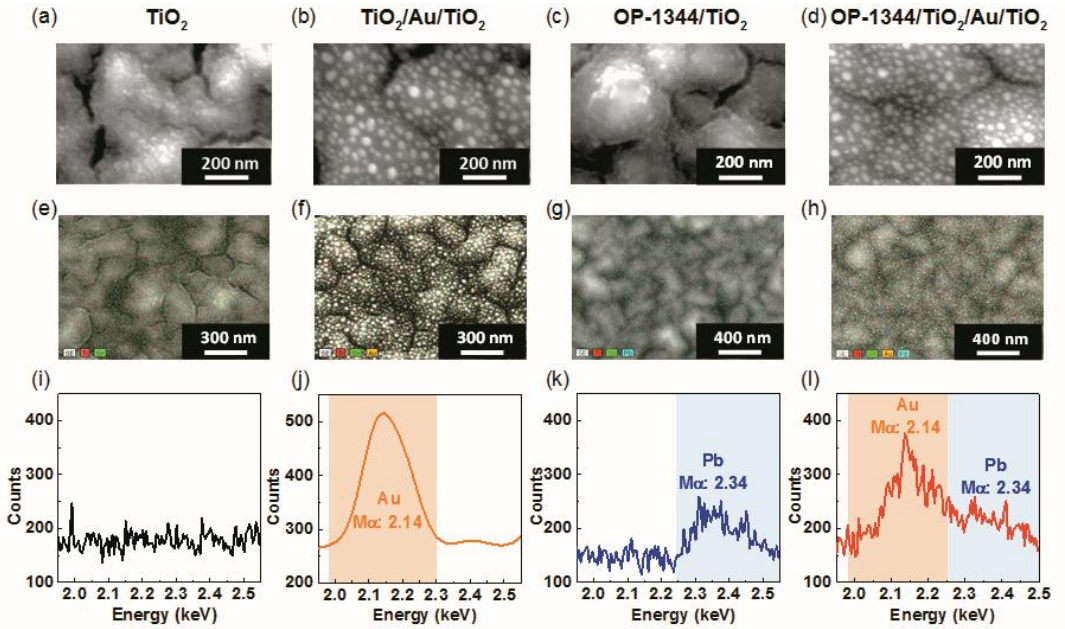

Figure 2.3. SEM images (top row), EDS mapping images (middle row) and corresponding spectrum (bottom row) of bare titanium dioxide and plasmonic electrode before and after sensitized by OP-1344 QDs: (a, e, i) TiO_2, (b, f, j) TiO_2/Au/TiO_2, (c, g, k) OP-1344/TiO_2 and (d, h, l) OP-1344/TiO_2/Au/TiO_2 substrate. Element mapping involved in gold M_α (orange), lead M_α (blue), titanium K_α (red) and tin L_α (green, coming from FTO glass) emission (PbS particle density: 5.5E+12 cm^{-2}). EDS spectrums were enlarged in low energy region to identify the existence of gold and lead.

2.3.2 Size-dependent optical and electric properties of colloid PbS QDs

Absorption and emission spectra of the colloid oleic acid (OA)-capped PbS QDs dispersed in hexane and ligand exchanged with 3-mercaptopropionic acid (MPA)-capped PbS QDs in methanol were obtained (Figure 2.4a), giving the 1st exciton peak from near-infrared to visible. These PbS QDs were

named according to the absorption maximum, as OP-1344, OP-1101, etc. Their average bandgap (E_g) were determined by the 1st exciton peak as 0.9, 1.1, 1.4, 1.6, 1.7, 1.8 and 2.3 eV. The average diameters were estimated to be 4.8, 3.7 2.7, 2.4, 2.3, 2.1 and 1.6 nm in diameter[13] respectively in reference of the 1st exciton peak (Figure 2.4c). Within the Bohr radius of 18 nm, all these PbS QDs exhibit strong quantum confinement especially the smallest OP-682 with a larger bandgap. The emission maximum was marked as black respectively. The Stokes shift between emission and absorption maximum became larger as the increase in bandgap energy (Figure 2.4b), because of the size-dependent vibrational relaxation based on quantum confinement.[15]

The valence and the conduction band-edges of PbS QDs were calculated according to the size-dependent ionization energy and values of bulk PbS (E_g=0.41 eV, E_{CB}=-0.29 V, E_{VB}=0.12 V (vs. Ag/AgCl))[16]. The uncertainty in the energies of QDs is the full width at half-maximum of the absorption peaks that yielded E_g (Figure 2.4c). The flat-band potential (U_{FB}) of anatase TiO_2 prepared by the LPD method is around -0.7 V (vs. Ag/AgCl) in alkane solution with pH=13 considering the band-edge shifts for 0.059 V/ pH at 298 K.[17, 18] Based on the simplest model of infinite surface-barrier quantum confinement (i.e., article-in-the-box), the CB and VB shifts are inversely proportional to the effective mass of the electron (m_e*) and hole (m_h*), respectively, as $\Delta E_{CB}/\Delta E_{VB}=m_h^*/m_e^*$. For PbS QDs, CB possesses a larger energy shift as m_e* is less than m_h*.[19] Strong quantum confinement enlarges the CB of OP-682 to a more negative potential than U_{FB} of TiO_2 whereas the CB of infrared OP-1344 is almost the same as the U_{FB} of TiO_2, indicating electron injection from excited OP-1344 faces much more difficulties rather than the two others. The observed photocurrents are ascribed to the electron injection into the conduction band of TiO_2 from excited PbS QDs accompanied by electron transfer from the donor of sulfide redox in the electrolyte under positive polarization for effective charge separation[20] (Figure 2.4c).

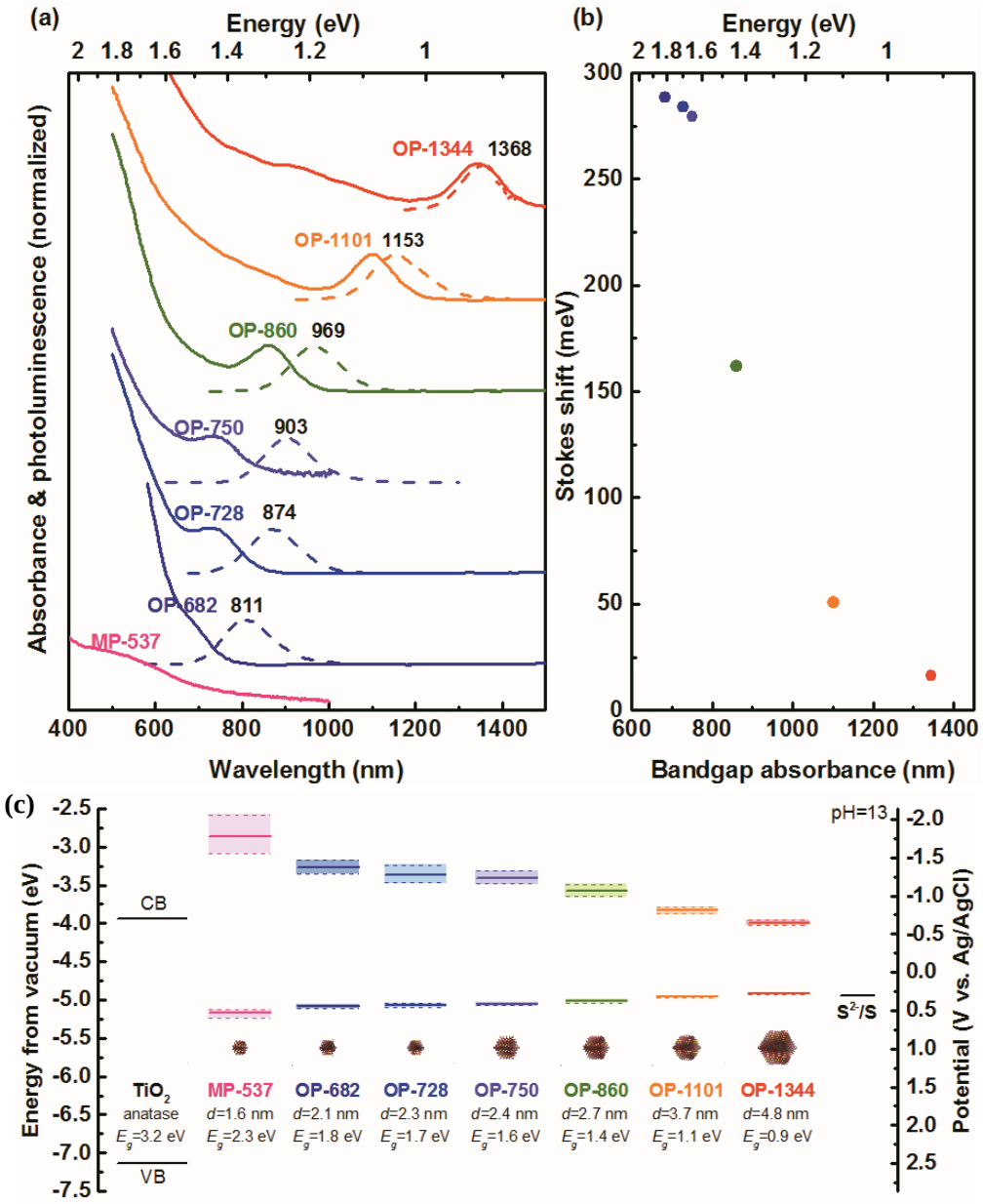

Figure 2.4. (a) Size-dependent absorbance and emission of colloid PbS QDs dispersed in hexane with 1st exciton wavelength (marked in color) and emission maximum (marked in black). (b) Size-dependent Stokes shift between the band maximum of the absorption and emission spectra. (c) Band-edge energies of PbS QDs calculated in regard to the average size. The color boxes indicate the uncertainty in the energies of QDs determined by the full width at half-maximum of the 1st exciton peaks. The flat band energy of TiO_2 with respect to Ag/AgCl (sat.KCl) refer to anatase in alkaline aqueous solution (pH=13).

2.3.3 Substrate-dependent emission spectrum of OP-1101

Figure 2.5 present the photoluminescence of OP-1101 excited by light with wavelength of 570 nm

(green) and 900 nm (black) on cover glass (Figure 2.5d) and photoelectrochemical cells including bare TiO_2 (Figure 2.5c), PbS QDs directly contacting Au NPs (Figure 2.5b) and the 2nd layer of TiO_2 separated Au NPs (Figure 2.5a) measured in air. Compared to PbS QDs on cover glass without any quenching nor electron injection process, apparent decline of photoluminescence was observed for the other three systems, especially for OP-1101/TiO_2 substrate (Figure 2.5a) because of electron injection from excited PbS QDs into the conduction band of TiO_2. As for the excitation by 570 nm among the LSPR region, existence of Au NPs enhanced the photoluminescence by comparing OP-1101 sensitized TiO_2/Au/TiO_2 with TiO_2 (green, Figure 2.5a and c). Photoluminescence of OP-1101 on TiO_2/Au/TiO_2 and Au/TiO_2 by 570 nm is respectively 6,000 and 6,500 cps, in contrasted to 9500 cps of OP-1101 on cover glass, the decrease is accounted for electron injection to TiO_2 and quenching in proximity to Au NPs by Forster energy transfer,[7, 9] respectively. The peak around 1070 nm could be ascribed to the interference of emission light caused by the thickness of both the TiO_2 layers as well as the glass substrates.

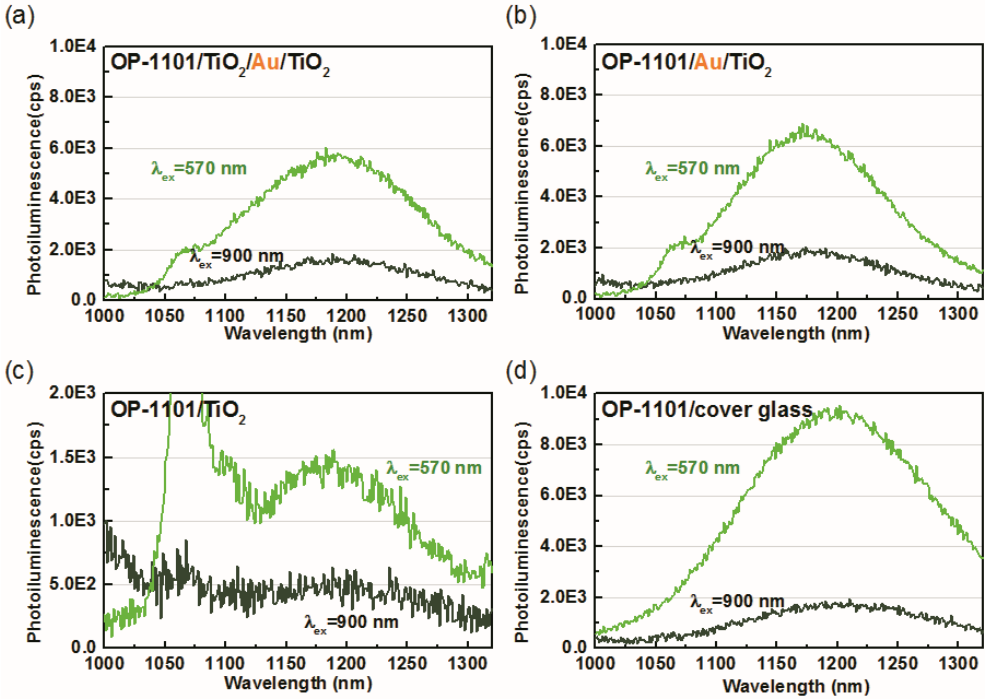

Figure 2.5. Photoluminescence of OP-1101 sensitized (a) TiO_2/Au/TiO_2, (b) Au/TiO_2 (c) TiO_2 and (d) cover glass excited by 570 nm (green) and 900 nm (black) with multiples of the emission maximums. PbS particle density: 4.8×10^{12} cm^{-2}.

2.3.4 Potential-dependent fluorescence spectrum and simultaneous photocurrent

Photoluminescence, the radiated process for the recombination of electron-hole pair generated by light irradiation with energy larger than the bandgap, also plays significant role in PbS QDs sensitizing photoelectrochemical cell system besides the process of electron injection into the conduction band of TiO_2. The overall amount of electron-hole pairs including the electrons undergoing electron injection and photoluminescence processes keep as constant under light irradiation with a constant intensity. As the Fermi level of the system is able to be controlled by a polarized potential of the three-electrode system, the amount of excited electron injected into TiO_2 is tunable so that the simultaneous photoluminescence counterpart will present opposite changing tendency as if the loading amount is extremely low within a single layer regime. A positive potential benefits the electron injection leading to the effective charge separation. The process also contributes to the prevention of the charge recombination. Thus, decreased photoluminescence intensity is expected.

2.3.4.1 OP-1101/TiO_2/Au/TiO_2

Figure 2.6 shows the photoluminescence and simultaneous photocurrents of OP-1101/TiO_2/Au/TiO_2 (left column) and OP-1101/TiO_2 (right column) measured under potential from -0.6 to +0.5 V with excitation wavelength of 450, 500 and 550 nm. Slight change in photoluminescence was observed, as shown in potentials of -0.5 and +0.3 V (insets in Figure 2.6a and d). Figure 2.7 shows the potential-dependent average photoluminescence from 1100 to 1300 nm (a, b) and the simultaneous photocurrents (c, d). As the potential polarized to positive direction, apparent decreased photoluminescence with increased photocurrent were simultaneously obtained because of the enlarged potential gradient in TiO_2 modified by the Fermi level. The potential-dependent decline of photoluminescence presented almost a linear tendency for OP-1101/TiO_2 by the excitation of 450 nm and a second increasing step of photocurrent after the saturation as the potential larger than 0 V. For OP-1101/TiO_2/Au/TiO_2, the decline in photoluminescence became saturated as the potential larger than 0 V and the 2nd increasing step of photocurrent was not as obvious as that for 1101/TiO_2. Enhanced photocurrents were produced by the plasmonic substrate excited by wavelength in the range of 500~

600 nm owing to the LSPR effect. Fairly large photocurrents were collected by the relatively large irradiation light intensity compared with previous IPCE measurements in our lab, leading to probable photocharging-induced 2nd increment in photocurrent, especially for high energy irradiation of 400 and 450 nm. In addition, the absence of enhancement in photoluminesce may be accounted for quenching process or the coupling between Au NPs and multilayered PbS QDs resulted from a relatively large loading amount.

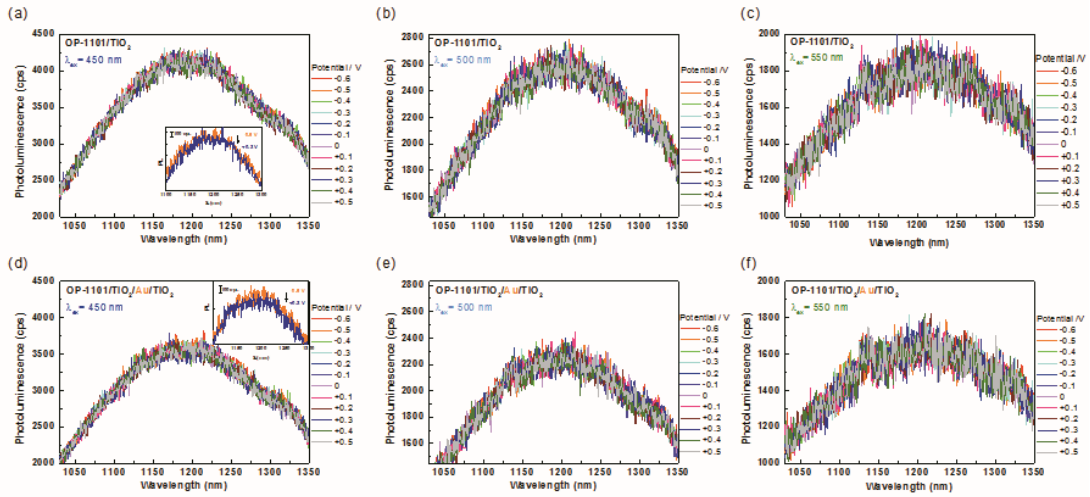

Figure 2.6. Emission spectrum of OP-1101 sensitized TiO_2 and TiO_2/Au/TiO_2 substrates under excitation of 450 nm (a, d), 500 nm (b, e) and 550 nm (c, f) under polarized potential from -0.6 V to +0.5 V. Insets (a, d) show the enlarged photoluminescence under potential of -0.5 V (orange) and +0.3 V (navy). The particle density of OP-1101: 1.2E+12 cm^{-2}.

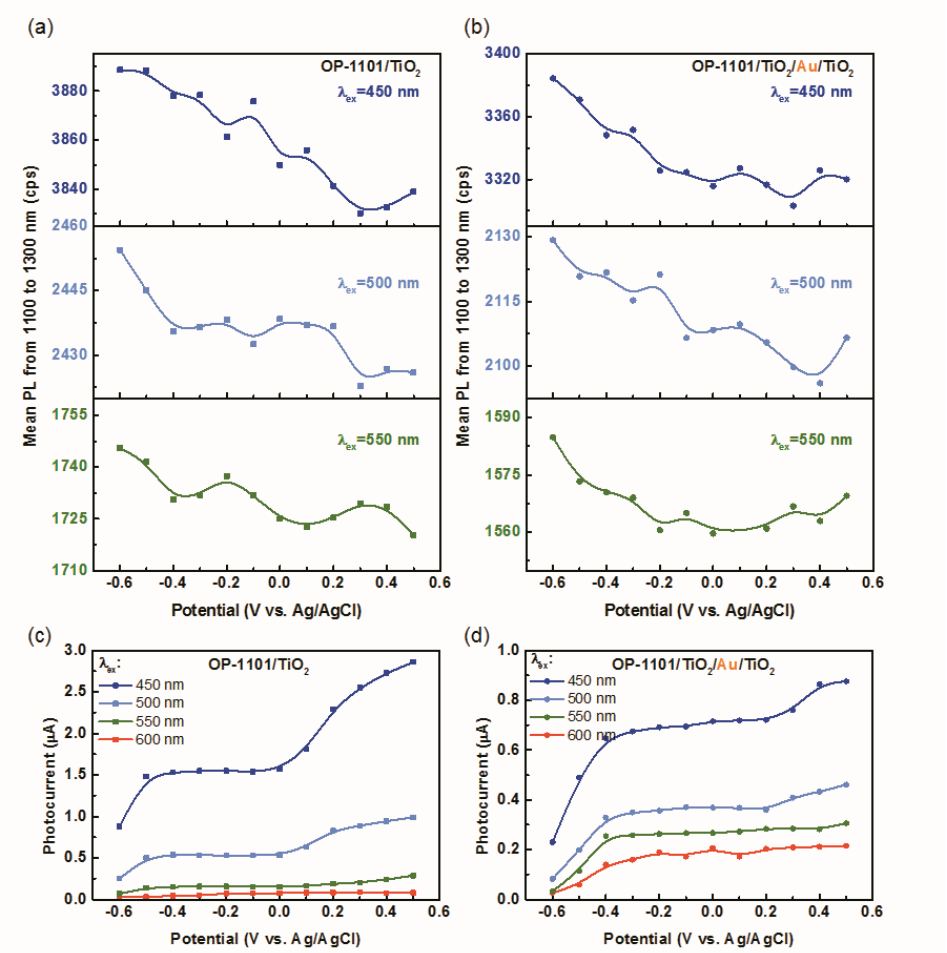

Figure 2.7. Potential-dependent (a, b) average photoluminescence from 1100 to 1300 nm and (c, d) simultaneous photocurrent for OP-1101 sensitized TiO_2 (square) and TiO_2/Au/TiO_2 (circle) under excitation of 450 (blue), 500 (cyan), 550 (green) and 600 nm (red). The particle density of OP-1101: 1.2E+12 cm^{-2}.

2.3.4.2 OP-682/TiO_2/Au/TiO_2

Electrochemical fluorescence was also measured by OP-682 sensitized TiO_2 (Figure 2.8a, c) and TiO_2/Au/TiO_2 (Figure 2.8b, d) under potential from -0.8 to +0.5 V excited by blue (460-495 nm) or green (520-550 nm) visible light via an inverted microscopy occupied with fluorescence filter cubes. Three measurements under each potential with light-off time of 60 s were performed to improve the accuracy affected by photobleaching, and average values were extracted for the comparison. Fluorescence maximums around 700 nm were observed and the discrepancy in spectrums was ascribed to the filter cubes. Apparent decrease in photoluminesce was observed (insets in Figure 2.8). Figure

2.9 shows the potential-dependent average photoluminescence from 700 to 710 nm for the blue excitation (a, b) and from 685 to 695 nm for the green excitation (c, d) with the simultaneous photocurrent (e, f). The plasmonic substrate present saturation in photoluminesce decline as the potential positive than -0.4 V; while TiO_2 substrate present a linear decline over the whole potential range. The decline in photoluminesce is 3 % and 4.6% by the plasmonic substrate by blue and green excitation, respectively, less than that of 7% and 7.8% by TiO_2 substrate, indicating that the LSPR inhibited the recombination of electron-hole pairs. Enhancement in photocurrent collection by the LSPR was confirmed in contrast with OP-682 sensitized TiO_2, demonstrating the validity of LSPR in modification the photo-excitation process of PbS QDs.

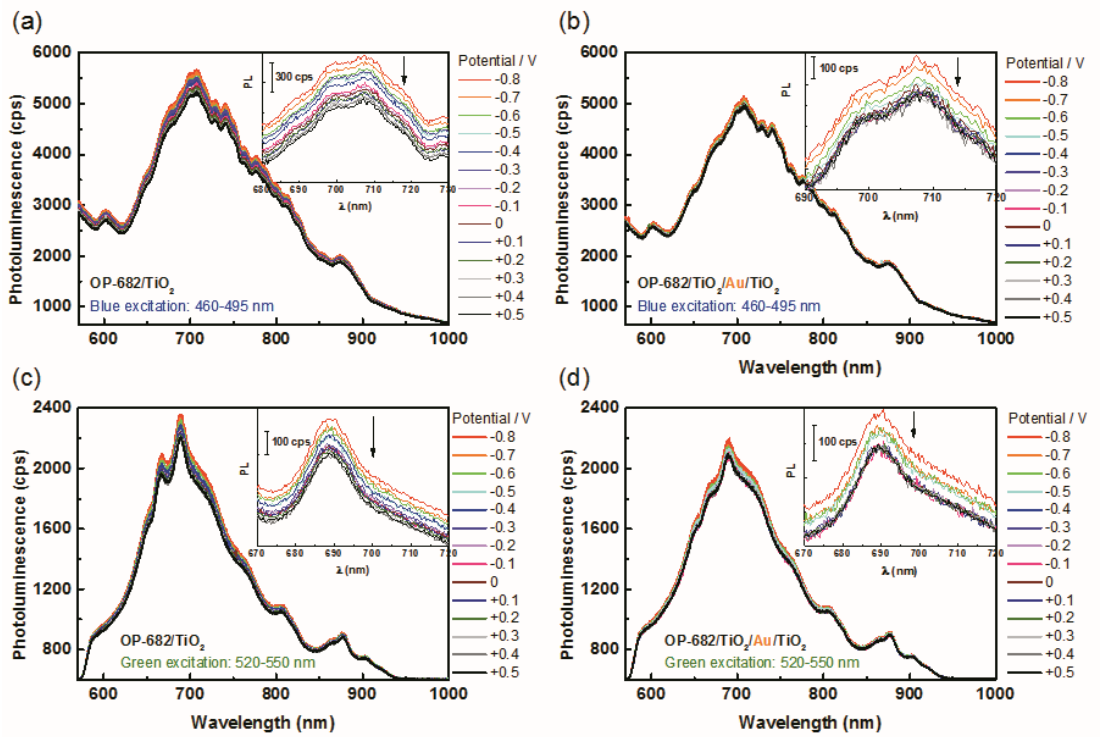

Figure 2.8. Emission spectrum of OP-682 sensitized TiO_2 (a, c) and TiO_2/Au/TiO_2 (b, d) substrates under blue (a, b) and green excitation (c, d) under polarized potential from -0.8 V to +0.5 V. Photoluminescence is the average value for three measurements at each potential under irradiation for 10 s and irradiation cut-off interval of 60 s. Insets show the enlarged emission spectrum with decreased photoluminescence as the potential polarized from negative to positive. The particle density of OP-682: 1.2E+12 cm^{-2}.

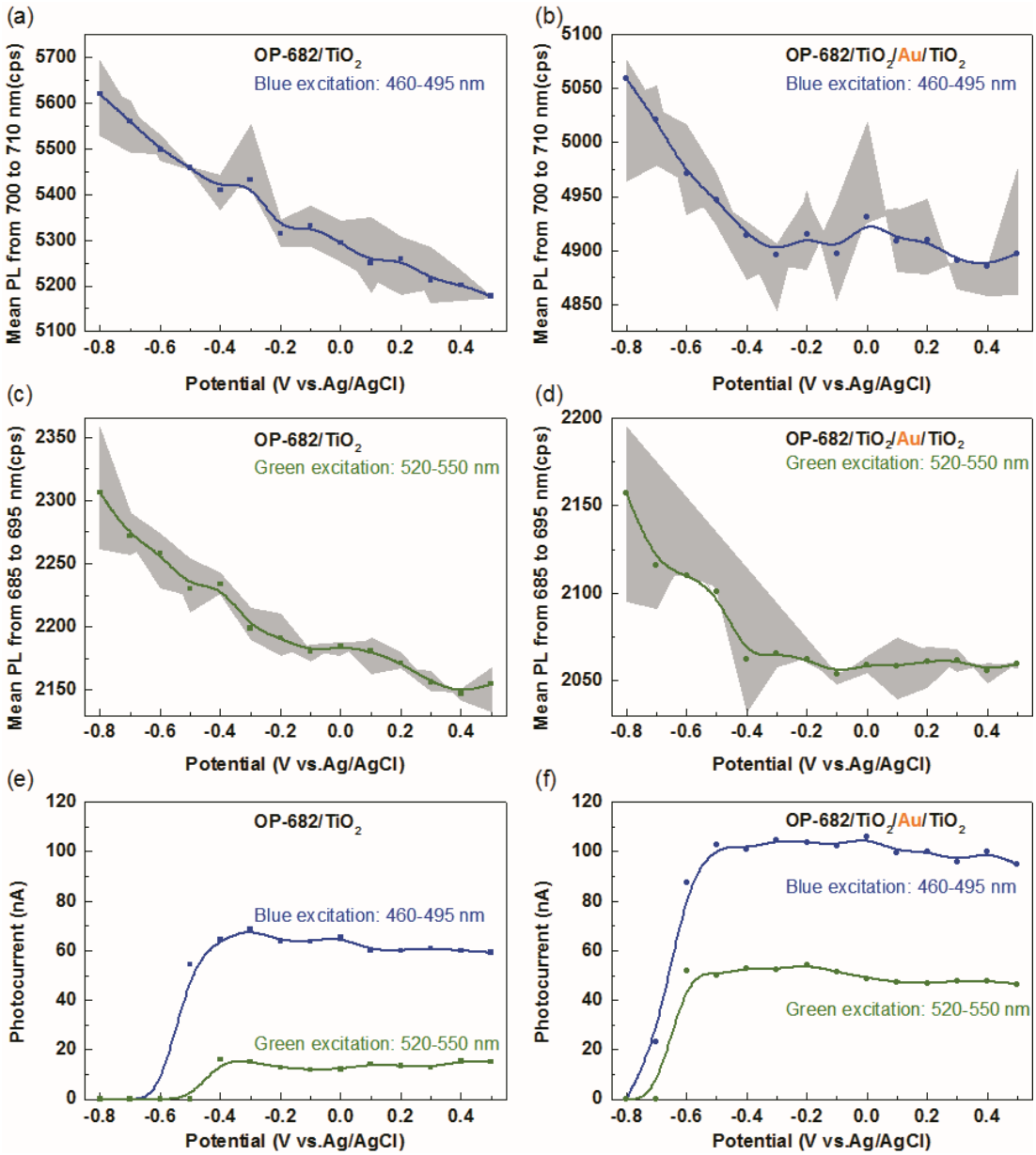

Figure 2.9. Potential-dependent average photoluminescence of OP-682 sensitized TiO_2 (left column) and TiO_2/Au/TiO_2 (right column) from 700 to 710 nm for the blue excitation (a, b) and from 685 to 695 nm for the green excitation (c, d) with the simultaneous photocurrent (e, f). Grey areas present the photoluminescence of three measurements under each potential.

2.3.5 Potential-dependent fluorescence imaging of OP-682 sensitized plasmonic electrode

Fluorescence image mapping of OP-682/TiO_2/Au/TiO_2 electrode was performed under potetnial polarization. Differential photoluminescence image in reference with -0.7 V by the blue excitation (Figure 2.10 a) illustrates the alternation in photoluminesce of each point under irradiation. In contrast with the photocurrent obtained from the whole area irradiated (red line in Figure 2.10 b), a typical point (marked as a black circle in Figure 2.10 a) from the mapping area was extracted to exemplify the decline of photoluminescence as the potential polarized from -0.7 V to -0.2 V (black squre line in Figure 2.10 b and a 3-D image mapping in Figure 2.10 c to e). As the fluorescence image mapping was perfomed after the 3 measurements of the spectrum, photobleaching could influnce the photoluminesce intensity. Inhomogeneous spatial distribution of the fluorescence suggests the contribution of Au nanostructures to the enhanced light absorption, emission and the quenching processes at the electrodes.

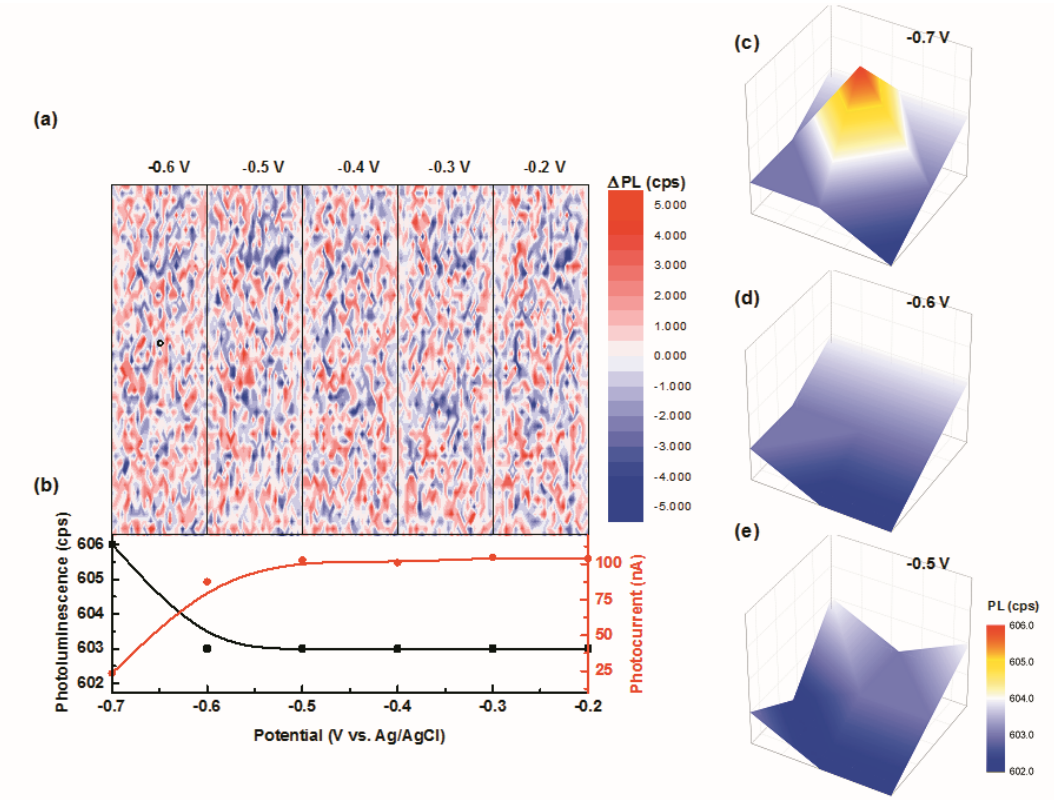

Figure 2.10. (a) Differential photoluminescence image of OP-682/TiO_2/Au/TiO_2 based on -0.7 V by the blue excitation in exposure of 1 s. (b) Potential dependent photoluminescence of a point (marked as black circle) and photocurrent (red). (c) 3D-image of the point under potential of -0.7 (c), -0.6 (d) and -0.5 V (e).

2.4 Conclusions

In summary, optical and electronic properties of size-controlled PbS QDs were characterized. The plasmonic photoelectrochemical cell with size-controlled PbS QDs were also characterized by SEM-EDS, absorption and emission spectroscopy. Photoluminescence of PbS QDs sensitized TiO_2/Au/TiO_2 present both plasmon enhancement and quenching effect compared to PbS QDs/TiO_2. Electrochemical luminescence of OP-1101 and OP-682 on TiO_2/Au/TiO_2 show apparent potential-dependent photoluminescence and simultaneous photocurrent, confirming that LSPR enhanced exciton generation and modified recombination. The variation of the Fermi level controlled by the electrode potential resulted in the charge separation efficiency, leading to the change in the efficiency of electron-hole separation and recombination in PbS QDs. The potential dependence provide the information on the band diagram of PbS QD/TiO_2 interface predicted by the optical and electronic properties of size-controlled PbS QDs in solutions. Fluorescence imaging of OP-682/TiO_2/Au/TiO_2 present the potential-dependent alternation of photoluminescence showing inhomogeneous distribution.

References

1. de Torres, J.; Ferrand, P.; Colas des Francs, G.; Wenger, J. *ACS Nano* **2016,** 10, (4), 3968-3976.
2. Achermann, M. *The Journal of Physical Chemistry Letters* **2010,** 1, (19), 2837-2843.
3. Ming, T.; Chen, H.; Jiang, R.; Li, Q.; Wang, J. *The Journal of Physical Chemistry Letters* **2012,** 3, (2), 191-202.
4. Song, J.-H.; Atay, T.; Shi, S.; Urabe, H.; Nurmikko, A. V. *Nano Letters* **2005,** 5, (8), 1557-1561.
5. Zhou, D.; Liu, D.; Xu, W.; Yin, Z.; Chen, X.; Zhou, P.; Cui, S.; Chen, Z.; Song, H. *ACS Nano* **2016,** 10, (5), 5169-5179.
6. LeBlanc, S. J.; McClanahan, M. R.; Jones, M.; Moyer, P. J. *Nano Letters* **2013,** 13, (4), 1662-1669.
7. Pons, T.; Medintz, I. L.; Sapsford, K. E.; Higashiya, S.; Grimes, A. F.; English, D. S.; Mattoussi, H. *Nano Letters* **2007,** 7, (10), 3157-3164.
8. Zhang, X.; Marocico, C. A.; Lunz, M.; Gerard, V. A.; Gun'ko, Y. K.; Lesnyak, V.; Gaponik, N.; Susha, A. S.; Rogach, A. L.; Bradley, A. L. *ACS Nano* **2012,** 6, (10), 9283-9290.
9. Li, M.; Cushing, S. K.; Wang, Q.; Shi, X.; Hornak, L. A.; Hong, Z.; Wu, N. *The Journal of Physical Chemistry Letters* **2011,** 2, (17), 2125-2129.
10. Nozik, A. J. *Annual Review of Physical Chemistry* **1978,** 29, (1), 189-222.
11. Bard, A. J. *Science* **1980,** 207, (4427), 139-144.
12. Hines, M. A.; Scholes, G. D. *Advanced Materials* **2003,** 15, (21), 1844-1849.

13. Moreels, I.; Lambert, K.; Smeets, D.; De Muynck, D.; Nollet, T.; Martins, J. C.; Vanhaecke, F.; Vantomme, A.; Delerue, C.; Allan, G.; Hens, Z. *ACS Nano* **2009,** 3, (10), 3023-3030.
14. Oh, J. K.; Lee, J. Y.; Lee, H. Y.; Kim, S. G.; Han, C.; Shin, J. K. *Geosystem Engineering* **1999,** 2, (1), 1-6.
15. Ushakova, E. V.; Litvin, A. P.; Parfenov, P. S.; Fedorov, A. V.; Artemyev, M.; Prudnikau, A. V.; Rukhlenko, I. D.; Baranov, A. V. *ACS Nano* **2012,** 6, (10), 8913-8921.
16. Jasieniak, J.; Califano, M.; Watkins, S. E. *ACS Nano* **2011,** 5, (7), 5888-5902.
17. Kavan, L.; Grätzel, M.; Gilbert, S. E.; Klemenz, C.; Scheel, H. J. *Journal of the American Chemical Society* **1996,** 118, (28), 6716-6723.
18. Beranek, R. *Advances in Physical Chemistry* **2011,** 2011.
19. Tsidilkovski, I. M., Chapter 2 - Band Structure of Important Semiconductors. In *Band Structure of Semiconductors*, Pergamon: **1982**; Vol. 19, pp 77-200.
20. Chakrapani, V.; Baker, D.; Kamat, P. V. *Journal of the American Chemical Society* **2011,** 133, (24), 9607-9615.

Appendix

A2.1 Quantities analysis of PbS QDs

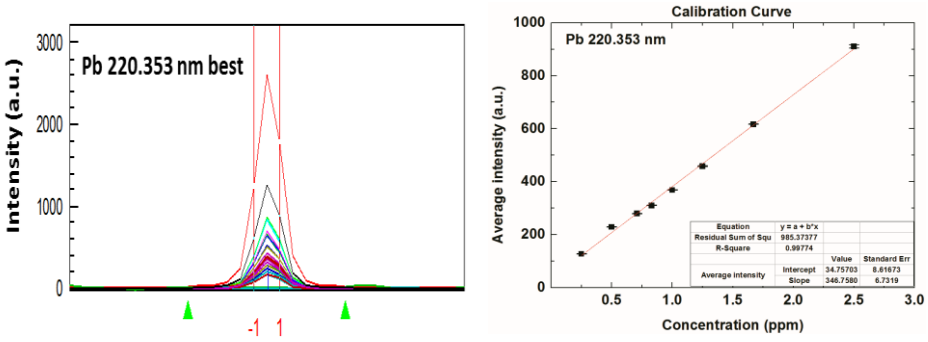

Figure A2.1. Results of concentration-dependent Pb atom emission peak intensity. (Left) Measured results and (right) the calibration curve.

Table A2.1. Details of ICPE results and calculated mole concentration of PbS according to detection wavelength of 220.353 nm

Sample	Diluted conc.		Average	RSD
file	ppm	fold	a.u.	%
cal1	0	Solvent	1.58	42.39
cal2	0.25	20	127.18	0.84
cal3	0.50	10	228.87	0.17
cal4	0.71	7	279.42	0.26
cal5	0.83	6	309.71	0.28
cal6	1.00	5	368.15	0.07
cal7	1.25	4	458.32	0.25
cal8	1.67	3	616.56	0.15
cal9	2.50	2	910.11	0.7
cal10	5.00	-	1855.65	0.05

Table A2.2 Calculated mole concentration of PbS

Sample	Average	RSD	Calculated Conc.	Conc. of PbS in original solution	Mole Conc. of PbS in original solution
file	a.u.	%	ppm	ug/uL	umol/mL
Blank	0.18	244.96	-	-	-
OP-682	169.05	1.01	0.387	11.18	46.7
OP-728	221.26	1.11	0.538	37.27	155.7
OP-750	114.81	0.92	0.231	5.33	22.3
OP-860	269.16	0.25	0.676	31.23	130.5
OP-1101	258.31	0.11	0.645	18.61	77.8
OP-1344	206.04	0.34	0.494	19.97	83.4

A2.2 EDS mapping spectrum

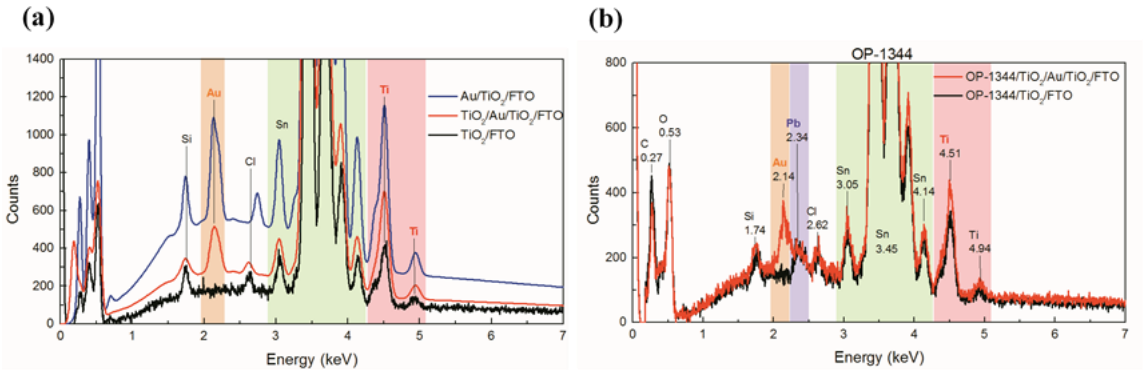

Figure A2.2. EDS spectrum of bare titanium dioxide and plasmonic electrode (a) before and (b) after sensitized by OP-1344 QDs (PbS particle density: 5.5E+12 cm^{-2}).

Chapter 3

Characteristic Electronic Excitation of PbS Quantum Dots at the Gap of Au Nano-Dimer Monitored by Surface-Enhanced Raman Scattering

3.1 Introduction

Colloid semiconductor quantum dots (CQDs) provide a considerable advantage of tunable electronic properties with variation in size, shape, and composition though diverse synthetic techniques[1-3]. Over the years, numerous efforts have been made to control size-dependent intrinsic properties covering biexciton quantum yield[4, 5] or fluorescence blinking,[6-8] excited-state lifetime and polarization,[9] Auger process[10-12] or reversed Auger process known as multiple exciton generation,[13-18] intraband relaxations,[19-21] for various species of QDs such as pure core colloid QDs and core/shell QDs including alloy composition at the core/shell interface across II-VI, III-V and IV-VI semiconductors.

Besides intrinsic properties of CQDs, the surface and environmental properties also play an important role in CQDs' numerous applications.[22] Type of organic adlayers serving as surface passivation affect electronic or optical properties of QDs, such as electronic band structures,[23, 24] exciton dissociation,[25-27] surface-mediated charge trapping[28-31] and electron transfer rate from excited QDs to solar cell;[32, 33] conversely, excitation of QDs can influence vibrational modes of capping ligands in turn. Recently, surface-ligand bonding has been well studied[34-39] but the effect of size-dependent exciton-vibrational coupling remains unknown. Since pure core CQDs exhibit similar delocalization of the electron and hole radial distribution functions with minor penetration to the surrounding beyond the dot boundary, consequently promoting an overlap with the ligand electronic or vibrational states.[40]

The discovery of surface-enhanced Raman spectroscopy/scattering (SERS) has opened a new avenue for molecule detection thanks to the breakthrough in limited sensitivity of Raman spectroscopy. Enhancement of Raman scattering cross-section of molecules adsorbed on noble metallic nanostructures has been attributed to two major effects: electromagnetic enhancement (EM) through

interaction with surface plasmon excitations and chemical enhancement (CM) through charge transfer interaction of the absorbed molecule with the metal surface.[41-43] Supplemented to noble metal, semiconductor QDs have also been validated the enhancement with a factor on the order as high as 10^3-10^6.[44-46] Benefiting from relatively weak exciton binding energy, lead sulfide (PbS) gives electron-hole pair easily via bandgap excitation.[47] Furthermore, relatively small and almost equivalent effective mass of electron and hole initiate strong quantum confinement of both electron and hole as if size is controlled less than the relatively large Bohr radius of 18 nm.[48] PbS QDs play a notable role in SERS both by physical and chemical mechanism: PbS QDs intensely enhance the electromagnetic field generated by localized surface plasmon resonance,[49] and charge transfer to surfactant thus modify Raman spectrum.[50] Electrochemical surface-enhanced Raman scattering (EC-SERS), a system generally consisting nanostructured electrodes and electrolyte, provides specific features in molecule characterization and identification because the alteration in applied electrode potential can easily change the Fermi level of metal, dielectric constant of interfacial electrolyte, the coverage and/or the adsorption orientation of the molecule and bonding interaction of the molecule with the surface, and consequently influence on both physical and chemical enhancements to some extent.[51] However, best to our knowledge, characterization of PbS QDs by EC-SERS has not been reported to date.

Oleic acid (*cis*-9-octadecenoic acid: OA) is one of the major surfactant used to stabilize PbS quantum dots (QDs) during the synthesis procedure of the precursor-rapid-injection method[52], forming strong chemical bond between the carboxylic acid and the lead atoms and thus reducing the surface energy of the QDs. However, previous studies on OA by Raman scattering were focused on the transitions of crystalline phases at deliberately dropped temperature[53, 54] and no publications by EC-SERS have reported OA served as capping ligand, so that it is hardly to know the interaction between the single nanoparticle and surfactant from the "complicated" results given by nanoparticles systems.

In this chapter, we studied SERS spectra of OA molecule as surface function of various sizes of PbS QDs coupled with gold nanodimers (NDs) fabricated via angle-resolved nanosphere lithography (AR-NSL) under near-infrared light irradiation both in air as well as in electrolyte environment. Modified spectra of OA were observed thanks to the improved polarizability by the enhanced electric field generated by the PbS QDs-Au NDs system. The binding mode between carboxylate head and Pb atoms

was determined as bridging bidentate for all PbS QDs varied in size according to anti- and symmetric stretching of COO^-. Notably, size-dependent Raman shift of vibrational modes approaching to carboxyl bond was considered stemming from size-controlled excitation of PbS QDs involving hole trapping in surface dangling induced states. And negative potential-induced change in vibrational modes was ascribed to electron transfer and variation in bond strength of OA in the ultra-small space between QDs and metal surface. Size-dependent LO phonon mode of PbS QDs was investigated owing to phonon confinement assisted by the near-field of LSPR. The observed competition between phonon emission and energy transfer to ligand vibrations confirms various pathways for intraband relaxation, and highlights the advantage of the size-tunable CQDs-plasmon coupling system in the exciton-vibrational coupling regime.

3.2 Experimental

3.2.1 Preparation of Au-NSL substrate:

The detailed procedure has been reported in our previous publications.[55, 56] Briefly, gold nano-dimer substrate was fabricated via angle-resolved nanosphere lithography (AR-NSL). Polystyrene microspheres (PS beads) with average diameter of 200 nm was dispersed on a well washed hydrophilic ITO glass.[57] Triangle Au dimer arrays were deposited via electric beam vaporization (quartz crystal monitor CRTM-6000, ULVAC; 3KWE-type electron gun, ANELVA; compound molecular pump TG-800F-B, OSAKA Vacuum Ltd.) between the gaps of the PS beads with well-adjusted repeated condition containing a deposition angle of $\pm 10^o$ and a thickness of 10 nm at a deposition rate of 0.20 nm/s. Then the PS beads were well washed in Milli-Q water via ultrasonic for 1 min.

3.2.2 Sensitization of PbS QDs

OA-capped PbS QDs (purchased or synthesized) was diluted in argon-degased dehydrated hexane. The above PbS QDs dispersion was drop-casted onto the surface of Au-NSL substrate. It was spread into a circle of about 2 cm^2 in diameter with a particle density of 1.7E+13, 1.2E+13, 1.8E+12 cm^{-2} for OP-728, OP-750 and OP-1101, respectively. After solvent evaporation, Raman measurements were

taken on these samples.

3.2.3 SERS measurement

Raman measurements were performed via an inverted Raman spectroscopy of Nanofinder®30 (Tokyo Instruments, SOLAR TII) with a 100x objective lens (Nikon TU Plan ELWD, NA=0.80, WD=4.5 mm). NIR laser light of 785 nm (E_{ex} =1.58 eV) was obtained from a diode laser (Vortex^{TM} 6000 laser controller, Tokyo Instruments). Polarized excitation light was obtained by using a half wavelength plate. The output laser intensity was tunable via a ND filter yielding an estimated spot size of irradiation, ~1 μm, and was measured via power meter (OPHIR Japan LTD.). Raman measurements were carried out at the backscattering configuration collecting the scattering photons. The CCD (CS230B CCD color camera with OLM PUS SZ-CTV and CA180 camera adapter, Teli) equipped with a cooler (solver, scanning probe microscope) resolution of 785 nm is 3.94 cm^{-1}. The silicon line at 520.8 cm^{-1} was used for the calibration. All the measurements were performed with laser exposure of 1 s under a constant temperature of 25 ^{o}C.

Electrochemical SERS measurement was performed via a three-electrode system in electrolyte of sodium hydroxide (NaOH) aqueous solution (pH=13). Hand-made Ag/AgCl (sal. KCl) and Pt narrow sheet were respectively used as the reference and counter electrodes. Negative polarized potential was well controlled by a potentiostat (HA-151B, Hokuto Denko) and an oscilloscope (TDS 2004B, Tektronix) and was selected in order to avoid oxidation reaction according to the Pourbaix diagram of galena. The Fermi level of Au-dimer will be tuned as changing the polarized potential. Samples were measured under laser irradiation for 1s.

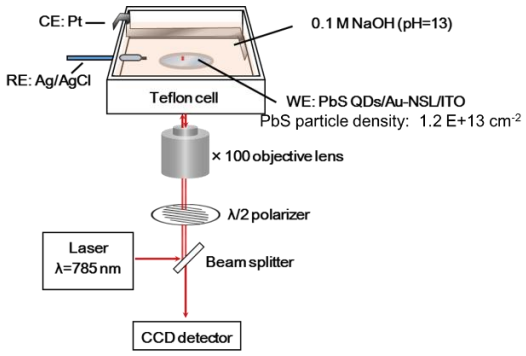

Figure 3.1. Schematic of the electrochemical SERS measurement

3.2.4 Finite-difference time-domain (FDTD) simulations

Finite difference time domain method (FDTD) of solving Maxwell equations was used to calculate nanoparticles extinction and electromagnetic field distribution. A commercial software, EEM-FDM (Ltd. EEM, Japan), was employed to carry out FDTD analysis for Au NP-PbS QD coupling system. Wavelength-dependent optical constants of bulk Au and bulk PbS were taken from the references[58, 59]. The systems were illuminated with a s-polarized plane wave with the electric field amplitude of 1 V/m. Boundary condition of perfectly matched layers (PMLs) were used to absorb the scattered radiation in all directions. The environment was set as the vacuum. Meshes were set sufficiently small in order to calculate local-field enhancements with sufficient spatial resolution; the details are listed as the following: 0.2 nm in the gap of Au NP-PbS QD as well as the space containing PbS QDs, 0.5 nm for the space containing bulk Au sphere, and 1 nm for the vacuum domain. The field was calculated as the ratio of its value at a given point relative to the incident field, $|E|/|E_0|$.

3.3 Results and discussion

3.3.1 Characterization via AFM and Absorption Spectrum

For fabricating metal nanostructures, physical methods such as evaporation or sputtering can avoid spectrum interference from surfactant of metal nanoparticles and thus improve SERS activity of the substrate. Angle-resolved nanosphere lithography (AR-NSL) enjoys great advantage in fabricating homogeneous arrays with controlled size, shape, and inter-particle spacing comparing with other physical techniques.[60] The structure of the Au nanodimer on ITO glass substrate was inspected by an atomic force microscope (AFM, Nanoscope-IIIa, Digital Instruments) in air. AFM image of Au-NSL illustrate the average size and thickness of the gold nano-dimer (Figure 3.2 top). Extinction spectrum of the Au nanodimer structure was measured by polarized light, giving longitudinal extinction peak around 785 nm (Figure 3.2 middle) which matches the excitation wavelength for Raman scattering, indicating an expected enhancement of Raman signals. The substrate was respectively sensitized by OP-728, OP-750 and OP-1101 as mentioned in Chapter 2.

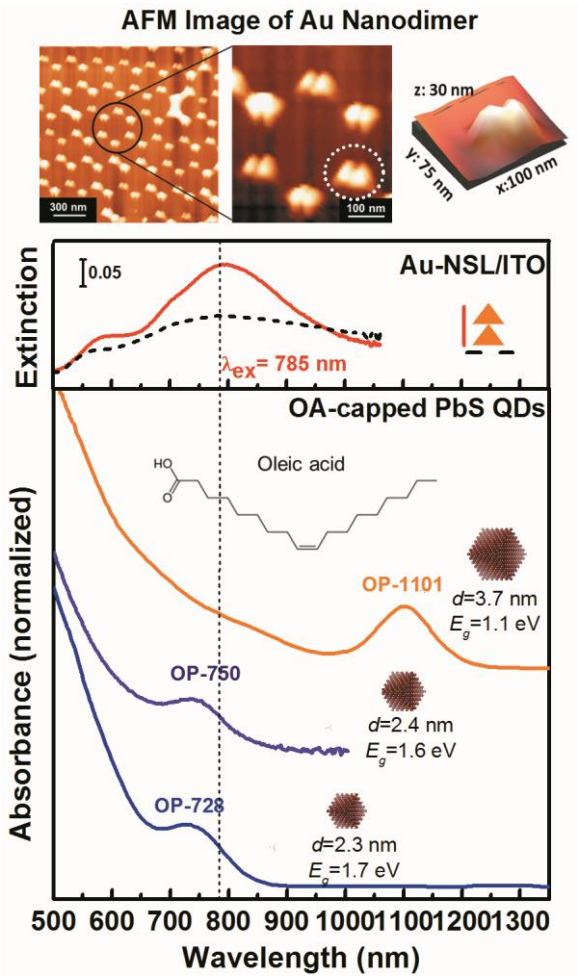

Figure 3.2. (Top) AFM image and (middle) extinction spectrum of Au nanodimer. (Bottom) Normalized absorption spectrum of size-controlled colloid PbS QDs respectively with 1st exciton peak around 1101 nm, (synthesized at 150 oC, marked as orange), 750 nm (purchased, marked as purple) and 728 nm (synthesized at 100 °C, marked as blue). Dotted line illustrated the excitation laser light at 785 nm.

3.3.2 SERS of Size-Controlled PbS QDs Measured in Air

3.3.2.1 Modified Spectrum of OA via SERS

Figure 3.3 illustrates the Raman spectroscopy of OA molecule (wine) and as capping ligand surrounding PbS QDs respectively with excitation wavelength of 728 nm (d=2.3 nm, blue), 750 nm (d=2.4 nm, purple) and 1101 nm (d=3.7 nm, orange) on Au-NSL under laser excitation of 785 nm measured in air, and assignments were summarized in Table according to references.[53, 54]

The neat liquid of OA on slide glass measured via normal Raman (Figure 3.3, green) in agreement

with the publication[61] exhibit broad peaks containing several overlapped vibrational modes across the whole spectrum due to the melt amorphous states in 25 °C in comparison with the vibrations of the crystallized γ phase measured in -18 °C (Figure 3.3, navy).[53] That is to say, normal Raman scattering can present much more meticulous peaks of OA molecule only carried on at a temperature lower than the melting point owing to the crystallization of OA molecule.

On the other hand, SERS signal of OA molecule both on Au-NSL substrate and as surface modification of PbS QDs displayed increased sensitivity for the vibrations which were detected by normal Raman including the Olefin group modes (C=C-H out-of-plane bending around 700 cm^{-1} and C=C-H in-plane bending at 1260 cm^{-1}) as well as the polymethylene modes (CH_3 rocking at 846 cm^{-1}, C-C stretching around 1060~1200 cm^{-1}, CH_2 twisting at 1295 cm^{-1} and CH_2 scissoring at 1432 cm^{-1}). Compared to the spectrum in -18 °C (navy), SERS measurements of PbS QDs on Au-NSL present distinctive vibrations consisting of the Olefin group modes at low Raman shift region (C=C-C bending around 570 cm^{-1} marked as azure), the Carboxyl group (C-C stretching modes around 900 cm^{-1} marked as pink, α-CH_2 bending around 1410 cm^{-1} marked as azure) and the polymethylene modes (CH_2 rocking around 1170 cm^{-1} marked as azure). Such phenomena demonstrate the validity of surface plasmon resonance in modified spectrum detection that previously only can be obtained at a low temperature.

In addition, vibrations of COO^- symmetric and anti-symmetric stretching[62, 63] respectively around 1370 and 1550 cm^{-1} (marked as orange and yellow respectively) instead of C=O stretching at 1645 cm^{-1} were observed, because OA molecule stabilizing PbS QDs form strong covalent-like bond between oxygen atom in the carboxylic acid and the lead atoms during the synthesis procedure of the precursor-rapid-injection method.[52] It has been reported[64-67] that the type of the interaction between the carboxylate head and the metal atom can be diagnosed by the anti-symmetric stretching especially by the wavenumber separation, Δ, between the anti- and symmetric stretching via IR: monodentate (Δ of 200~320 cm^{-1}), bridging bidentate (Δ of 140~190 cm^{-1}), chelating bidentate (Δ <110 cm^{-1}), and ionic interaction. Since IR and Raman share the same vibration frequency for an unforbidden vibration of molecule, in the present work, the Δ (188, 157 and 175 cm^{-1} respectively for OP-728, 750 and 1101)

is ascribed to bridging bidentate, where the interaction between the carboxyl group and the Pb atom is covalent (Figure 3.5).

Furthermore, such vibration modes of carboxylate were also observed for the OA/Au-NSL substrate as the carboxylic group can be easily chemisorbed on gold surface even under a self-assembly process.[68] A splitting of $\nu_{as}(COO^-)$ with Δ of 181 and 215 cm^{-1} as well as the significant O-H bending at 923 cm^{-1} indicated a mixed construction between OA molecules and gold nanodimers containing not only bridging bidentate and monodentate with Au atoms, but physical absorbed molecule without any chemical binding.

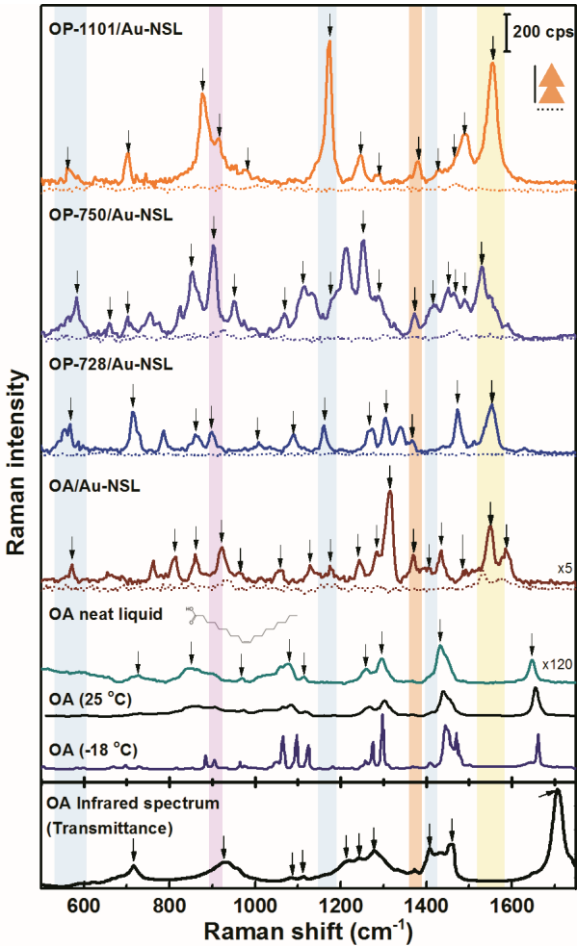

Figure 3.3. SERS spectrum of oleic acid molecule on Au-NSL substrate (wine) and as capping ligands surrounding PbS QDs with 1st exciton peak of 1101 nm (orange), 750 nm (purple), 728 nm (blue) on Au-NSL substrate; normal Raman spectrum of neat OA liquid on cover glass (green) and in publications measured at 25 (black, ref [61]) and -18 °C (navy, ref [53]). Infrared spectrum of OA neat liquid (bottom, ref[69]). SERS signals were irradiated and recorded for 1 s by a laser of 785 nm with the intensity of ~0.3 mW in air and were averaged for 3 times. The inevitable fluorescence background of

PbS QDs was subtracted. Normal Raman for OA neat liquid on glass was irradiated and recorded for 60 s by a laser of 13 mW. Laser intensity was normalized to 0.3 mW for all the measurements including parallel (solid line), perpendicular (dotted line) polarization and normal Raman. Distinct vibrational modes of OA surrounding PbS QDs are marked as: enhanced vibrations compared with neat liquid OA (azure areas); size-dependent shifted C-C (carboxyl) stretching (pink area) and COO^- symmetric stretching (orange area); and COO^- anti-symmetric stretching (yellow area).

Table 3.1 Raman-shift and modes assignments of oleic acid

Raman shift (cm^{-1})					Assignments	
OA neat liquid	OA	OP-728	OP-750	OP-1101		
on glass, in air	on Au-NSL, in air					
	572	568	583	564	C=C-C bending	Olefin group
			655, 702	701	C=C-H out-of plane bending	
723, 967	964	716	950	972	C=C-H out-of plane bending	
1260	1244	1272	1253	1245	C=C-H in-plane bending	
846	815, 860	860	825, 853	876	CH_3 rocking, chain-end tg, gg, gt	Polymethylene chains
	1062		1069		C-C anti-symmetric stretching	
1079		1088			C-C stretching, COOH-sided chain disordered	
1115	1129		1112		C-C stretching, CH_3-sided chain disordered	
	1175	1162	1194	1173	CH_2 rocking	
1295	1286,1315	1305	1289	1290	CH_2 twisting	
1432	1435, 1485	1472	1451, 1466, 1488	1468, 1490	CH_2 scissoring	
		898	905	914	C-C (carboxyl) stretching	Carboxyl group
	923				O-H bending	
	1410		1416	1425	α-CH_2 bending	
	1369	1366	1372	1380	COO^- symmetric stretching	
	1550,1584	1554	1529	1555	COO^- anti-symmetric stretching	
1645					C=O or C=C stretching	

Vibrational modes are marked in colors consistent with that in Figure 3.3 and 3.4a.

3.3.2.2 Distinct Enhancement and Size-Dependent Raman Shift by PbS QDs

Besides the spectrum modification of vibrations related to the carbon skeleton contiguous the Au NDs, vibrational modes of OA molecule closed to PbS QDs were also examined. In contrast with neat liquid of OA, OA/Au-NSL (Figure 2) and PbS QDs/glass (see Figure S1 in SI), PbS QDs-coupled Au-NSL system created an unique vibration of C-C (carboxyl) stretching around 900 cm^{-1}, a vibrational position closed to the COO-Pb bond but far away from the surface plasmon. Such enhancement definitely evidenced that PbS QDs further enhanced the electromagnetic field generated by localized surface plasmon resonance (Figure 4), a phenomenon which have been proposed by FDTD simulation[49] and confirmed by photo-electrochemical measurements.[32] Moreover, the frequency of this C-C (carboxyl)

stretching band blue-shifted by as much as 16 cm^{-1} as the bandgap exciton wavelength altered from 728 to 1101 nm. Similar blue-shifted phenomena were also observed for COO^- symmetric stretching as well as α-CH_2 bending (orange and pink in Figure 2 and 3a, respectively).

The reason to explain such tendency can be considered from variation in charge density of COO^- bond induced by a different interband excitation degree of PbS QDs under a NIR laser. As the distribution of charge density in a molecule influences its vibrational spectrum, ligand−QD interaction rationally leads to a significant redistribution of electron density according to Mulliken charges of ligand atoms calculated by DFT. [70] A carboxyl group can only passivize nonbonding Pb^{2+} ion on a QD's surface, leaving S^{2-} ion as dangling bond and forming valence-band-associated surface trap states.[28] When PbS QDs are excited (process 1 in Figure 4) and create electron-hole pairs, the surface trap will capture the hole escaping to the surface (process 5 in Figure 4), consequently reducing the repulsive force between S^{2-} and COO^-, and moving the electron cloud of O atoms towards Pb atoms. As a result, the electrostatic interaction contributes to enriching the COO^- bond strength so that frequency of the symmetric stretching bond blue-shifts. Such inductive effect become much more significant for OP-1101 rather than OP-728 as the former enjoys completely excitation by a NIR laser of 785 nm while only partial to the latter can be excited due to a wide size distribution (Figure 3b, CB and VB were calculated according to size-dependent properties[71]).

In addition, besides the size-dependent excitation, another reason for the large blue-shifted vibrations by OP-1101 is considered from a larger amount of trapped holes additionally produced by the LSPR near-field. Since a QD with an increasing size can boost the enhancement in electromagnetic field engendered by a noble metal particle (as roughly illustrated as the background in Figure 4) owing to improved scattering efficiency by a larger size,[49] consequently, instead of OP-728 and OP-750, OP-1101 intensify the near-field most and the near-field contrariwise augments the generation of electron-hole pairs as confirmed by photoelectron collection[32] as well as a quenched luminescence intensity compared with PbS QDs on a slide glass (see Figure S1 in SI).

On the other hand, OP-750 produced the most meticulous spectrum by coupling with gold nanodimer, whereas OP-728 generated a similar spectrum compared with OA/Au-NSL and vibrations

involving carbon skeleton around 1000~1130 cm was seldom detected for OP-1101. A plausibly explanation is that the electron transfer from excited QDs to Au NDs complicates the polarizability of the C-C bonds to some extent (process 2 in Figure 4). In a view of dynamics, molecular vibration lifetime around tens of femtosecond[72] is comparable with the same time scale of electron injection, such as several femtoseconds from excited PbS QDs into TiO_2,[73] indicating that a fast electron transfer will intensely influence molecule vibrational scattering by transiently inducing or redistributing electron clouds of OA molecule and modifying dipole moment of relevant vibrational modes. Variations in polarizability by highly arrayed Au nanodimer is also ascribed for deficiency in detecting vibrations above 2800 cm^{-1} for all the SERS measurements.

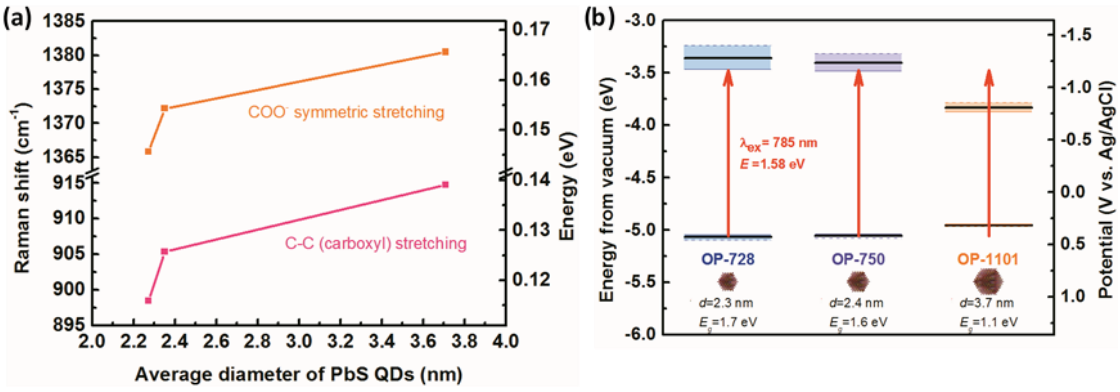

Figure 3.4. (a) Size-dependent blue-shifted vibrational modes of OA adjacent to PbS QDs: C-C (carboxyl) stretching (pink) and COO^- symmetric stretching (orange) as colored in Figure 3.3. (b) Size-dependent excitation of PbS QDs by the NIR laser of 785 nm considering the wide size distribution illustrated in colored regions (see the absorption spectrum in Figure 1 for details).

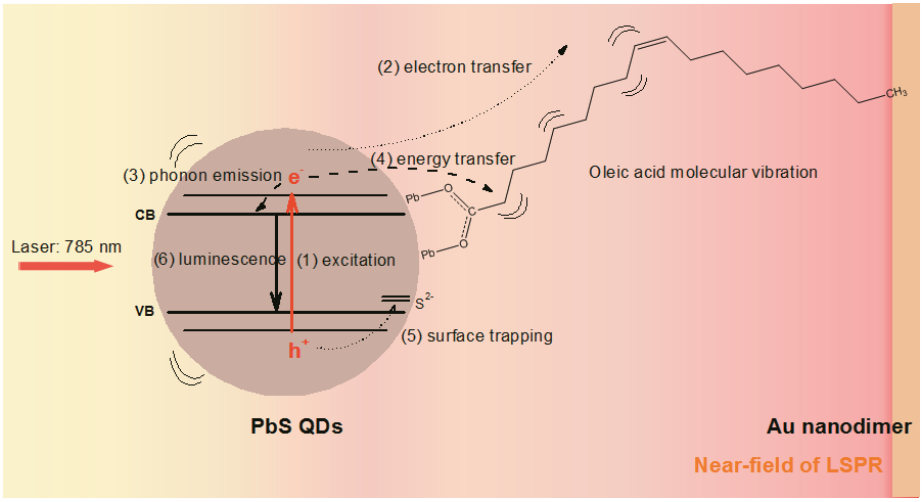

Figure 3.5. Scheme of possible processes of excited OA-capped PbS QDs/Au-NSL system by NIR of

785 nm including (1) excitation of PbS QDs with energy exceeding the bandgap (red solid line), (2) electron transfer from QD to Au through the molecule chain (dotted line), (3) intraband relaxation via phonon emission of the QD's lattice (dashed line), (4) intraband relaxation by energy transfer from QD to vibrations of OA ligand (dashed line), (5) hole transfer from QD to surface trapping state generated by dangling bond of S^{2-} ions (dotted line), (6) interband relaxation by radiative photoluminescence. Colored background roughly presents that the electromagnetic field generated by localized surface plasmon resonance can be enhanced in the confined region between PbS QD and Au nanostructure.

3.3.2.3 Size-Dependent LO Phonon Mode of PbS QDs

The phonon modes consists of the lattice vibrations in QDs was also observed for OP-1101 and OP-728 on Au-NSL substrate (Figure 5a), Raman band around 220 cm^{-1} was assigned as longitudinal optical phonon mode at Γ point of Brillouin zone (LO_{Γ}). Blue-shifted and narrowed FWHM of LO_{Γ} (Figure 3.6b) as decreasing the diameter of PbS QDs is ascribed to the relaxation of q=0 selection rule by quantum confinement effect[74] according to phonon dispersion wave of PbS neutron scattering[75] and is in agreement with the publication.[76, 77] Such successful phonon mode observation for ultra-small QDs with fairly few lattice number evidenced the effectiveness of electromagnetic field generated by PbS QDs-Au NDs system.

Furthermore, inhibition of phonon-assisted intraband relaxation has been expected because of the sparse electronic states known as the phonon bottleneck,[78] but controversially, fast electron-phonon relaxation was also simulated as fast as several picoseconds,[79] and detected for PbS QDs for 2~25 ps.[16, 17] Perfect symmetry breaking and generation of dense electronic state stemming from surface reconstruction by ligands,[80] Stark effect from fluctuating local electric fields,[47] breaking of the inversion-symmetry of wave functions,[81] or coupling with highly confined LSPR field,[82, 83] may account for the fastened phonon-assisted intraband relaxation, which followed by energy transfer from QDs to organic ligand for 1~100 ns[84-86] and photoluminescence around several μs for ultra-small PbS QDs[87, 88] (process 3, 4 and 6 in Figure 3.5).

As hot electrons and holes may perform opposite size-contributed relaxation pathway according to theoretical calculation,[20, 89] in the present study, the lack of observation on lattice vibration for OP-750 which produced the most modes-enhanced vibrational spectrum of OA may be accounted from competition between phonon scattering and energy transfer processes both serving as interband relaxation (process 3 and 4 in Figure 3.5), in which the latter is facilitated by large extent of hybridization between electronic states of OP-750 and OA molecule by highly coupled to LSPR in the regime of strong coupling thanks to their closest excitation energy.[90] Further investigation based on theoretical simulation and transient dynamics in electromagnetic field could provide additional information on thoroughly comprehending diverse energy losing pathways of hot carriers and give insight into development of multiple exciton generation by IV-VI semiconductor QDs.

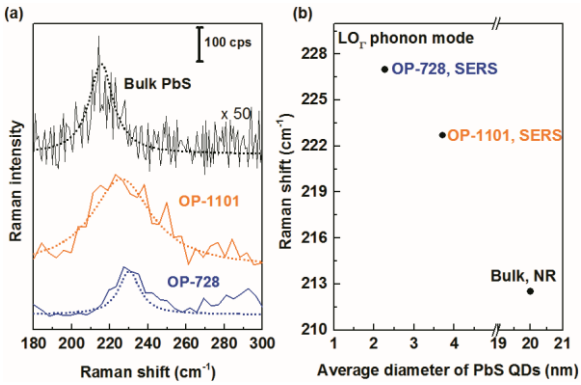

Figure 3.6. (a) SERS spectrum of longitudinal optical mode at Γ point of Brillouin zone (LOΓ) for OP-728 (blue) and OP-1101 (orange) on Au-NSL substrate and bulk galena powder (blue). Dotted lines are Lorenz fitting at the band maximum. (b) Size-dependent blue-shifted LOΓ phonon mode. Galena powder was exposed 1s and accumulated for 100 times by 5 mW NIR laser by an upright microscope.55 Laser intensity was normalized to 0.5 mW for all the measurements.

3.3.3 Potential-dependent Raman intensity

Electrochemical measurements advance the SERS spectrum compared with SERRS of OA molecule measured in the air (Figure 3.3, black) because of the reduction of the intense fluorescence background in electrolyte. Further examination was performed by applying different polarized potential for the OP-750/Au-NSL system as OP-750 present a most meticulous SERS spectrum.

EC-SERS of OA-capped PbS QDs absorbed on Au dimer was performed with negatively polarized potential decreased from 0 to -0.4 V (Figure 3.7a). Especially under potential of -0.2 V, Raman shift

of OA molecule presented distinct spectrum. Potential-dependent enhancement and reduction of certain vibration modes were observed and marked in orange and purple areas, respectively. As potential altered negatively, in contrast with the almost constant Raman intensity of the C-C anti-symmetric stretching around 1062 cm^{-1} (Figure 3.7a grey area and 4b black square-symbol-line), the CH_3-side (separated by the Olefin group) around 1115 cm^{-1} decreased (Figure 3.7b, purple circle-symbol-line) while CH_2 twisting around 1292 cm^{-1} (Figure 3.7b, orange diamond-symbol-line) increased apparently.

As has mentioned above, the Raman shift difference between the anti- and symmetric stretching, Δ, almost kept in the range of 140~190 cm^{-1} as the potential negatively polarized from 0 V to -0.4 V, indicating that the major binding mode between carboxylate head and Pb atoms is bridging bidentate with a minor partial of monodentate (Δ of 200~320 cm^{-1}).

Table 3.2. Raman-shift and modes assignments of oleic acid

Raman shift (cm^{-1})					Assignments	
OA/Au-NSL	PbS/Au-NSL					
0 V	-0 V	-0.2 V	-0.3 V	-0.4 V		
557, 578	568	583			C=C-C bending	Olefin group
	698	691			C=C-H out-of plane bending	
964		974			C=C-H out-of plane bending	
1266	1253	1266	1260		C=C-H in-plane bending	
846	860	815, 867	808	829	CH_3 rocking, chain-end tg, gg, gt	Polymethylene chains
	1065	1062	1065		C-C anti-symmetric stretching	
1101	1122	1115	1129		C-C stretching, CH_3-sided chain disordered	
1174	1185	1194		1195	CH_2 rocking	
1302		1292	1295	1292	CH_2 twisting	
1454		1438			CH_2 scissoring	
	895	898			C-C (carboxyl) stretching	Carboxyl group
1356, 1388	1331	1353	1343	1359	COO^- symmetric stretching	
1529	1510, 1562	1504, 1526	1526, 1563	1519	COO^- anti-symmetric stretching	
	179, 231	151, 173	183, 220	160	difference between anti- and symmetric stretching of COO^-	

The reason maybe come from the configuration of the OA-capped PbS QDs/Au-NSL system (Figure 3.7b, inset). As OA molecule serves as the surface modification of PbS QDs, the carboxyl covalently bond the surface-active Pb atom, leaving the methyl end to physically absorbed on the surface of Au. As the potential was polarized negatively, the accumulated electrons repulsed the electron cloud of methyl end toward the carbon chain of OA and compressed the OA molecules

between PbS QDs and Au nanodimer because of the less quality of molecule compared with PbS QDs. The deviation of electron cloud induced lengthening the C-C bond separated by the Olefin group at the CH_3-side, thus reduced the stretching strength and red-shifted this bond towards low energy (Table). Also such spatial compression did put disadvantage to the stretching and reduced Raman intensity apparently (Figure 3.7b, purple circle-symbol-line). On the other hand, such spatial alternation of OA molecule promoted vibrations sensitive to carbon skeleton concluding both the Olefin group such as C=C-C bending at 583 cm^{-1}, as well as the polymethylene chain, such as blue-shifted CH_2 rocking (chain-end) at 867 cm^{-1}, CH_2 rocking at 1194 cm^{-1}, CH_2 twisting at 1292 cm^{-1} and C-C (carboxyl) stretching at 898 cm^{-1} (marked as orange areas) at -0.2 V (see Table for details) because of the altered polarization of the ligand atoms.

Another reason for such variations can be explained by considering the strong coupling of the PbS QDs-Au nanodimer system. As the potential was altered from 0 to -0.2 V, some number of electrons were added to Au-NSL and can produce a shift in surface plasmon band position towards higher energy.[91, 92] Consequently, the overlap between the bandgap energy of PbS QDs (1^{st} exciton wavelength of 750 nm) and the surface plasmon can be enriched and reasonably the coupling degree of the present system will be improved. In this sense, modification of spectrum consisting of enhanced and red-shifted bands was observed for major vibrations.

When the potential was switched to a more negative potential (-0.3 and -0.4 V, Figure 3.7a, green and blue), due to the loose binding with Au, the desorption of the surface bound anions led to a decrease of Raman spectrum.

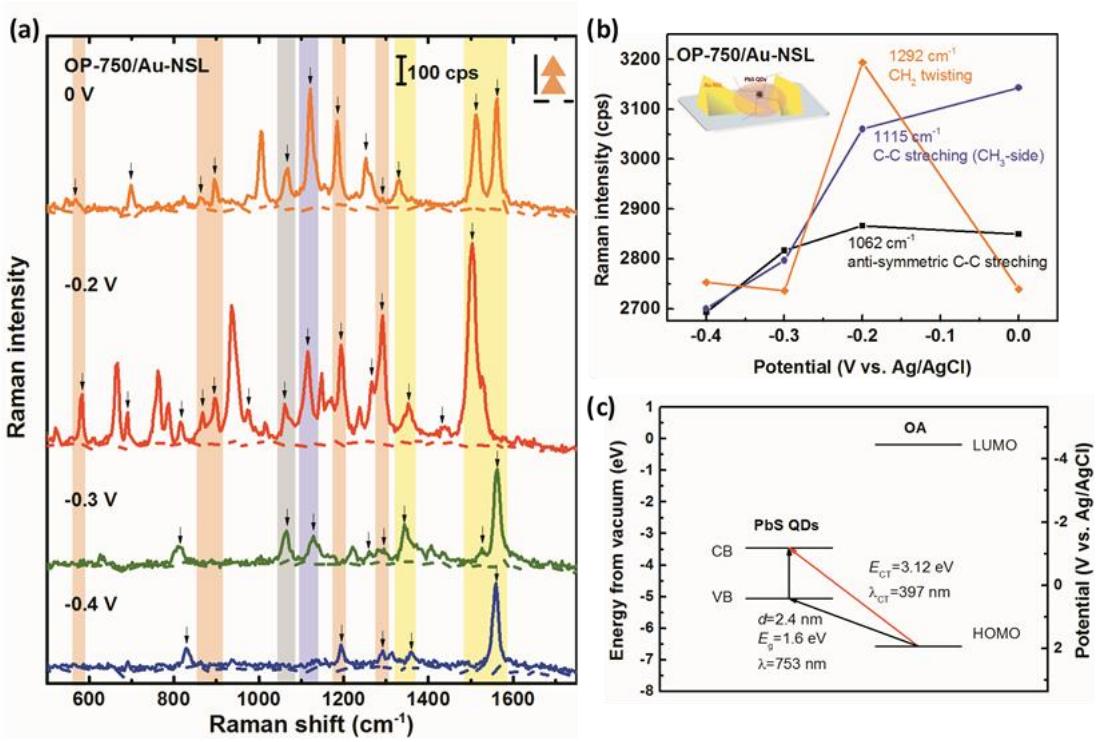

Figure 3.7. (a) EC-SERS spectrum of OA as capping ligands surrounding OP-750 QDs on Au-NSL substrate under negatively scanned potential of 0 (orange), -0.2 (red), -0.3 (green) and -0.4 V (blue). Signals were recorded and irradiated for 1 s by a laser of 785 nm in electrolyte of 0.1 M NaOH. Laser intensity was normalized to 0.6 mW both for parallel (solid line) and perpendicular (dotted line) polarization. Decreased and blue-shifted, increased and red-shifted, and almost constantly remained vibration modes are marked as purple, orange and grey, respectively. (b) Potential-dependent Raman intensity at 1115, 1292 and 1062 cm^{-1} as marked in purple, orange and grey areas in (a). Inset is the schematic view of OA-capped PbS QDs/Au-NSL system. (c) Energy level diagram for OA-capped PbS QDs system. Energy of charge transfer from the HOMO of OA to CB of PbS QDs is 3.12 eV.

3.3.4 FDTD simulation of PbS QDs coupled Au NP system

The enhancement mechanism of the PbS/Au system was examined. First, charge transfer effect between PbS QDs and capping ligands of OA was considered according to the size-dependent band energy of PbS QDs. The HOMO and LUMO energy levels of OA was obtained by density functional theory with B3LYP exchange–correlation functional, according to a publication.[93] As shown in Figure 3.7c, the proposed minimum charge transfer energy from the HOMO of OA molecule to CB of QDs and to Au surface at potential of -0.2 V are respectively 3.12 eV and 2.13 eV, sufficiently larger than the current excitation energy of 1.58 eV (785 nm), suggesting the enhancement of Raman spectra was not stemmed from charge transfer mechanism.

In order to examine the electromagnetic enhancement, we utilized Finite-Difference Time-Domain method (FDTD) to simulate the electric field distribution of the PbS QD-Au NP hetero-system, simply assuming the size of PbS QDs to be 1.6 nm with a distance of 0.6 nm separated both from Au NP and from other close-packed PbS QDs in vacuum. The electric field generated by Au NP was confined within the gap between the Au NP and the near-by PbS QD, because of the unique dielectric and metallic property of PbS.[49] The wavelength-dependent electric field in the center line within the gap gives maximum value at 520-530 nm, which is comparable to the extinction spectrum of Au nanoparticle.[32] Stronger electric field at slightly shorter wavelength was generated by a single PbS QD in comparison with the close-packed numerous PbS QDs system (Figure 3.8g). The results indicate that the dielectric and metallic property of PbS QD combined to Au nanoparticle undoubtedly enhance the near-field generated by localized surface plasmon resonance. As the coupling number of PbS QDs increases, although the enhancement at the center spot decreases due to possible reduced scattering efficiency, the overall enhanced area is multiplied and thus can boost the enhancement between QDs and Au nanoparticle. The theoretical calculation demonstrates the availability of the remarkable SERS scattering of OA molecule surrounding PbS QDs by well coupling with Au NP.

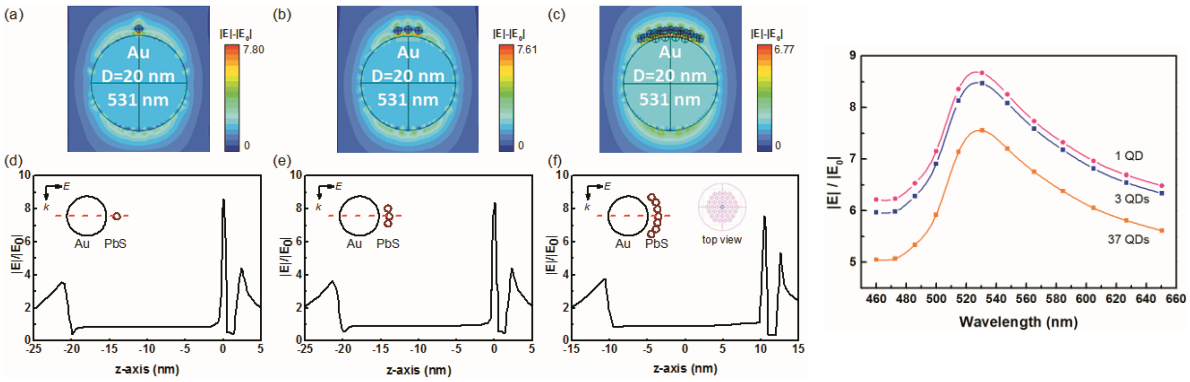

Figure 3.8. Results of FDTD simulation for Au-PbS hetero-system. (Left) Upper row: electric-field distribution excluding the incident field; lower row: the corresponding spatial electric-field distributions along the center line connecting Au and PbS (red dashed line). System of Au (D=20 nm) and PbS QD (d=1.6 nm) separated with 0.6 nm at the gap at the wavelength of 531 nm: (a, d) 1 QD, (b, e) 3 QDs, and (c, f) [37] QDs in a close-packed single layer. Inset: schematic illustration of the system and top view of the numerous QDs (f). The 0 point along z-axis was set as the center between Au and PbS. (Right) Wavelength-dependent maximum value of the electric field between the gap along the center line of the Au-PbS hetero-system. (a) and (c) are reproduced from J. Phys. Chem. C 2015, 119 (38), 22092 (ref32). Copyright 2015 American Chemical Society.

3.4 Conclusions

Experimental SERS studies of oleic acid as capping ligand of PbS QDs on Au nanodimer arrays have shown that the modification in the vibrational spectrum extremely depends on the QDs' size. The binding mode between oxygen atom of carboxylate head and Pb atoms was determined as bridging bidentate for all PbS QDs varied in size according to anti- and symmetric stretching of COO^-. Investigations of blue-shifted vibrational modes nearby QD's surface is attributed to inductive effect by size-dependent excitation involving the surface trapping of hole in the enhanced electromagnetic field created by coupling PbS QDs with localized surface plasmon resonance. Lattice vibration of PbS QDs assigned as confined LO phonon mode presents size-dependent shift and FWHM because of relaxation of q=0 selection rule by phonon confinement. Best coupling between OP-750 and Au nanodimers brings out the most meticulous spectrum of capping ligands whereas lacks in phonon emission, indicating the hybridization between electronic states of a coupled system affects the selection for a most preferred interband relaxation way including scattering phonon and energy transfer to surfactants. Potential-dependent variations of vibrational modes were investigated and explained by considering the electron transfer and static Coulomb interaction between OA molecule and Au surface. The FDTD simulation indicates electromagnetic mechanism plays significant role in the enhancement. The present observation proves apparently that the PbS QDs can be efficiently excited by localized surface plasmon resonance of Au nanostructure via effective band excitation of electrons in the PbS QDs. The control of electrochemical potential is the way to control the interaction between the PbS QDs and Au.

References

1. Maikov, G. I.; Vaxenburg, R.; Sashchiuk, A.; Lifshitz, E. *ACS Nano* **2010,** 4, (11), 6547-6556.
2. Sowers, K. L.; Swartz, B.; Krauss, T. D. *Chemistry of Materials* **2013,** 25, (8), 1351-1362.
3. Zhuang, Z.; Peng, Q.; Li, Y. *Chemical Society Reviews* **2011,** 40, (11), 5492-5513.
4. Nair, G.; Zhao, J.; Bawendi, M. G. *Nano Letters* **2011,** 11, (3), 1136-1140.
5. Bischof, T. S.; Correa, R. E.; Rosenberg, D.; Dauler, E. A.; Bawendi, M. G. *Nano Letters* **2014,** 14, (12), 6787-6791.
6. Krauss, T. D.; Peterson, J. J. *The Journal of Physical Chemistry Letters* **2010,** 1, (9), 1377-1382.

7. Durisic, N.; Wiseman, P. W.; Grütter, P.; Heyes, C. D. *ACS Nano* **2009,** 3, (5), 1167-1175.
8. Hoyer, P.; Staudt, T.; Engelhardt, J.; Hell, S. W. *Nano Letters* **2011,** 11, (1), 245-250.
9. Gdor, I.; Shapiro, A.; Yang, C.; Yanover, D.; Lifshitz, E.; Ruhman, S. *ACS Nano* **2015,** 9, (2), 2138-2147.
10. Klimov, V. I.; Mikhailovsky, A. A.; McBranch, D. W.; Leatherdale, C. A.; Bawendi, M. G. *Science* **2000,** 287, (5455), 1011-1013.
11. Geiregat, P.; Houtepen, A.; Justo, Y.; Grozema, F. C.; Van Thourhout, D.; Hens, Z. *The Journal of Physical Chemistry C* **2014,** 118, (38), 22284-22290.
12. Rabouw, F. T.; Vaxenburg, R.; Bakulin, A. A.; van Dijk-Moes, R. J. A.; Bakker, H. J.; Rodina, A.; Lifshitz, E.; L. Efros, A.; Koenderink, A. F.; Vanmaekelbergh, D. *ACS Nano* **2015,** 9, (10), 10366-10376.
13. Schaller, R. D.; Klimov, V. I. *Physical Review Letters* **2004,** 92, (18), 186601.
14. Padilha, L. A.; Stewart, J. T.; Sandberg, R. L.; Bae, W. K.; Koh, W.-K.; Pietryga, J. M.; Klimov, V. I. *Accounts of Chemical Research* **2013,** 46, (6), 1261-1269.
15. Stewart, J. T.; Padilha, L. A.; Qazilbash, M. M.; Pietryga, J. M.; Midgett, A. G.; Luther, J. M.; Beard, M. C.; Nozik, A. J.; Klimov, V. I. *Nano Letters* **2012,** 12, (2), 622-628.
16. Midgett, A. G.; Luther, J. M.; Stewart, J. T.; Smith, D. K.; Padilha, L. A.; Klimov, V. I.; Nozik, A. J.; Beard, M. C. *Nano Letters* **2013,** 13, (7), 3078-3085.
17. Nootz, G.; Padilha, L. A.; Levina, L.; Sukhovatkin, V.; Webster, S.; Brzozowski, L.; Sargent, E. H.; Hagan, D. J.; Van Stryland, E. W. *Physical Review B* **2011,** 83, (15), 155302.
18. Cirloganu, C. M.; Padilha, L. A.; Lin, Q.; Makarov, N. S.; Velizhanin, K. A.; Luo, H.; Robel, I.; Pietryga, J. M.; Klimov, V. I. *Nat Commun* **2014,** 5.
19. El-Ballouli, A. a. O.; Alarousu, E.; Usman, A.; Pan, J.; Bakr, O. M.; Mohammed, O. F. *ACS Photonics* **2014,** 1, (3), 285-292.
20. Kambhampati, P. *The Journal of Physical Chemistry C* **2011,** 115, (45), 22089-22109.
21. Geiregat, P.; Delerue, C.; Justo, Y.; Aerts, M.; Spoor, F.; Van Thourhout, D.; Siebbeles, L. D. A.; Allan, G.; Houtepen, A. J.; Hens, Z. *ACS Nano* **2015,** 9, (1), 778-788.
22. Morris-Cohen, A. J.; Malicki, M.; Peterson, M. D.; Slavin, J. W. J.; Weiss, E. A. *Chemistry of Materials* **2013,** 25, (8), 1155-1165.
23. Brown, P. R.; Kim, D.; Lunt, R. R.; Zhao, N.; Bawendi, M. G.; Grossman, J. C.; Bulović, V. *ACS Nano* **2014,** 8, (6), 5863-5872.
24. Bloom, B. P.; Zhao, L.-B.; Wang, Y.; Waldeck, D. H.; Liu, R.; Zhang, P.; Beratan, D. N. *The Journal of Physical Chemistry C* **2013,** 117, (43), 22401-22411.
25. Knowles, K. E.; Peterson, M. D.; McPhail, M. R.; Weiss, E. A. *The Journal of Physical Chemistry C* **2013,** 117, (20), 10229-10243.
26. Choi, J. J.; Luria, J.; Hyun, B.-R.; Bartnik, A. C.; Sun, L.; Lim, Y.-F.; Marohn, J. A.; Wise, F. W.; Hanrath, T. *Nano Letters* **2010,** 10, (5), 1805-1811.
27. Akselrod, G. M.; Prins, F.; Poulikakos, L. V.; Lee, E. M. Y.; Weidman, M. C.; Mork, A. J.; Willard, A. P.; Bulović, V.; Tisdale, W. A. *Nano Letters* **2014,** 14, (6), 3556-3562.
28. Omogo, B.; Aldana, J. F.; Heyes, C. D. *The Journal of Physical Chemistry C* **2013,** 117, (5), 2317-2327.
29. Baker, D. R.; Kamat, P. V. *Langmuir* **2010,** 26, (13), 11272-11276.
30. Turk, M. E.; Vora, P. M.; Fafarman, A. T.; Diroll, B. T.; Murray, C. B.; Kagan, C. R.; Kikkawa, J. M. *ACS Nano* **2015,** 9, (2), 1440-1447.
31. Schnitzenbaumer, K. J.; Labrador, T.; Dukovic, G. *The Journal of Physical Chemistry C* **2015,** 119, (23), 13314-

13324.

32. Li, X.; Suzuki, K.; Toda, T.; Yasuda, S.; Murakoshi, K. *The Journal of Physical Chemistry C* **2015,** 119, (38), 22092-22101.
33. Hines, D. A.; Kamat, P. V. *The Journal of Physical Chemistry C* **2013,** 117, (27), 14418-14426.
34. Ji, X.; Copenhaver, D.; Sichmeller, C.; Peng, X. *Journal of the American Chemical Society* **2008,** 130, (17), 5726-5735.
35. André, A.; Zherebetskyy, D.; Hanifi, D.; He, B.; Samadi Khoshkhoo, M.; Jankowski, M.; Chassé, T.; Wang, L.-W.; Schreiber, F.; Salleo, A.; Liu, Y.; Scheele, M. *Chemistry of Materials* **2015,** 27, (23), 8105-8115.
36. Balazs, D. M.; Dirin, D. N.; Fang, H.-H.; Protesescu, L.; ten Brink, G. H.; Kooi, B. J.; Kovalenko, M. V.; Loi, M. A. *ACS Nano* **2015,** 9, (12), 11951-11959.
37. Ko, D.-K.; Maurano, A.; Suh, S. K.; Kim, D.; Hwang, G. W.; Grossman, J. C.; Bulović, V.; Bawendi, M. G. *ACS Nano* **2016,** 10, (3), 3382-3388.
38. Zhang, J.; Crisp, R. W.; Gao, J.; Kroupa, D. M.; Beard, M. C.; Luther, J. M. *The Journal of Physical Chemistry Letters* **2015,** 6, (10), 1830-1833.
39. Zhang, H.; Yang, J.; Chen, J.-R.; Engstrom, J. R.; Hanrath, T.; Wise, F. W. *The Journal of Physical Chemistry Letters* **2016,** 7, (4), 642-646.
40. Lifshitz, E. *The Journal of Physical Chemistry Letters* **2015,** 6, (21), 4336-4347.
41. George C. Schatz, M. A. Y., Richard P. Van Duyne, Electromagnetic Mechanism of SERS. In *Surface-Enhanced Raman Scattering: Physics and Applications*, K. Kneipp; M. Moskovits; H. Kneipp, Eds. Springer-Verlag Berlin Heidelberg: New York, **2006**; pp 19-45.
42. Ronald L. Birke, J. R. L., Surface-Enhanced Raman Scattering. In *Spectroelectrochemistry: Theory and Practice*, R.J. Gale, Ed. Springer US: Plenum Press, New York, **1998**; pp 263-348.
43. Lombardi, J. R.; Birke, R. L. *Accounts of Chemical Research* **2009,** 42, (6), 734-742.
44. Livingstone, R.; Zhou, X.; Tamargo, M. C.; Lombardi, J. R.; Quagliano, L. G.; Jean-Mary, F. *The Journal of Physical Chemistry C* **2010,** 114, (41), 17460-17464.
45. Li, W.; Zamani, R.; Rivera Gil, P.; Pelaz, B.; Ibáñez, M.; Cadavid, D.; Shavel, A.; Alvarez-Puebla, R. A.; Parak, W. J.; Arbiol, J.; Cabot, A. *Journal of the American Chemical Society* **2013,** 135, (19), 7098-7101.
46. Cong, S.; Yuan, Y.; Chen, Z.; Hou, J.; Yang, M.; Su, Y.; Zhang, Y.; Li, L.; Li, Q.; Geng, F.; Zhao, Z. *Nat Commun* **2015,** 6.
47. Trinh, M. T.; Sfeir, M. Y.; Choi, J. J.; Owen, J. S.; Zhu, X. *Nano Letters* **2013,** 13, (12), 6091-6097.
48. Berger, L. I., Chapter 12. Properties of Solids. In *CRC Handbook of Chemistry and Physics*, 90th ed.; W.M. Haynes, Ed. CRC Press: Boca Raton, FL, **2005**; pp 1-218.
49. Hutter, T.; Mahajan, S.; Elliott, S. R. *Journal of Raman Spectroscopy* **2013,** 44, (9), 1292-1298.
50. Fu, X.; Pan, Y.; Wang, X.; Lombardi, J. R. *The Journal of Chemical Physics* **2011,** 134, (2), 024707.
51. Wu, D.-Y.; Li, J.-F.; Ren, B.; Tian, Z.-Q. *Chemical Society Reviews* **2008,** 37, (5), 1025-1041.
52. Akhtar, J.; Azad Malik, M.; O'Brien, P.; Wijayantha, K. G. U.; Dharmadasa, R.; Hardman, S. J. O.; Graham, D. M.; Spencer, B. F.; Stubbs, S. K.; Flavell, W. R.; Binks, D. J.; Sirotti, F.; El Kazzi, M.; Silly, M. *Journal of Materials Chemistry* **2010,** 20, (12), 2336-2344.
53. Kobayashi, M.; Kaneko, F.; Sato, K.; Suzuki, M. *The Journal of Physical Chemistry* **1986,** 90, (23), 6371-6378.
54. Tandon, P.; Förster, G.; Neubert, R.; Wartewig, S. *Journal of Molecular Structure* **2000,** 524, (1–3), 201-215.
55. Nagasawa, F.; Takase, M.; Murakoshi, K. *The Journal of Physical Chemistry Letters* **2014,** 5, (1), 14-19.
56. Sawai, Y.; Takimoto, B.; Nabika, H.; Ajito, K.; Murakoshi, K. *Journal of the American Chemical Society* **2007,**

129, (6), 1658-1662.
57. Sawai, Y.; Takimoto, B.; Nabika, H.; Ajito, K.; Murakoshi, K. *Faraday Discussions* **2006,** 132, (0), 179-190.
58. Johnson, P. B.; Christy, R. W. *Physical Review B* **1972,** 6, (12), 4370-4379.
59. Palik, E. D., *Handbook of Optical Constants of Solids*. Academic Press: New York, **2011**; p 187-227.
60. Haynes, C. L.; McFarland, A. D.; Smith, M. T.; Hulteen, J. C.; Van Duyne, R. P. *The Journal of Physical Chemistry B* **2002,** 106, (8), 1898-1902.
61. Adar, F. *Spectroscopy* **2013,** 28, (6).
62. Baas, J. M. A., *A Guide to the Complete Interpretation of Infrared Spectra of Organic Structures*. N.P.G. Roeges. John Wiley: **1995**; Vol. 114, p 114-114.
63. Colthup, N. B.; Daly, L. H.; Wiberley, S. E., Chapter 9 - Carbonyl Compounds. In *Introduction to Infrared and Raman Spectroscopy*, 3rd ed.; Academic Press: San Diego, **1990**; pp 289-325.
64. Nakamoto, K., Theory of Normal Vibrations. In *Infrared and Raman Spectra of Inorganic and Coordination Compounds*, John Wiley & Sons, Inc.: **2008**; pp 1-147.
65. Wu, N.; Fu, L.; Su, M.; Aslam, M.; Wong, K. C.; Dravid, V. P. *Nano Letters* **2004,** 4, (2), 383-386.
66. Ren, Y.; Iimura, K.-i.; Kato, T. *Langmuir* **2001,** 17, (9), 2688-2693.
67. Cass, L. C.; Malicki, M.; Weiss, E. A. *Analytical Chemistry* **2013,** 85, (14), 6974-6979.
68. Han, S. W.; Joo, S. W.; Ha, T. H.; Kim, Y.; Kim, K. *The Journal of Physical Chemistry B* **2000,** 104, (50), 11987-11995.
69. SOCIETY, C., (9Z)-9-octadecenoic acid (Oleic Acid). **1976**.
70. Abuelela, A. M.; Mohamed, T. A.; Prezhdo, O. V. *The Journal of Physical Chemistry C* **2012,** 116, (27), 14674-14681.
71. Jasieniak, J.; Califano, M.; Watkins, S. E. *ACS Nano* **2011,** 5, (7), 5888-5902.
72. Kobayashi, T.; Du, J., Femtosecond Real-Time Vibrational Spectroscopy using Ultrafast Laser Pulses. In *Ultrafast Dynamics in Molecules, Nanostructures and Interfaces*, World Scientific: **2014**; pp 1-28.
73. Yang, Y.; Rodríguez-Córdoba, W.; Xiang, X.; Lian, T. *Nano Letters* **2012,** 12, (1), 303-309.
74. Smith, G. D.; Firth, S.; Clark, R. J. H.; Cardona, M. *Journal of Applied Physics* **2002,** 92, (8), 4375-4380.
75. Elcombe, M. M. *Proceedings of the Royal Society of London A: Mathematical, Physical and Engineering Sciences* **1967,** 300, (1461), 210-217.
76. Nanda, K. K.; Sahu, S. N.; Soni, R. K.; Tripathy, S. *Physical Review B* **1998,** 58, (23), 15405-15407.
77. Kilian, O.; Allan, G.; Wirtz, L. *Physical Review B* **2009,** 80, (24), 245208.
78. Guyot-Sionnest, P.; Wehrenberg, B.; Yu, D. *The Journal of Chemical Physics* **2005,** 123, (7), 074709.
79. Kilina, S. V.; Kilin, D. S.; Prezhdo, O. V. *ACS Nano* **2009,** 3, (1), 93-99.
80. Liu, J.; Kilina, S. V.; Tretiak, S.; Prezhdo, O. V. *ACS Nano* **2015,** 9, (9), 9106-9116.
81. Nootz, G.; Padilha, L. A.; Olszak, P. D.; Webster, S.; Hagan, D. J.; Van Stryland, E. W.; Levina, L.; Sukhovatkin, V.; Brzozowski, L.; Sargent, E. H. *Nano Letters* **2010,** 10, (9), 3577-3582.
82. Jain, P. K.; Ghosh, D.; Baer, R.; Rabani, E.; Alivisatos, A. P. *Proceedings of the National Academy of Sciences* **2012,** 109, (21), 8016-8019.
83. Takase, M.; Ajiki, H.; Mizumoto, Y.; Komeda, K.; Nara, M.; Nabika, H.; Yasuda, S.; Ishihara, H.; Murakoshi, K. *Nat Photon* **2013,** 7, (7), 550-554.
84. Piland, G. B.; Huang, Z.; Lee Tang, M.; Bardeen, C. J. *The Journal of Physical Chemistry C* **2016,** 120, (11), 5883-5889.
85. Peterson, M. D.; Cass, L. C.; Harris, R. D.; Edme, K.; Sung, K.; Weiss, E. A. *Annual Review of Physical Chemistry*

2014, 65, (1), 317-339.

86. Pandey, A.; Guyot-Sionnest, P. *Science* **2008,** 322, (5903), 929-932.
87. Moreels, I.; Lambert, K.; Smeets, D.; De Muynck, D.; Nollet, T.; Martins, J. C.; Vanhaecke, F.; Vantomme, A.; Delerue, C.; Allan, G.; Hens, Z. *ACS Nano* **2009,** 3, (10), 3023-3030.
88. Ushakova, E. V.; Litvin, A. P.; Parfenov, P. S.; Fedorov, A. V.; Artemyev, M.; Prudnikau, A. V.; Rukhlenko, I. D.; Baranov, A. V. *ACS Nano* **2012,** 6, (10), 8913-8921.
89. Cooney, R. R.; Sewall, S. L.; Anderson, K. E. H.; Dias, E. A.; Kambhampati, P. *Physical Review Letters* **2007,** 98, (17), 177403.
90. Gibbs, H. M.; Khitrova, G.; Koch, S. W. *Nat Photon* **2011,** 5, (5), 273-273.
91. Templeton, A. C.; Pietron, J. J.; Murray, R. W.; Mulvaney, P. *The Journal of Physical Chemistry B* **2000,** 104, (3), 564-570.
92. Zhang, X.; Chen, Y. L.; Liu, R.-S.; Tsai, D. P. *Reports on Progress in Physics* **2013,** 76, (4), 046401.
93. Ning, Z.; Molnar, M.; Chen, Y.; Friberg, P.; Gan, L.; Agren, H.; Fu, Y. *Physical Chemistry Chemical Physics* **2011,** 13, (13), 5848-5854.

Chapter 4

Construction of Photocurrent Generation System using PbS Quantum Dots Coupled with Au Nanostructures on TiO_2 Electrode

4.1 Introduction

Benefiting from relatively larger Bohr radius of 18 nm, lead sulfide (PbS) is capable to exhibit strong quantum confinement effect. PbS QDs-sensitized photoelectrochemical cells based on titanium dioxides (TiO_2) have been confirmed to perform efficiently not only in photoenergy conversion[1, 2] but also in photodegradation or photocatalytic reduction of molecules[3, 4] by various synthesis approaches.[5-9] Surface plasmon resonance is a robust approach in advancing the applications of PbS QDs-based photoenergy conversion owing to enhanced electromagnetic field by coupling dielectric PbS with noble metal nanostructures.[10-12]

As the concept for the further improvement of photoenergy conversions, the use of multiple exciton generation (carrier multiplication) has been proposed. A high energy photon can excite more than two pairs of electrons or holes in semiconductor and credibly exceed the Shockley-Queisser limit of ~33% by traditional photoenergy devices,[13-16] has boosted intense studies focused on intrinsic properties of colloid PbS QDs including inter- or intraband relaxation processes of fluorescence blinking,[17, 18] Auger recombination,[19-22] phonon-assisted intraband relaxations[23, 24] based on determination of various processes' lifetime. However, compared to electron transfer[25-28] or electron/hole trapping by surface state,[29-31] research on hole transfer between QDs and inorganic electrolyte has been merely studied.

Instead of triiodide/iodide (I^{3-}/ I^-) electrolytes, sulfide redox couple (S^{2-}/S_n^{2-}) for hole scavenging plays a crucial role in stabling lead chalcogenide-based QDs-sensitized photoelectrochemical cells (QDSC) from degradation. Dynamics of interfacial hole transfer process from QDSC to polysulfide has been discussed by transient absorption,[32] but best to our knowledge, potential-dependent relation between electron and hole separation remains blank. Infrared PbS QDs exhibiting MEG in visible light

region has been confirmed to benefit photo-electrochemical conversion thanks to the well coupling with plasmonic gold nanoparticles according to previous study by our group.[33] In this chapter, a coupling techniques by simultaneously electrochemical surface-enhanced Raman scattering and photoelectric response measurement was utilized to reveal electron-hole pair separation of infrared PbS QDs-sensitized TiO_2/Au/TiO_2 electrode in electrolyte containing sulfide redox couple (S^{2-}/S_n^{2-}). Raman intensity of polysulfur vibrations and collected photocurrent were observed increasing as potential polarized from negative to positive, because the improved charge separation efficiency at the PbS/TiO_2 interface under positive potential benefits electron injection from excited PbS QDs and subsequently facilitates hole transfer to S^{2-} donor. Fast enough hole transfer at a more positive potential from PbS QDs by S^{2-} than that of electron transfer is required for the effective charge separation to achieve overall high conversion efficiency even though multiple excitons are generated. The observation by coupling techniques provide insights in better understanding charge separation processes and designing QDs-sensitized photoelectrochemical cells based on MEG.

4.2 Experimental

4.2.1 Sensitization of PbS QDs

OA-capped PbS QDs was diluted in argon-degased dehydrated hexane. The above PbS QDs dispersion was drop-casted onto the surface of TiO_2/Au/TiO_2 substrate. It was spread into a circle of about 2 cm in diameter with a particle density of 2.3 x 10^{12} cm^{-2}. After solvent evaporation, Raman measurements were taken on these samples.

4.2.2 Simultaneous EC-SERS and photocurrent measurements

Raman measurements were performed via an inverted Raman spectroscopy of Nanofinder®30 (Tokyo Instruments, SOLAR TII) with a 100x objective lens (Nikon TU Plan ELWD, NA=0.80, WD=4.5 mm). Visible laser light of 514.8 nm (E_{ex} =2.4 eV) was obtained from an argon gas laser (Tokyo Keiki). The output laser intensity was tunable via a ND filter yielding an estimated spot size of irradiation, ~1 μm, and was measured via power meter (OPHIR Japan LTD.). Raman measurements were carried out

at the backscattering configuration collecting the scattering photons. The CCD (CS230B CCD color camera with OLM PUS SZ-CTV and CA180 camera adapter, Teli) equipped with a cooler (solver, scanning probe microscope) resolution of 514 nm is 6.2 cm^{-1}. The silicon line at 520.8 cm^{-1} was used for the calibration. All the measurements were performed under a constant temperature of 25 ^{o}C.

Electrochemical SERS measurement was performed via a three-electrode system in electrolyte of 0.05 M Na_2S and 0.1 M NaOH aqueous solution (pH=13). Hand-made Ag/AgCl (sal. KCl) and Pt narrow sheet were respectively used as the reference and counter electrodes. Polarized potential was well controlled from -1 V to +0.5 V with an interval of 0.1 V by a potentiostat (HSV-110, Hokuto Denko). The Fermi level of TiO_2 will be tuned as changing the polarized potential. Simultaneous Raman spectrum and photocurrent were measured under laser irradiation for 30 s by an intensity of 80 μW.

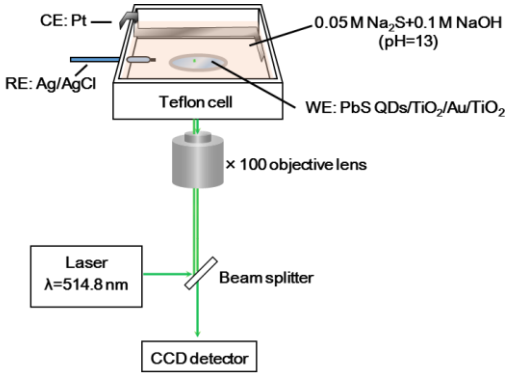

Figure 4.1. Schematic of the electrochemical SERS measurement

4.3 Results and discussion

4.3.1 Potential-dependent SERS spectrum and simultaneous photocurrent

EC-SERS spectrum of OP-1344/TiO_2/Au/TiO_2 electrode was measured under the potential altered from -1 V to +0.5 V (vs. Ag/AgCl) in an electrolyte of 0.05 M Na_2S+0.1 M NaOH aqueous solution (Figure 4.2a, red). As potential polarized from negative to positive, enhancement of vibrations at 155, 222 and 474 cm^{-1} was investigated and assigned as S-S-S bending and S-S stretching of the polysulfide di-anions S_n^{2-}.[34] Such vibration change is resulted from the potential-dependent chemical reaction of the donor of S^{2-} in the electrolyte oxidized into S_n^{2-} by the hole excited in PbS QDs,[10, 32] as illustrated

in Figure 4.2c. Control experiments of TiO_2/Au/TiO_2 and TiO_2 were also examined under the same conditions but the evolution of the band assigned to S_n^{2-} was not observed (see Figure A4.1).

Potential-dependent Raman intensity of S-S-S bending at 222 cm^{-1} and the simultaneous generated photocurrent were summarized for the three sorts of electrodes (Figure 4.2b). As the potential altered to positive direction, both Raman intensity of polysulfur vibrations as well as the photocurrent of OP-1344/TiO_2/Au/TiO_2 (red) were increased, because the Fermi level in TiO_2 moves downwards corresponding with a more positive potential (Figure 4.2c) and enlarges the potential gradient in TiO_2 which consequently benefits fast the electron injection into TiO_2 via the excitation of PbS QDs, leading to effective electron-hole separation to remain holes at the interface. As previously reported,[10, 33] the significant photocurrent is attributed to not only the enhanced electromagnetic field by coupling dielectric PbS QDs with localized surface plasmon, but also the contribution of multiple exciton generation. PbS QDs with relatively small band gap in near-infrared region, as OP-1344 used in the present study, excited by visible light with energy exceeding 2.6 times of the bandgap produce multiple exciton for the electron injection from the conduction band of PbS fairly approximates to that of anatase TiO_2 (Figure 4.2c). In addition, increase in the photocurrent saturated from -0.3 V, more negative than that in the polysulfur from +0.1 V (Figure 4.2b), credibly because of the different dynamics on time scale between electron and hole transfer. Electron transfer from PbS QDs into TiO_2 NPs has been estimated with a time scale of femtosecond,[35] tremendously more rapid than hole scavenging by donor of S^{2-} on a nanosecond scale[32] and radiative recombination detected as photoluminescence around 1 μs.[36] Such slow hole scavenging may limit electron-hole pair separation of QDs and obtainment overall high conversion efficiency even though multiple excitons are generated. Moreover, vibrational modes of OA, the surface modification of PbS QDs, unfortunately, was not detected due to not only the relatively lower excitation intensity with weak resonance but also the enlarged distance between PbS QDs and Au NPs by the 2nd layer of TiO_2 in comparison with a direct contact as descripted previously.

As for the control experiments, photocurrent measurements for both the bare TiO_2 and the plasmonic TiO_2/Au/TiO_2 electrodes were carried out (Figure 4.2b, blue and orange, respectively). The extremely limited photoelectric response of the bare TiO_2 electrode is attributed to the TiO_2 doped by S ions from

the electrolyte, showing the photocurrent response in visible light region due to the intermediate states in the bandgap of TiO_2. The response of the plasmonic TiO_2/Au/TiO_2 electrodes results from enhanced excitation of the intermediate states by LSPR. The LSPR field also facilitates the formation of a hot electron-hole pair: the electron is collected by TiO_2 and detected as photocurrent[10] whereas the hole oxides water[37, 38] rather than S^{2-} because of more positive potential of O_2/H_2O than S/S^{2-}. Supplemental examination was also performed by increasing excitation intensity (Figure A4.2), showing apparent Raman bands of S_n^{2-}, .but TiO_2 phonon modes assigned as anatase[39, 40] irradiated by a relatively high laser intensity of 1.61 mW. Such investigations confirms that the charge separation and transfer processes by PbS QDs dose benefit photoelectric conversion efficiency for solar cells. Further investigation based on potential-dependent relationship between photocurrent and photoluminescence in electromagnetic field could provide additional information on thoroughly comprehending charge transfer and radiative recombination processes under electrochemical environment and would considerably advance development on IV-VI semiconductor QDs-sensitized photoelectrochemical cell.

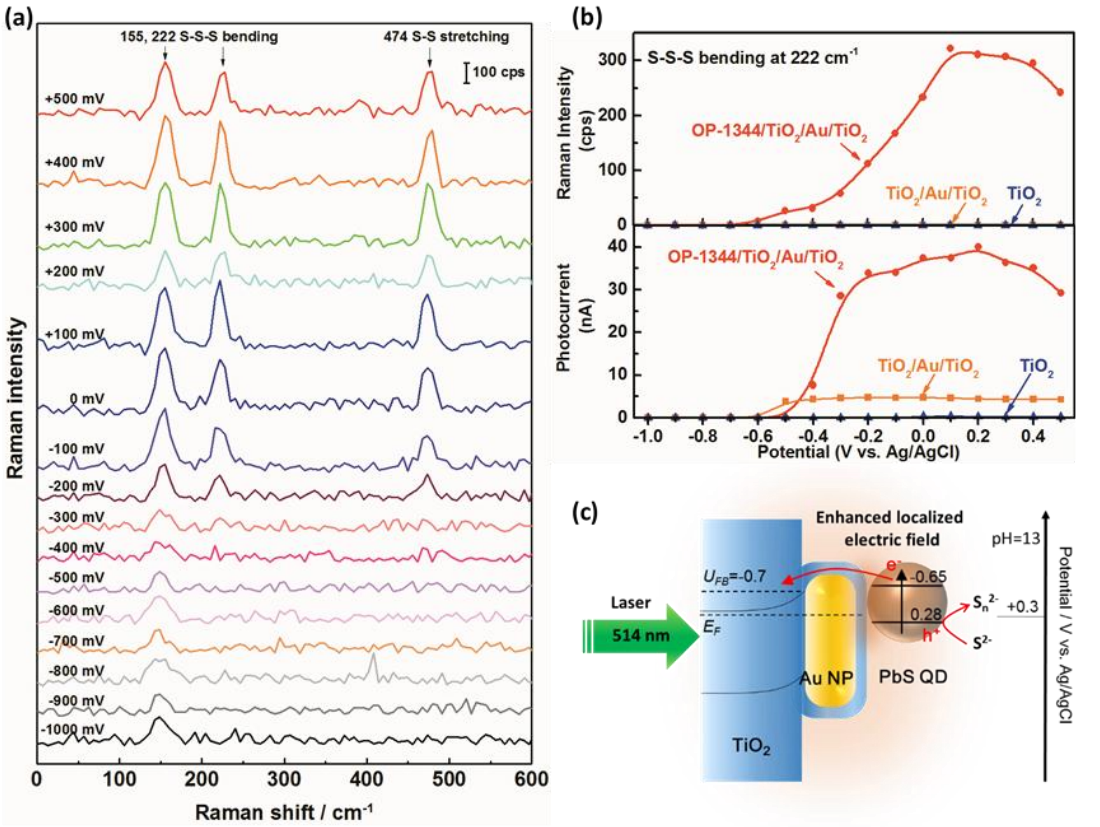

Figure 4.2. (a) EC-SERS spectrum of OP-1344/TiO_2/Au/TiO_2 scanned potential from -1 V to +0.5 V

(vs. Ag/AgCl) in electrolyte of 0.05 M Na_2S+0.1 M NaOH aqueous solution. Raman spectrum and corresponding photocurrent signals were recorded simultaneously and irradiated for 30 s by a laser of 514.8 nm with the intensity of 0.08 mW. (b) Potential-dependent Raman intensity of S-S-S bending band at 222 cm^{-1} (top) and the coincident photocurrent (bottom) of OP-1344/TiO_2/Au/TiO_2 (red) TiO_2/Au/TiO_2 (orange) and TiO_2 (blue), respectively. (c) Schematic illustration of PbS QDs/TiO_2/Au/TiO_2 electrode in contact with S^{2-}/S_n^{2-} redox couple. The conduction and valence band edge position was calculated in regard to the average size evaluated from the 1st exciton wavelength of 1344 nm.[36, 41] The flat band energy of TiO_2 with respect to Ag/AgCl (sat.KCl) refer to anatase[42, 43] in alkaline aqueous solution (pH=13). Enhanced near-field generated by LSPR is confined between Au NP and PbS QD.[10, 11]

4.4 Conclusions

Electrochemical surface-enhanced Raman scattering and corresponding photocurrent were measured simultaneously for PbS QDs-sensitized plasmonic photoelectrochemical cell. Raman intensity of polysulfur vibrations and photocurrent were observed at the positive polarization, because the variation in the Fermi level controlled by potential altered the potential gradient in TiO_2 and subsequently influences the efficiency of electron-hole separation in PbS QDs. Effective hole scavenging from PbS QDs by S^{2-} at the interfaces was successfully monitored by the present method. Such coupling techniques provide a robust way in better understanding charge separation processes of QDs-sensitized photoenergy conversion devices.

Reference

1. Bozyigit, D.; Lin, W. M. M.; Yazdani, N.; Yarema, O.; Wood, V. *Nat Commun* **2015,** 6.
2. Wang, D.; Zhao, H.; Wu, N.; El Khakani, M. A.; Ma, D. *The Journal of Physical Chemistry Letters* **2010,** 1, (7), 1030-1035.
3. Ratanatawanate, C.; Tao, Y.; Balkus, K. J. *The Journal of Physical Chemistry C* **2009,** 113, (24), 10755-10760.
4. Wang, C.; Thompson, R. L.; Ohodnicki, P.; Baltrus, J.; Matranga, C. *Journal of Materials Chemistry* **2011,** 21, (35), 13452-13457.
5. Kang, Q.; Liu, S.; Yang, L.; Cai, Q.; Grimes, C. A. *ACS Applied Materials & Interfaces* **2011,** 3, (3), 746-749.
6. Ratanatawanate, C.; Xiong, C.; Balkus, K. J. *ACS Nano* **2008,** 2, (8), 1682-1688.
7. Bubenhofer, S. B.; Schumacher, C. M.; Koehler, F. M.; Luechinger, N. A.; Grass, R. N.; Stark, W. J. *The Journal of Physical Chemistry C* **2012,** 116, (30), 16264-16270.
8. Acharya, K. P.; Hewa-Kasakarage, N. N.; Alabi, T. R.; Nemitz, I.; Khon, E.; Ullrich, B.; Anzenbacher, P.; Zamkov, M. *The Journal of Physical Chemistry C* **2010,** 114, (29), 12496-12504.
9. Leventis, H. C.; O'Mahony, F.; Akhtar, J.; Afzaal, M.; O'Brien, P.; Haque, S. A. *Journal of the American Chemical*

Society **2010,** 132, (8), 2743-2750.

10. Li, X.; Suzuki, K.; Toda, T.; Yasuda, S.; Murakoshi, K. *The Journal of Physical Chemistry C* **2015,** 119, (38), 22092-22101.
11. Hutter, T.; Mahajan, S.; Elliott, S. R. *Journal of Raman Spectroscopy* **2013,** 44, (9), 1292-1298.
12. Kawawaki, T.; Tatsuma, T. *Physical Chemistry Chemical Physics* **2013,** 15, (46), 20247-20251.
13. Sukhovatkin, V.; Hinds, S.; Brzozowski, L.; Sargent, E. H. *Science* **2009,** 324, (5934), 1542-1544.
14. Sambur, J. B.; Novet, T.; Parkinson, B. A. *Science* **2010,** 330, (6000), 63-66.
15. Semonin, O. E.; Luther, J. M.; Choi, S.; Chen, H.-Y.; Gao, J.; Nozik, A. J.; Beard, M. C. *Science* **2011,** 334, (6062), 1530-1533.
16. Yuan, M.; Liu, M.; Sargent, E. H. *Nature Energy* **2016,** 1, 16016.
17. Maturova, K.; Nanayakkara, S. U.; Luther, J. M.; van de Lagemaat, J. *Nano Letters* **2013,** 13, (6), 2338-2345.
18. Correa, R. E.; Dauler, E. A.; Nair, G.; Pan, S. H.; Rosenberg, D.; Kerman, A. J.; Molnar, R. J.; Hu, X.; Marsili, F.; Anant, V.; Berggren, K. K.; Bawendi, M. G. *Nano Letters* **2012,** 12, (6), 2953-2958.
19. Padilha, L. A.; Stewart, J. T.; Sandberg, R. L.; Bae, W. K.; Koh, W.-K.; Pietryga, J. M.; Klimov, V. I. *Accounts of Chemical Research* **2013,** 46, (6), 1261-1269.
20. Stewart, J. T.; Padilha, L. A.; Qazilbash, M. M.; Pietryga, J. M.; Midgett, A. G.; Luther, J. M.; Beard, M. C.; Nozik, A. J.; Klimov, V. I. *Nano Letters* **2012,** 12, (2), 622-628.
21. Midgett, A. G.; Luther, J. M.; Stewart, J. T.; Smith, D. K.; Padilha, L. A.; Klimov, V. I.; Nozik, A. J.; Beard, M. C. *Nano Letters* **2013,** 13, (7), 3078-3085.
22. Nootz, G.; Padilha, L. A.; Levina, L.; Sukhovatkin, V.; Webster, S.; Brzozowski, L.; Sargent, E. H.; Hagan, D. J.; Van Stryland, E. W. *Physical Review B* **2011,** 83, (15), 155302.
23. El-Ballouli, A. a. O.; Alarousu, E.; Usman, A.; Pan, J.; Bakr, O. M.; Mohammed, O. F. *ACS Photonics* **2014,** 1, (3), 285-292.
24. Geiregat, P.; Delerue, C.; Justo, Y.; Aerts, M.; Spoor, F.; Van Thourhout, D.; Siebbeles, L. D. A.; Allan, G.; Houtepen, A. J.; Hens, Z. *ACS Nano* **2015,** 9, (1), 778-788.
25. Knowles, K. E.; Malicki, M.; Weiss, E. A. *Journal of the American Chemical Society* **2012,** 134, (30), 12470-12473.
26. Knowles, K. E.; Malicki, M.; Parameswaran, R.; Cass, L. C.; Weiss, E. A. *Journal of the American Chemical Society* **2013,** 135, (19), 7264-7271.
27. Aruda, K. O.; Bohlmann Kunz, M.; Tagliazucchi, M.; Weiss, E. A. *The Journal of Physical Chemistry Letters* **2015,** 6, (14), 2841-2846.
28. Knowles, K. E.; Tagliazucchi, M.; Malicki, M.; Swenson, N. K.; Weiss, E. A. *The Journal of Physical Chemistry C* **2013,** 117, (30), 15849-15857.
29. Bakulin, A. A.; Neutzner, S.; Bakker, H. J.; Ottaviani, L.; Barakel, D.; Chen, Z. *ACS Nano* **2013,** 7, (10), 8771-8779.
30. Gao, J.; Johnson, J. C. *ACS Nano* **2012,** 6, (4), 3292-3303.
31. Chung, H.; Choi, H.; Kim, D.; Jeong, S.; Kim, J. *The Journal of Physical Chemistry C* **2015,** 119, (13), 7517-7524.
32. Chakrapani, V.; Baker, D.; Kamat, P. V. *Journal of the American Chemical Society* **2011,** 133, (24), 9607-9615.
33. Xiaowei Li, T. T., Hiro Minamimoto, Kei Murakoshi. *Nano Letters* **2016**.
34. Hagen, M.; Schiffels, P.; Hammer, M.; Dörfler, S.; Tübke, J.; Hoffmann, M. J.; Althues, H.; Kaskel, S. *Journal of The Electrochemical Society* **2013,** 160, (8), A1205-A1214.
35. Yang, Y.; Rodríguez-Córdoba, W.; Xiang, X.; Lian, T. *Nano Letters* **2012,** 12, (1), 303-309.

36. Moreels, I.; Lambert, K.; Smeets, D.; De Muynck, D.; Nollet, T.; Martins, J. C.; Vanhaecke, F.; Vantomme, A.; Delerue, C.; Allan, G.; Hens, Z. *ACS Nano* **2009,** 3, (10), 3023-3030.
37. Nishijima, Y.; Ueno, K.; Kotake, Y.; Murakoshi, K.; Inoue, H.; Misawa, H. *The Journal of Physical Chemistry Letters* **2012,** 3, (10), 1248-1252.
38. Zhong, Y.; Ueno, K.; Mori, Y.; Shi, X.; Oshikiri, T.; Murakoshi, K.; Inoue, H.; Misawa, H. *Angewandte Chemie International Edition* **2014,** 53, (39), 10350-10354.
39. Zhang, W. F.; He, Y. L.; Zhang, M. S.; Yin, Z.; Chen, Q. *Journal of Physics D: Applied Physics* **2000,** 33, (8), 912.
40. Choi, H. C.; Jung, Y. M.; Kim, S. B. *Vibrational Spectroscopy* **2005,** 37, (1), 33-38.
41. Jasieniak, J.; Califano, M.; Watkins, S. E. *ACS Nano* **2011,** 5, (7), 5888-5902.
42. Kavan, L.; Grätzel, M.; Gilbert, S. E.; Klemenz, C.; Scheel, H. J. *Journal of the American Chemical Society* **1996,** 118, (28), 6716-6723.
43. Beranek, R. *Advances in Physical Chemistry* **2011,** 2011, 20.

Appendix

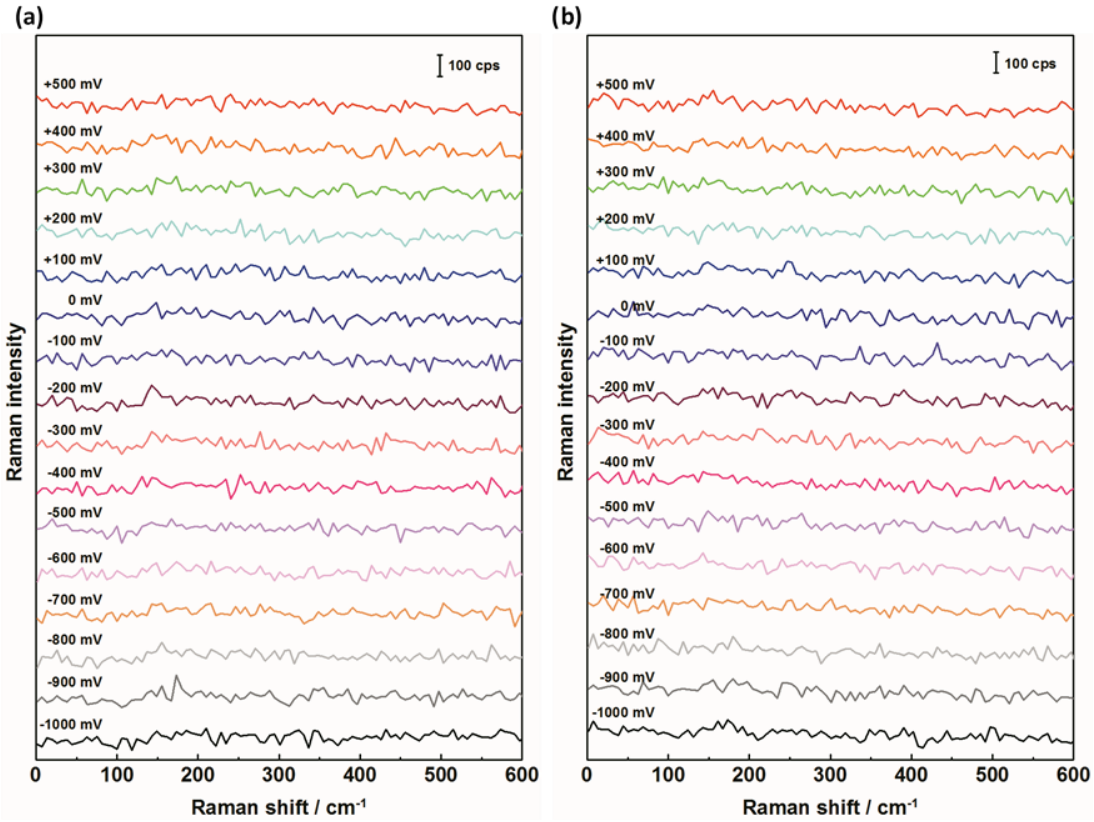

Figure A4.1. Potential-dependent EC-SERS spectrum of (a) TiO_2/Au/TiO_2 and (b) TiO_2 scanned potential from -1 V to +0.5 V (vs. Ag/AgCl) in electrolyte of 0.05 M Na_2S+0.1 M NaOH aqueous solution. Raman spectrum and corresponding photocurrent signals were recorded simultaneously and irradiated for 30 s by a laser of 514.8 nm with the intensity of 0.08 mW.

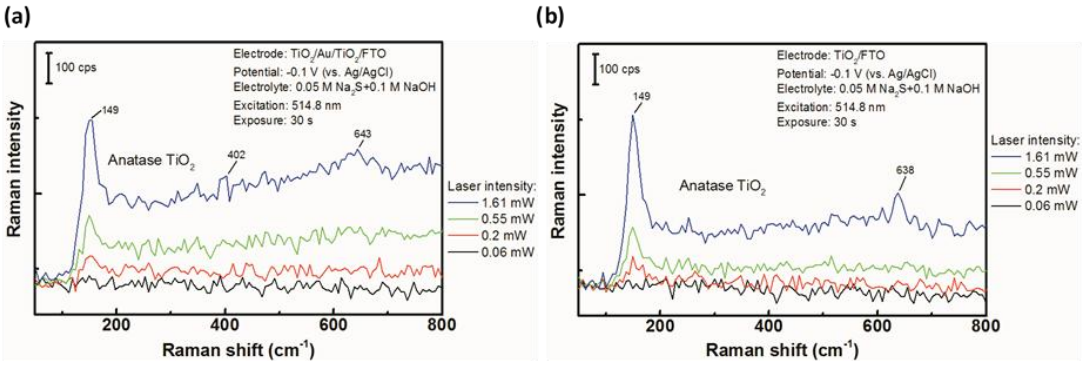

Figure A4.2. Excitation intensity-dependent EC-SERS spectrum of TiO_2/Au/TiO_2 (a) and TiO_2 (b) irradiated for 30 s by 514.8 nm under potential of -0.1 V (vs. Ag/AgCl) in electrolyte of 0.05 M Na_2S+0.1 M NaOH aqueous solution. Vibration modes at 149 cm^{-1} (E_g), and 643 cm^{-1} (E_g) were assigned as anatase TiO_2. Decreased E_g mode at 149 and 643 cm^{-1} is due to a fewer amount of TiO_2 in the 2nd layer covering Au NPs (less than 10 nm whereas about 100 nm for the 1st layer[10]). Enhanced B_{1g} mode at 402 cm^{-1} and background at higher laser intensity comes from localized surface plasmon resonance of Au NPs.

Chapter 5

Enhanced Photocurrent Generation in Visible Light Region using PbS Quantum Dots Coupled with Au Nanostructures on TiO_2 Electrode

5.1 Introduction

Plasmon-induce photoexcitation, owing to localized surface plasmonic resonance (LSPR), can be applied to break a limit of photoenergy conversion via changing photoenergy localization and the lifetime of excited states of materials[1-3]. The noble metal's free electrons strongly oscillate in phase with the varying electric field of the incident light, giving rise to an intensive local electric field, which powers the excitation of more electrons and holes.[4] The electromagnetic field of localized plasmons can be tailored by changing the structure of the metal at the nanometer scale.[5, 6] Various studies have focused on the application of the localized field at electrified interfaces for enhanced photo-electrical conversion,[7, 8] photocatalytic reaction,[9, 10] optical nanofabrication[11], enhanced illumination,[12] and the modification of the selection rule of electronic excitation of an isolated single-walled carbon nanotube[13] or dye molecule.[14]

Further tuning of the target energy of photons would be realized by using quantum dots (QDs) to sensitize tailored systems, because of the capability to present quantum confinement with diameters smaller than the Bohr radius of their exciton.[15] Lead sulfide (PbS) has relatively smaller effective masses both of electron and hole, resulting in metallic properties, such as large dielectric constant and characteristic Bohr radius of exciton (R_{ex}(PbS)=18 nm), which is significantly larger than that of typical compound semiconductors (*cf.* R_{ex}(CdS)=3 nm). Therefore, the quantized confinement could be more precisely tuned.[16] PbS QDs with size variation are easily prepared with inexpensive and relatively safe synthesis.[17-19] Size-dependent nonlinear optical properties, such as refractive index,[20, 21] lifetime of excited states,[22, 23] and transfer time of exited electron and hole,[24, 25] consequently play an essential role in a PbS QDs sensitized system, especially for the promising process of multiple exciton generation (MEG), which proposes a way to enhance the photo-electric conversion efficiency because of the creation of two electron-hole pairs from a single high energy photon.[26-30] The photovoltaic response of PbS QDs via MEG, however, is only available at relatively

short wavelength, typically λ <500 nm, which limits its application to visible response. The electronic properties of QDs are critically dependent on the nature of capping ligand molecules on their surfaces. Recent studies have indicated that the species of capping ligands to passivate a QD's surface defects serve as a considerable factor in electron transfer from an excited PbS QD into photovoltaic devices.[31, 32] In addition, research on SERS has reported that Raman signals of organic molecules adsorbed onto the surfaces of PbS QDs can be enhanced, ascribed to chemical effects.[33]

In this sense, nanoscale integration of noble metal nanoparticles (MNPs) and semiconductor QDs is particularly promising because of their controllable optical properties: a strong continuous spectral response (dielectric-confined electromagnetic modes) in MNP whereas discrete exciton energies of QD.[34, 35] When these two material systems are combined into heterostructures within nanometer-scale, the long-range Coulomb interaction between them leads to a dipole-dipole interaction, which will allow the tailoring absorption and emission properties,[36-38] local electromagnetic field enhancement,[39, 40] creation of new excitations in the strong-coupling regime,[41] and controllable nanoscale energy-transfer processes.[42-44] Theoretical calculations have shown that electric-field enhancement is available by coupling PbS QDs with Au NPs owing to metallic resonance because of the metallic properties of PbS, and the enhancement is strongly dependent on their sizes and distance.[45] A recent study has demonstrated that PbS QDs sensitized photocurrent can be enhanced by gold nanoparticles owing to LSPR, and QD-NP spacing dependent enhancement was ascribed to the competition of the plasmonic near field and Förster resonance energy transfer.[46] Effective enhancement was observed at relatively longer wavelength region (λ >600 nm), close to the bandgap exciton wavelength of PbS QDs prepared by the successive ionic layer adsorption and reaction (SILAR) method. Further improvement has also been expected at visible region where plasmonic enhancement is available. Compared to colloid PbS QDs, the prepared PbS QDs via the SILAR method has difficulties in tuning QDs' size smaller than 5 nm, consequently the size-dependent electronic states and optical properties for the sensitization in visible region remain challenging. Sensitization methods employing in-situ growth techniques of SILAR may also consider the recombination processes of excited electrons and holes due to the unpassivated surface as well as the formation of QD clusters.[47] Thus, it could be consequentially essential and meaningful to discover the coupling effect of plasmonic Au NPs with metallic PbS QDs by tuning QDs' size to

enhance photoelectric conversion under visible light irradiation.

The aim of this work reported in this paper is to expand the resonance region by coupling plasmonic Au NPs with size-controlled ultra-small PbS QDs not only in near infrared but also in visible light region, and to study the electric field enhancement contribution in the photocurrent generation based on photo-electrochemical measurement. Owing to the relatively small effective masses of carrier, semiconductor PbS QDs exhibit metallic properties, which is reasonable to well couple with gold NPs and will enhance the localized electromagnetic field. I change the capping ligand of PbS QDs from isolated long-chain molecules of oleic acid (OA) into short-chain molecules of 3-mercaptopropionic acid (MPA) and find that the ligand exchange process reduces the core size of QDs via the absorption spectrum. I deposit these two different size of PbS QDs capped respectively with MPA or OA on TiO_2/Au/TiO_2 nanoparticle substrates, in which TiO_2 are prepared via liquid phase deposition (LPD). The effect of LSP on the enhancement of the photocurrent is discussed based on the wavelength dependence of the enhancement at the substrate with distinct amounts of MPA- and OA-capped PbS QDs on the substrate.

5.2 Experimental

5.2.1 Ligand Exchange

3-MPA was dissolved in methanol with the concentration of 10 mM; pH of the solution was adjusted to 11 by TMAH. The solution was degassed for 30 min by Argon. Then different volume of 200 μM original OA-capped PbS QDs was added into 1 mL of the MPA solution to dilute the original solution for various folds (see Table.1 in SI).

5.2.2 Preparation of PbS QDs Sensitized Electrode

Original OA-capped PbS QDs solution was diluted for different folds by Toluene (see Table.2 in SI). 40 μL of MPA- or OA-capped PbS QDs solution with diluted concentrations was dripped onto the substrates of bare TiO_2 or TiO_2/Au/TiO_2 substrates to cover the whole 4 cm^2 square substrate. The excess MPA molecules were well washed down by methanol.

5.2.3 Morphology Characterization

The morphology of the electrode was measured by field-emission scanning electron microscopes (FE-SEM, JSM-6700FT), using 5.0 kV electron beam with a magnification of 100,000 times.

5.2.4 Photo-Electrochemical Measurement

Incident photon to current efficiency (IPCE) spectra were measured using a system (see Figure A5.2). Illumination from a 500 W Xenon lamp (USHIO optical modulex) was cut off for visible light by using 440 and 800 nm filters (SCH-50s-44Y and CLDF-50s, SIGMA KOKI Co., Ltd.), and then passed through a computer controlled grating monochromator (Oriel cornerstone 130 1/8 m). A power meter (MELLES GRIOT broadband power/energy meter 13PE M001, Microprecision Calibration Inc.) was used to measure the incident power through the monochromator for the photocurrent measurement.

Steady-state on-off photocurrent responses were monitored at -0.1 V (against a Ag/AgCl(sat.KCl) reference electrode) with a computer-controlled potentiostat (HABF-501A, Hokuto Denko). The photocurrent was recorded by an amplifier (SRS SIM900 mainframe, Stanford Research Systems) connected between a counter electrode of Pt coil and the working electrode of MPA- or OA-capped PbS QDs sensitized TiO_2/Au/TiO_2 substrate in the electrolyte of 0.05 M Na_2S+ 0.1 M NaOH aqueous solution.

5.2.5 Calculation for IPCE

The incident photon-current conversion efficiency (IPCE) of the PbS QDs sensitized substrates as a working electrode is calculated by the following formula, where I and φ are respectively the photocurrent density and power intensity density at a wavelength of λ.

$$\text{IPCE (\%)} = \frac{1240 \cdot I}{\lambda \cdot \varphi} \times 100$$

The IPCE, equaled to the external quantum efficiency (EQE), is determined as the ratio of the number of electrons to the number of irradiated photons; however, what is neglected is the number of the actual absorbed photon. Since absorbance efficiency scales with cubic diameter of nanoparticle, it is rational to consider that PbS QD with larger size will absorb more photons than

the smaller one, that OA-capped PbS QDs will yield higher IPCE than MPA-capped ones. However, only the extinction of the PbS QDs sensitized substrates are able to be measured in this work (see Figure S4 in SI) and the scattering counterpart remains unknown, hence it is difficult to determine the absorbance of QDs dripped on substrates.

5.3 Results and discussion

5.3.1 Structure of TiO_2 Electrodes

Since the liquid phase deposition (LPD) process enables a uniform layer of TiO_2 film to homogeneously coat on the entire surface of substrates, and the thickness of film is tunable by simply controlling the deposition time,[48] a construction of TiO_2/Au/TiO_2 was prepared by respectively depositing thin TiO_2 film on FTO glass for 12 h via LPD, gold film with thickness of 5 nm on the TiO_2 via electric beam vaporization, and a 2nd thin TiO_2 film on Au for 1 h via LPD (see Figure S1 in SI). 500 ^{o}C was chosen as the annealing temperature for the formation of Au NPs from continuous film according to our best IPCE results of Au/TiO_2 by comparing the annealing temperature of Au layer up to 200, 300, 400 and 500 ^{o}C, respectively. Then, a solution of PbS QDs with different sizes and capped ligands of MPA or OA were dripped onto the substrate. The high-resolution SEM images of TiO_2/Au/TiO_2 substrates sensitized with PbS QDs are shown in Figure 5.1.

The characterization of the TiO_2/Au/TiO_2 structure illustrates that gold nanoparticles, with an average size around 20 nm, are well dispersed on the TiO_2 surface without dissolution even after deposition of PbS QDs (Figure 5.1c and d). PbS QDs were quite reasonable not to be observed via SEM whose resolution is limited for our ultra-small PbS QDs with average diameter less than 3 nm (details are presented in the next section).The thickness of the microcrystalline thin film structure of the 1st TiO_2 layer is about 100 nm (cross section image in Figure 5.1b), while the thickness of the 2nd TiO_2 layer is less than 10 nm according to the experimental film formation rate.[49] The distance between PbS QDs and Au NPs should be appropriate to prevent quenching of the excited states leading to enhanced photocurrent under plasmon-excitation as demonstrated in the previously documented results.[46]

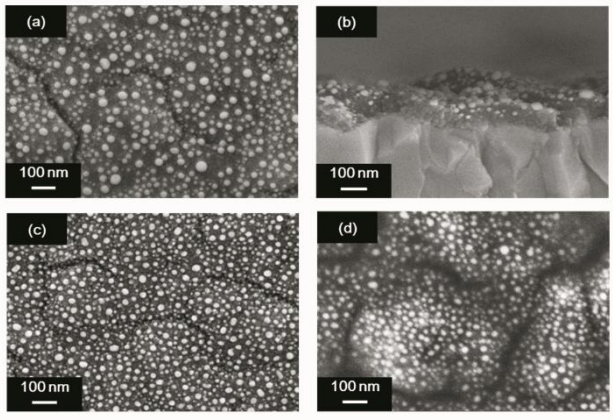

Figure 5.1. SEM images of (a) bare TiO_2/Au/TiO_2 substrate, (b) the cross section image of TiO_2/Au/TiO_2 substrate, (c) MPA-capped TiO_2/Au/TiO_2 substrate (PbS particle density: 2.4 x 10^{13} cm^{-2}), and (d) OA-capped PbS QDs/TiO_2/Au/TiO_2 substrate (PbS particle density: 2.4 x 10^{14} cm^{-2})

5.3.2 Substrate-dependent enhanced IPCE

Photo-electrochemical measurements were performed via a three electrodes system in an electrolyte solution containing Na_2S and NaOH (pH=13) (Figure S2 in SI). Anodic photocurrents were observed at the steady-state on-off responses under visible and near-infrared light illumination when the substrates were polarized more positive than -0.5 V. Constant polarized potential of -0.1 V was chosen for all the measurements because of sufficiently larger photocurrent responses without the background interference duo to the large dark current in positive potential region (see *I-V* characteristics in Figure S5 and S6 of SI).

As for colloid PbS QDs, the average bandgap of OA- and MPA-capped PbS QDs were determined by the absorption maximum corresponding to the 1st exciton peak (Figure S3 in SI), giving 1.6 and 2.3 eV, respectively. The average diameters of OA- and MPA-capped PbS QDs were estimated to be 2.4 and 1.6 nm in diameter,[50] respectively. Within the Bohr radius of 18 nm, both OA- and MPA-capped PbS QDs exhibit strong quantum confinement; in particular, the smaller PbS QDs capped with MPA present a larger bandgap. Figure 5.2a shows the valence band and the conduction band potentials of PbS QDs, which were calculated according to the size-dependent ionization energy and values of bulk PbS (E_g=0.41 eV, E_{CB}=-0.29 V, E_{VB}=0.12 V (vs. Ag/AgCl)).[51] The flat-band potential of anatase TiO_2 prepared by the LPD method was estimated to be at -0.83 V based on the Mott-Schottky plot of the present LPD substrates and previously documented values of the band-edge shifts of TiO_2 for 0.059 V/ pH at 298 K.[52] Both kinds of PbS QDs exhibit more negative

conduction band potential than that of TiO_2; it is therefore reasonable for the electrons to transfer from PbS CB into TiO_2 CB in the present system. The observed photocurrents are ascribed to the electron injection into the conduction band of TiO_2 from excited PbS QDs accompanied by electron transfer from the donor in the electrolyte under positive polarization for effective charge separation[53] (Figure 5.2b).

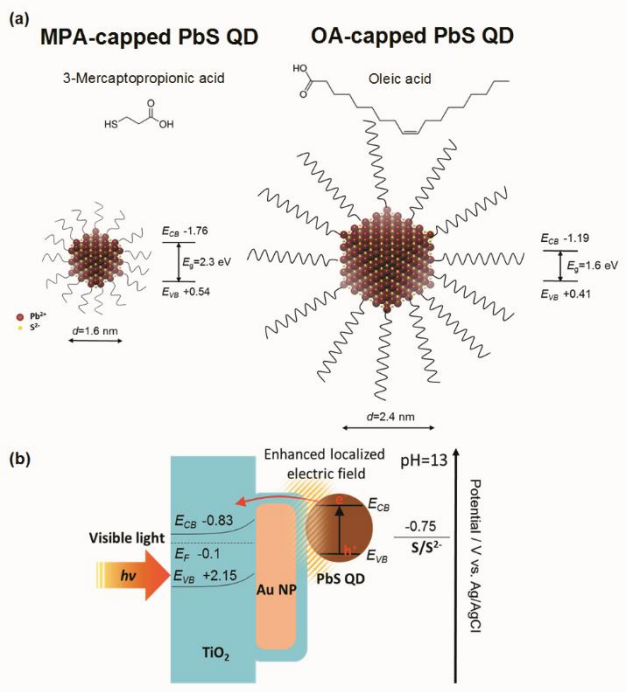

Figure 5.2. Schematic illustration of (a) the band energy of MPA- and OA-capped PbS QDs, (b) schematic energy diagram of PbS QDs/TiO_2/Au/TiO_2 system.

The comparison of IPCE values of the TiO_2 substrates before and after being sensitized with MPA-capped PbS QDs is presented in Figure 5.3. Before the sensitization (the data in the bottom of Figure 5.3), the enhanced IPCE owing to Au nanoparticles was apparently observed at a wavelength range between 500 and 700 nm, when the IPCE spectrum using the TiO_2 substrate in the absence of Au nanoparticles (Figure 5.3a) was compared with the IPCE spectrum using Au/TiO_2 (Figure 5.3b) as well as TiO_2/Au/TiO_2 (Figure 5.3c). After the sensitization of MPA-capped PbS QDs (the data in the bottom of Figure 5.3), the enhanced IPCE was observed below 600 nm for TiO_2 substrate (Figure 5.3a), as well as an additional broad feature around 580 nm of the IPCE of Au/TiO_2 and TiO_2/Au/TiO_2 substrates, which suggests the contribution of the plasmonic resonance owing to the enhanced electric field by coupling Au NPs with PbS QDs.[45]

A second TiO_2 thin layer played essential rule in enhancing the photo-electric conversion

efficiency. First, in the case without PbS QDs sensitization (Figure 5.3, the data in the bottom), the photocurrents generated by Au/TiO_2 (Figure 5.3b) in the wavelength range of 500-700 nm were considered to be the electron injection from excited Au NPs injected into TiO_2, as the donor of S^{2-} in the electrolyte directly contacts with Au NPs and consequently transferred electrons from S^{2-} to Au NPs. When Au NPs were covered by TiO_2, the photocurrents in the same wavelength range (Figure 5.3c, data in the bottom) were diminished, suggesting sufficient suppression of the electron injection from Au NPs. The result also indicates that the electron transfer from S^{2-} donor to Au NPs is prevented by this TiO_2 layer on Au NPs, which can act as an insulating layer for electrons with corresponding electrochemical potential.

Second, in the case that PbS QDs sensitized the plasmonic substrates (Figure 5.3, the data in the top), the enhancement of the TiO_2/Au/TiO_2 substrate (Figure 5.3c) is significantly larger than that of Au/TiO_2 substrate (Figure 5.3b). In addition to effective electron injection from PbS QDs to TiO_2, the space between PbS QDs and the Au surface by the 2nd layer of TiO_2 contributes to the prevention of the exciton quenching from PbS QDs to Au NPs via Förster resonance energy transfer[46]. The present result proves the importance of the second TiO_2 thin layer deposited on Au/TiO_2 for higher IPCE after being sensitized with PbS QDs in a plasmonic wavelength range as originally demonstrated in the previous study.[46] The induced enhanced electric field confined to the gap between the coupled Au NPs and PbS QDs resonantly excites electrons from PbS QDs to inject into TiO_2, and therefore enhanced the IPCE spectrum. Those results demonstrate the validity of plasmon enhancement on the quantized particles at a relatively wide wavelength region between visible and near infrared.

Weak photocurrent generated by TiO_2 under visible light irradiation in the absence of PbS QDs (Figure 5.3a) was considered to be coming from contact with donor of S^{2-} in electrolyte. The surface oxygen atoms in TiO_2 were thought to be substituted and doped by S^{2-} so that bandgap of TiO_2 was modified and minimized resulting in photoelectric response under visible light.[54, 55] Although the process was also enhanced by Au NPs owing to the electric field by LSPR (Figure 5.3c), the contribution is minor compared with the enhancement of PbS QDs sensitized photocurrent.

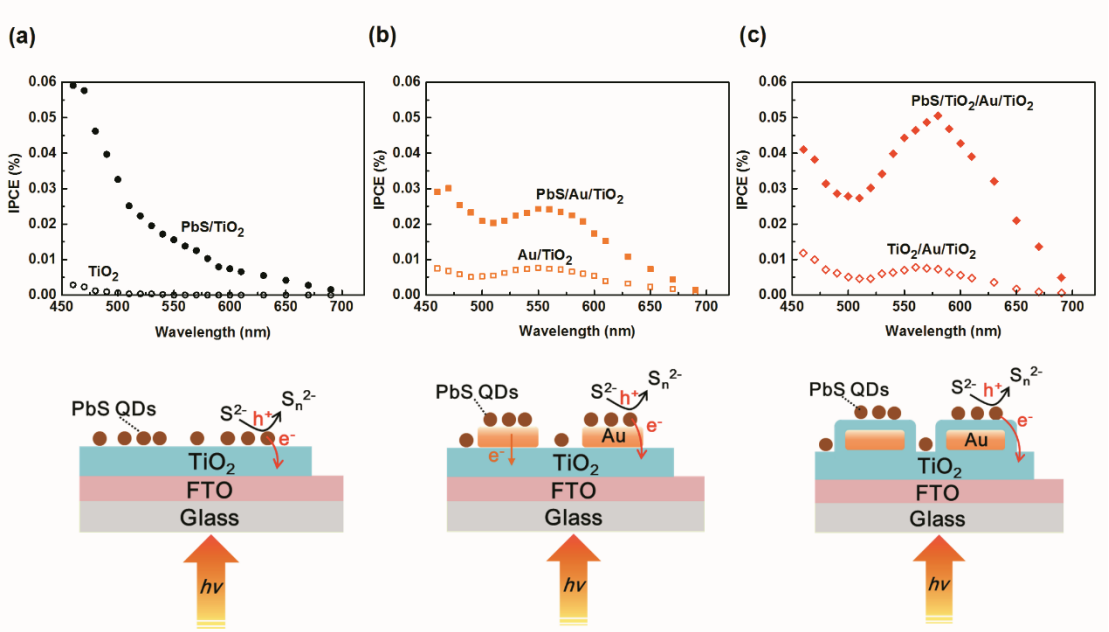

Figure 5.3. Comparison of substrate-dependent IPCE results before and after sensitized by MPA-capped PbS QDs (PbS particle density: 2.4 x 10^{12} cm^{-2}): (a) TiO_2, (b) Au/TiO_2 and (c) $TiO_2/Au/TiO_2$ substrate. All experiments were measured with the same condition: potential: -0.1 V, electrolyte: 0.05 M Na_2S+0.1 M NaOH, irradiation wavelength range: 440~800 nm. Schematic illustration of the substrates' structures as well as electron-hole pairs' pathways are respectively listed below.

5.3.3 Comparison of enhanced IPCE spectra using distinct sizes of PbS QDs

The characteristics of the plasmonic enhancement at visible wavelength region were compared using distinct sizes of colloid PbS QDs capped with MPA or OA molecule (Figure 5.4). Significant enhancement was observed for both kinds of PbS QDs sensitized $TiO_2/Au/TiO_2$ structure in plasmonic wavelength range between 500 and 700 nm in comparison with PbS QDs/TiO_2 substrate. It has been suggested that the dipole-dipole interactions of the hetero-structures consisting of PbS QDs combined Au NPs are available due to their metallic character of the respective system[45]. Thus, PbS QDs are capable of coupling with gold NPs and enhancing the nearby electric field, resulting in increased IPCE.

Another worth noting characteristic of the enhancement on IPCE is the pronounced improvement at shorter wavelength range below 500 nm generated by MPA-capped smaller PbS QDs sensitized plasmonic substrate, in contrast with the unsatisfactory enhancement effect by OA-capped larger PbS QDs. Such discovery has not been reported by any research group. The effect at a shorter wavelength region could be considered in several ways. First is the contribution coming from the

quantized effect: stronger quantum confinement by a smaller QD expands the band gap energy, leading to effective injection of the excited electrons with relatively negative potential compared to the conduction band edge of TiO_2. Furthermore, the relatively strong inter-particle interaction of PbS QDs and Au NPs also plays an important role in enhancement. Theoretical research via photon Green's function method on coupled QD-MNP systems has proven that the interaction is strong when QD and MNP are in close proximity and their optical excitation frequencies are resonant with each other[35]. In the present system, larger spectral overlap of MPA-capped PbS QDs, whose exciton absorption peak is at 540 nm (E_g = 2.3 eV), with plasmon excitation of Au NPs at 500 – 700 nm (ca.1.8 eV< E < 2.5 eV) results in more effective resonance than that of OA-capped ones peaked at 750 nm (E_g = 1.6 eV).

The lack of change in IPCE of the OA-capped system in the presence of Au NPs in this short wavelength region suggests the absence of inter-particle interaction of the OA-capped PbS QDs with larger diameters with a different band gap energy than that of LSPR. The band gap energy at the near-infrared region (750 nm) can conduce to improved IPCE at the shorter wavelength region below 500 nm, because of the contribution of MEG as often observed is PbS QDs in previously documented results.[56] Unfortunately, the enhancement is not apparent possibly due to the mismatch of the LSPR energy of the present system with the excitation energy of OA-capped PbS QDs, although the effect of MEG is also expected to be enhanced by LSPR.[57] These characteristics of smaller MPA-capped PbS QDs when combined with Au NPs gives birth to more effective enhancement of IPCE in the visible wavelength region.

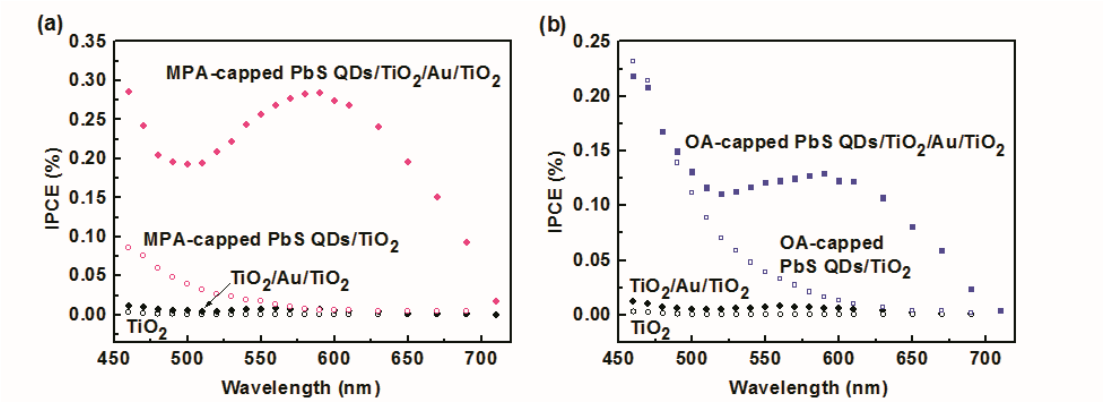

Figure 5.4. IPCE comparison of (A) MPA- and (B) OA- capped PbS QDs sensitized TiO_2 and TiO_2/Au/TiO_2 substrates. Measured at -0.1 V in electolyte of 0.05 M Na_2S+0.1 M NaOH. PbS particle densities are 7.2 x 10^{12} cm^{-2} and 4.8 x 10^{12} cm^{-2}, respectively for MPA- and OA-capped PbS QDs.

5.3.4 IPCE changes depending on the amount of PbS QDs loading

Further examinations were performed to evaluate the coupling effect by Au NPs with increasing loaded amounts of the MPA- or OA-capped PbS QDs by measuring the enhanced IPCE of TiO_2/Au/TiO_2 and TiO_2 substrates. The changes in IPCE depending on the amount of MPA- and OA-capped PbS QDs are shown in Figure 5.5. As the quantity of MPA-capped QDs increased up to a loading of 7.2 x 10^{13} cm^{-2} both on TiO_2/Au/TiO_2 and TiO_2 substrates (Figure 5.5a, b), the IPCE increased as a whole over the observed wavelength region. The IPCE increment of TiO_2/Au/TiO_2 in the LSPR wavelength region at 600 nm is larger than that of TiO_2, which is comparable to the shorter wavelength region below 500 nm. In the case of OA-capped PbS QDs (Figure 5c, d), IPCE also increased as the loading increased. The increments, however, saturated at relatively small amounts (2.4 x 10^{13} cm^{-2}) of the loading. The IPCE values of OA-capped PbS QDs on TiO_2/Au/TiO_2 (Figure 5.5c) are smaller than those in the absence of Au (Figure 5.5d) with relatively large loading of more than 1.2 x 10^{13} cm^{-2}.

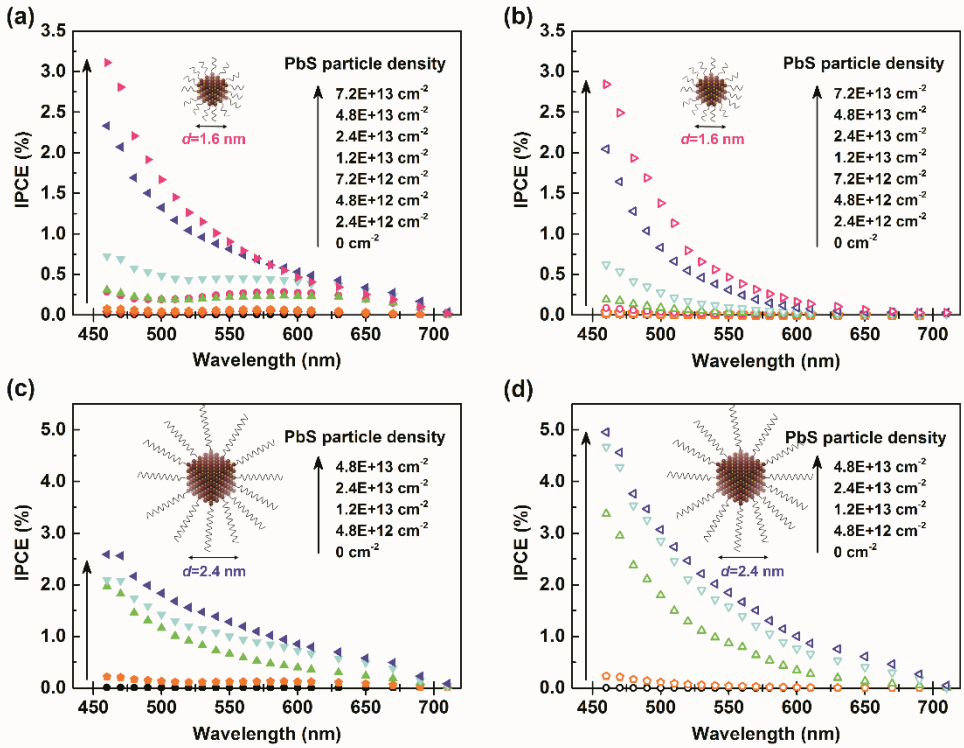

Figure 5.5. Comparison of IPCE changes depending on the loading amount of two kinds of PbS

QDs: (a) MPA-capped PbS QDs/TiO_2/Au/TiO_2 (solid scatter), (b) MPA-capped PbS QDs/TiO_2 (hollow scatter), (c) OA-capped PbS QDs/TiO_2/Au/TiO_2 (solid scatter), and (d) OA-capped PbS QDs/TiO_2 (hollow scatter) measured at -0.1 V in electolyte of 0.05 M Na_2S+0.1 M NaOH (black circle: 0 cm^{-2}; red rhombus: 2.4 x 10^{12} cm^{-2}; orange pantogon: 4.8 x 10^{12} cm^{-2}; pink circle: 7.2 x 10^{12} cm^{-2} (only for MPA- capped PbS QDs); green upper triangle:1.2 x 10^{13} cm^{-2}; cyan lower triangle:2.4 x 10^{13} cm^{-2}; violet left triangle: 4.8 x 10^{13} cm^{-2}; pink right triangle: 7.2 x 10^{13} cm^{-2} (only for MPA-capped PbS QDs)).

For further quantitative comparison of the enhancements between MPA- and OA-capped systems, the enhancement factor EF was introduced. In the present experiment, the loading amounts of PbS QDs both on the substrates with and without Au are carefully controlled to be the same as shown in Table 1 of the SI. Thus, all of the EF was calculated as the yielded IPCE ratio of PbS QDs/TiO_2/Au/TiO_2 substrate (with Au NPs) to PbS QDs/TiO_2 substrate (without Au NPs) at a certain wavelength, as described below.

$$\text{Enhancement Factor} = \frac{\text{IPCE}_{\lambda,\text{w/Au}}}{\text{IPCE}_{\lambda,\text{w/oAu}}}$$

Calculated EFs at visible light are presented in Figure 5.6. The EF was significant at the wavelength range longer than 530 nm, at which Au NPs exhibit plasmon resonance. The smaller PbS QDs generated a greater EF with a maximum of 48.5, while the maximum EF produced by larger PbS QDs was 20. The smaller PbS QDs also performed very well in a short wavelength range in contrast with the larger PbS QDs. The enhancements were outstanding owing to well spectrum overlap between Au NPs and ultra-small colloid PbS QDs because of strong quantum confinement, compared with the previous report[46] with a maximum EF value of 6 by PbS QDs larger than 5 nm synthesized via SILAR method.

The dependence of the loading on EF of respective PbS systems indicates that optimum amounts of loading are essential to construct the plasmon-enhanced photocurrent generation electrodes that should be tailored to the sizes and bandgap energies of PbS QDs. In the present system, significant EFs were observed at 7.2 x 10^{12} cm^{-2} and 4.8 x 10^{12} cm^{-2} of MPA- and OA-capped PbS QDs. Considering the numbers of PbS moles of MPA- and OA-capped PbS QDs covering the flat substrate with close-packing a single layer of 4.5 x 10^{13} cm^{-2} and 2.0 x 10^{13} cm^{-2}, roughly 20% coverage of PbS QDs is appropriate to prepare the plasmon-enhanced photocurrent generation system.

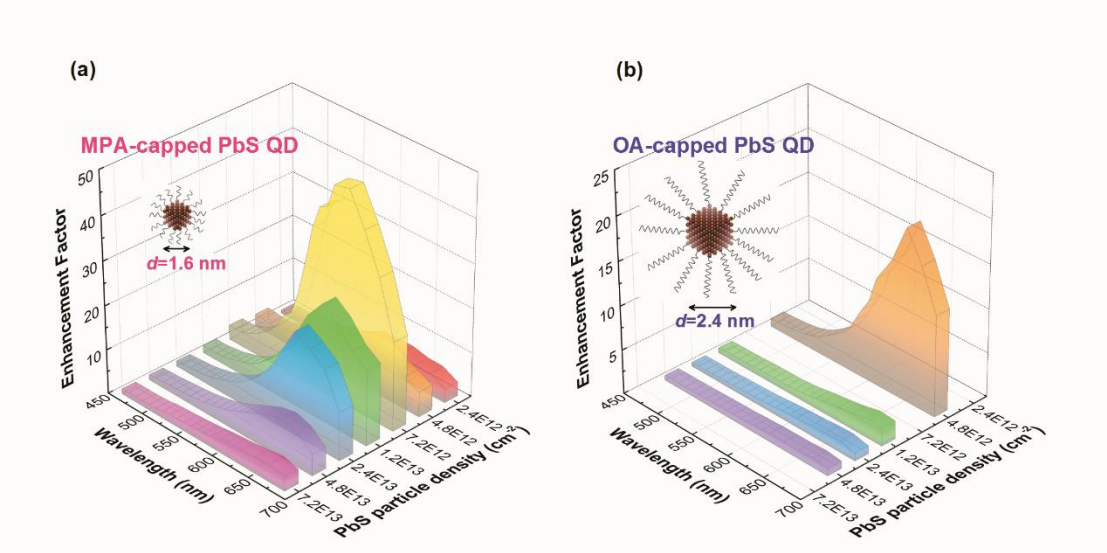

Figure 5.6. Comparison of enhancement factor changes depending on the loading amount of (a) MPA- and (b) OA-capped PbS QDs measured at -0.1 V in electolyte of 0.05 M Na_2S+0.1 M NaOH (red: 2.4 x 10^{12} cm^{-2}; orange: 4.8 x 10^{12} cm^{-2}; yellow: 7.2 x 10^{12} cm^{-2} (only for MPA- capped PbS QDs); green:1.2 x 10^{13} cm^{-2}; blue:2.4 x 10^{13} cm^{-2}; violet: 4.8 x 10^{13} cm^{-2}; pink: 7.2 x 10^{13} cm^{-2} (only for MPA- capped PbS QDs)).

5.3.5 Wavelength-dependent enhanced IPCE

Since absorbance efficiency scales with the volume of a nanoparticle, larger PbS QDs more effectively capture photons so that OA-capped PbS QDs yielded higher IPCE than MPA-capped ones. To discuss the PbS quantity dependence on IPCE in more detail, the EF values at 650, 560 and 460 nm are plotted as the function of the number of moles of PbS loaded on the substrates, as shown in Figure 5.7. The relation between the number of QD particles and the number of moles of PbS is summarized in Tables 5.1 and 5.2 of SI.

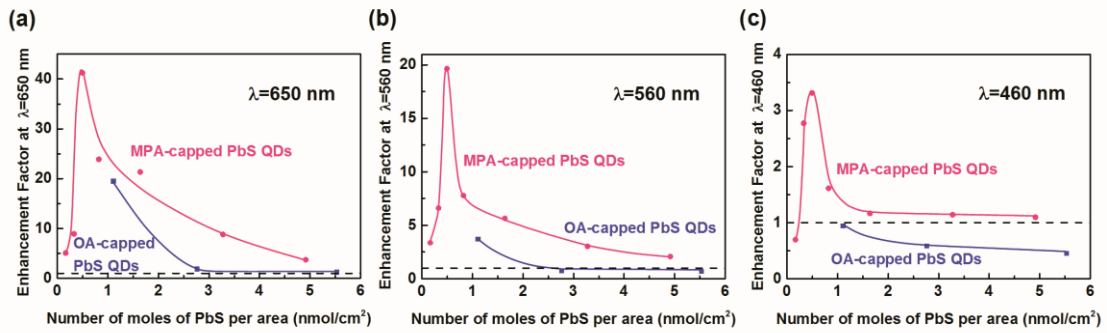

Figure 5.7. Comparison of MPA- and OA-capped PbS QDs loading amount dependent enhancement factor at different wavelength light irradiation of (a) 650 nm, (b) 560 nm and (c) 460 nm.

Under the illumination of 650 nm light (Figure 5.7a), the enhanced photocurrent is ascribed to the resonance enhancement of the band gap excitation by the localized electric magnetic field in the vicinity of metal nanoparticles. As reported previously, the apparent enhancement of IPCE depends on the quantity of PbS QDs[46]. The EF is generally higher when the amount of loading is relatively small. Saturation of IPCE increments was observed in the MPA-capped PbS QDs as well as OA-capped systems. The EF of MPA-capped system is much larger than that of the OA-capped system, and saturation is around 3.3 nmol/cm^2 of PbS (particle density of 4.8 x 10^{13} cm^{-2}). Although the IPCE improvement of OA-capped PbS QDs on TiO_2/Au/TiO_2 is not significant, the EF is apparently large at a loading of less than 2.8 nmol/cm^2 (particle density of 1.2 x 10^{13} cm^{-2}). The different saturation loading amount is considered to result from the size variation. This result suggests that the effect of LSPR saturates at this amount of loading.

Under the illumination of 560 nm light (Figure 5.7b), it could be possible that both band gap excitation and plasmonic enhanced electric fields are ways to generate photocurrent for the PbS QDs. Maximum EF of close to 20 is obtained by small loading (0.5 nmol/cm^2, particle density of 7.2 x 10^{12} cm^{-2}) of MPA-capped PbS QDs. At this wavelength, the EF of OA-capped PbS QDs is relatively small and decrease to reach unity at a higher loading of greater than 2.8 nmol/cm^2 (particle density of 1.2 x 10^{13} cm^{-2}). Similar tendency of the loading of EF was also observed in both MPA- and OA-capped systems at an irradiation of 460 nm (Figure 5.7c). Although the EF values of the MPA-capped PbS system are smaller than those at 560 nm, the maximum at a loading of 0.5 nmol/cm^2 (particle density of 7.2 x 10^{12} cm^{-2}) is also confirmed. At a higher loading of more than 1.6 nmol/cm^2 (particle density of 2.4 x 10^{13} cm^{-2}), the unity of EF indicates no enhancement. The value of the OA-capped system, however, decreases to less than unity at a higher loading.

In the present system, plasmon-enhanced photocurrent generation was apparently observed. The interaction between PbS QDs and Au NP depends on their distance. The dependence of IPCE on the amount of PbS QDs loading is a consequence of the interaction. It has been reported that the electromagnetic field owing to surface plasmon resonance is strongly dependent on distance, which localizes only in the vicinity of 10 nm around noble metal nanoparticles[58]. In this sense, within the plasmonic wavelength range, the PbS QDs/TiO_2/Au/TiO_2 system presents a tendency to be blurred and similar to that of the substrates without gold NPs (Figure 5.5a and Figure 5.7a), suggesting the

saturation of photo-electron conversion owing to the enhanced electric field by coupling PbS QDs with gold NPs. As for OA-capped PbS QDs sensitized plasmonic substrate, a similar saturation tendency was also observed although the plasmonic peak was not that apparent and the yielded relatively small IPCE.

Such phenomena are elucidated by pondering the relation between the quantity of PbS QDs and the enhancement of IPCE at the plasmon wavelength range of 500~700 nm. Within the domain that QDs close-pack a monolayer on the substrate, the yielding IPCE is considered a linear function of the mole number density of QDs because of the cumulative effect. The calculated mole number of PbS in MPA- and OA-capped PbS QDs covering the substrate (sensitized area of 4 cm^2) with a monolayer are respectively 3.1 and 4.7 $nmol/cm^2$ (particle density of 4.5×10^{13} and 2.0×10^{13} cm^{-2}, respectively), according to the estimated average diameters. As the quantity of QDs exceeds a monolayer, IPCE at that wavelength range displays a tendency to be saturated since farer QDs face difficulties not only in electrons' effective injection, but also in well coupling with gold NPs due to the vicinity of LSPR (Figure 5.7). Because the coupling distance between OA-capped PbS QD and Au NP is apparently the larger one, and the number of possible coupling hot-spots generated by large QDs is consequently less than that of small QDs; consequently, the electric field cannot be continuously enhanced (see the original IPCE of OA-capped ones in Figure S8).

The unique physical properties of PbS provides a clear insight for the PbS-Au coupling system. PbS exhibit metallic properties owing to the relatively small effective masses of electron and hole, and high refractive index compared to other semiconductors such as CdS. Although PbS QDs show relatively weak plasmon resonance under visible light irradiation, their presence simply increases the dielectric constant of the nano-environment surrounding Au NPs[59]; consequently, more induced polarization charges will pile up around the Au NP under an external electromagnetic excitation by incident light irradiation, which leads to stronger screening of the Coulombic restoring force, therefore confining the localized hybridized NP plasmon to the gap between PbS QDs and Au NP.

At the wavelength region below 500 nm, it is generally expected that multiple exciton generation and collection are accessible via such PbS QDs-Au NPs systems by well adjusting their tunable sizes and Au structure on a nanoscale. In the present system, OA-capped larger PbS QDs may generate multiple excitons because of lower threshold around 3 times of bandgap[56], leading to higher

IPCE below 500 nm compared with that of MPA, as shown in Figure 5.4. The contribution of the plasmon enhancement to the multiple exciton generation is not apparent or is rather negative, especially at a higher loading. Less than unity of EF at amounts greater than more than 2.8 nmol/cm^{-2} (particle density of 1.2 x 10^{13} cm^{-2}) OA-capped PbS implies difficulty in the collection of multiple excitons from stacked PbS QDs even when partially plasmon-enhanced.

5.3.6 Mechanism of enhancement

Effective enhancement both at the wavelength regions of 500 – 700 nm and below 500 nm was clearly demonstrated in the MPA-capped PbS system. Such phenomena are elucidated by pondering the naturally occurring dipole-dipole interactions when PbS QDs combined with Au NPs into hetero-structures. First, simulated results[45] have demonstrated that well-coupled metallic PbS QDs-metal NP system can generate metallic resonance and produce an enhanced electric field confined in the gap between them, because PbS has a small effective electron mass and behaves like metal; the higher the diameter ratio of Au NP to PbS QD, the larger the enhancement of the electric field confined between them owing to better scattering efficiency. The enhancement decreases with an increasing distance between PbS QDs and Au NPs, resulting in a coupling advantage by the 2nd layer of smaller PbS (Figure 5.7). In this case, it is sensible to conclude that small PbS QDs performed better coupled with Au NP. Thus, an apparent enhancement is available with the MPA-capped smaller one, both within long as well as short wavelength visible regions, owing to the metallic resonance. For the larger PbS QDs, significant enhancements were only observed within a long wavelength range, which is close to the bandgap exciton wavelength, so the enhancement is ascribed to bandgap resonance.

I utilized Finite-Difference Time-Domain method (FDTD) to simulate the electric field distribution of the PbS QD-Au NP hetero-system by assuming the size of PbS QDs to be 1.6 and 2.4 nm with a distance separated from Au NP of 0.6 nm and 2.0 nm in vacuum, respectively. The electric field generated by Au NP was confined within the gap between the Au NP and the near-by PbS QD, because of the unique dielectric and metallic property of PbS.[45] The wavelength-dependent electric field in the center line within the gap gives maximum value at 520-530 nm, which is comparable to the extinction spectrum (see Figure 5.8). Stronger electric field at slightly shorter

wavelength was generated by MPA-capped smaller PbS QD in comparison with the OA-capped larger PbS QD system (see Figure 5.9). The results indicate that the metallic property of PbS QD with smaller size at short gap distance has the advantage for the resonance at visible light region. Stronger confinement of the quantized states in MPA-capped PbS QDs also contributes to enhancement. The theoretical calculation demonstrates the availability of the remarkable performance of MPA-capped PbS QDs by well coupling with Au NP.

Besides the coupling effect, quantum confinement and capping ligands also play a crucial role in electron injection. In one respect, increased quantum confinement by smaller QDs expands the energetic distance, resulting in a boosted electron injection driving force and consequently the photocurrent. In another respect, here, it is logical to explain two different natural electronic properties of QDs: one is the electron mobility of the capping ligands, and the other is the chemical structure binding to TiO_2 nanoparticles. For the former, researches have reported that electronic mobility increases exponentially the ligand length decreases;[60] while for the latter, the covalent bond between TiO_2 and carboxyl of MPA is more conducive to electron transfer than the loose binding between TiO_2 and alkyl of OA. It is therefore rational to explain that compared to long-chain OA, short-chain MPA has the advantage of more effective electron transfer from excited PbS QD into TiO_2 and, consequently performs better in photo electric conversion. In conclusion, besides the unsatisfided coupling effect with Au NPs, the passivating and loosen ligand of OA molecules also limit the possiblity of gaining higher enhancement factors in the short wavelength light region, although within which many more electrons are expected to be excited because of the larger energy difference from the bandgap. As the electron injection from PbS QDs is strongly related with their luminescent decay rate which will be affected by the localized surface plasmon resonance in consideration of the plasmon damping,I are projecting to characterize the luminescence properties

of size- and ligand-controlled PbS QDs coupled with plasmonic nano-structure in the next stage.

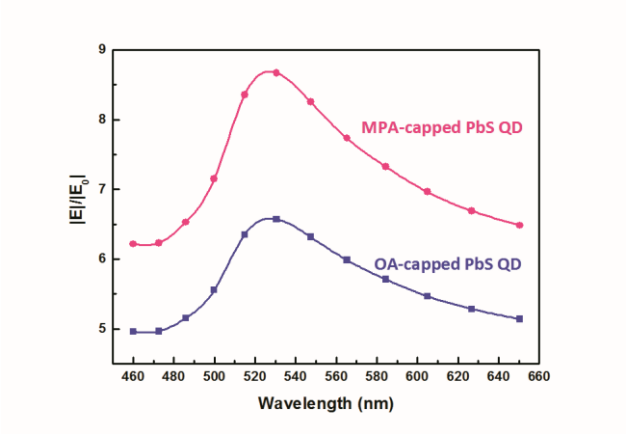

Figure 5.8. Results of FDTD simulation for Au-PbS hetero-system. Upper row: electric-field distribution excluding the incident field; lower row: the corresponding spatial electric-field distributions along the center line connecting Au and PbS (red dashed line). (a, c) System of Au (*D*=20 nm) and MPA-capped PbS QD (*d*=1.6 nm) separated with 0.6 nm at the gap at the wavelength of 531 nm; (b, d) system of Au (*D*=20 nm) and OA-capped PbS QD (*d*=2.4 nm) separated with 2.0 nm at the gap at the wavelength of 531 nm. Inset: schematic illustration of the system. The 0 point along z-axis was set as the center between Au and PbS.

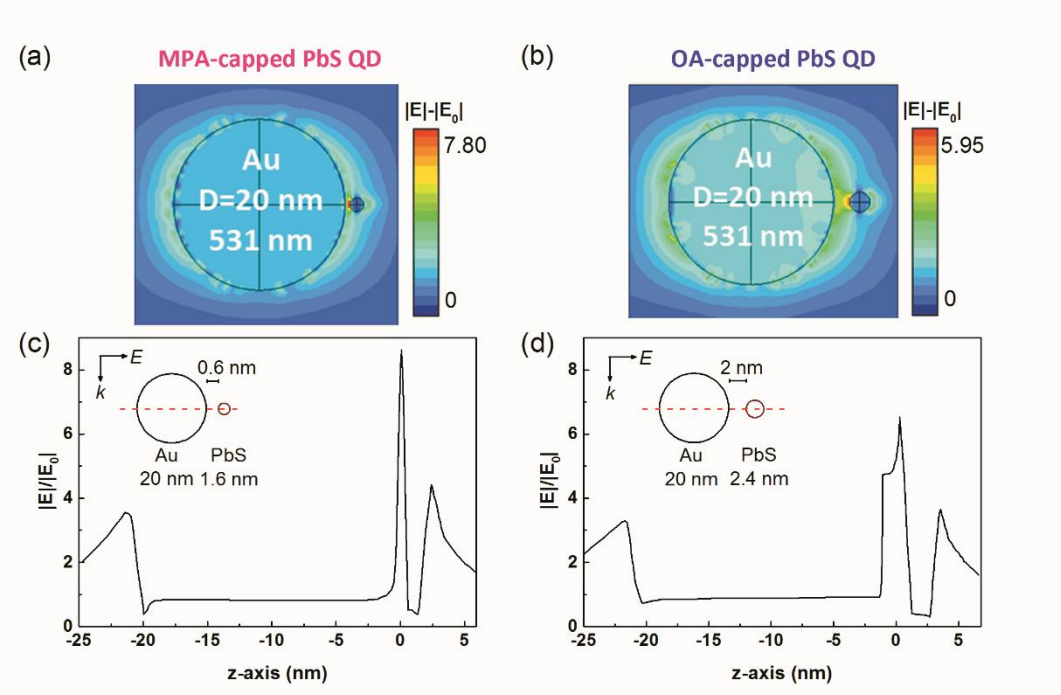

Figure 5.9. Wavelength-dependent maximum value of the electric field between the gap along the center line of the Au-PbS hetero-system. MPA-capped PbS QD (*d*=1.6 nm) was separated with 0.6 nm at the gap from Au (*D*=20 nm); and OA-capped PbS QD (*d*=2.4 nm) was separated with 2.0 nm at the gap at the from Au (*D*=20 nm).

5.4 Conclusion

The MPA-capped small PbS QDs coupled with Au NPs was observed to significantly enhance photo-current conversion efficiency compared with OA-capped large PbS QDs. The structure of a plasmon active Au NPs-modified TiO_2 electrode was optimized by covering a very TiO_2 thin layer prepared by the LPD method. Both strong quantum confinement and an enhanced electric field play a crucial role in the increased IPCE. For the former, excited electrons in small PbS QDs are more liable to be injected into the CB of TiO_2 because of the enlarged band gap; for the latter, small PbS QDs interact intensely with plasmonic Au NPs owing to the metallic properties of PbS with a high dielectric constant so that coupling takes place and the electric field induced by surface plasmon resonance is confined between the gap of Au NPs and PbS QDs, thus the enhanced near-field boosts to the efficiency of electron injection. The enhancement of the electric field accounts for both the distance between QDs and Au NP, as well as the average size of QDs. These results demonstrate the validity of plasmon enhancement on quantized particles at a relatively wide wavelength region between visible and near infrared. These findings pave a novel way to illuminate the mechanism of interaction between semiconductor QDs and metal NPs in the aspect of photoelectrical conversion.

References

1. Brongersma, M. L.; Halas, N. J.; Nordlander, P. *Nat Nano* **2015,** 10, (1), 25-34.
2. Prashant V. Kamat, K. T., David R. Baker, and James G. Radich. *Chem. Rev.* **2010,** 110, 6664–6688.
3. Gaoling Zhao I, H. K., Toshinobu Yoko. *Thin Solid Films* **1996,** 277, 147-154.
4. Nabika, H.; Takase, M.; Nagasawa, F.; Murakoshi, K. *The Journal of Physical Chemistry Letters* **2010,** 1, (16), 2470-2487.
5. Zhang, X.; Chen, Y. L.; Liu, R. S.; Tsai, D. P. *Reports on progress in physics. Physical Society* **2013,** 76, (4), 046401.
6. Kumar, J.; Wei, X.; Barrow, S.; Funston, A. M.; Thomas, K. G.; Mulvaney, P. *Physical Chemistry Chemical Physics* **2013,** 15, (12), 4258-4264.
7. Hines, M. A.; Scholes, G. D. *Advanced Materials* **2003,** 15, (21), 1844-1849.
8. Kawawaki, T.; Takahashi, Y.; Tatsuma, T. *The Journal of Physical Chemistry C* **2013,** 117, (11), 5901-5907.
9. Liu, Z.; Hou, W.; Pavaskar, P.; Aykol, M.; Cronin, S. B. *Nano letters* **2011,** 11, (3), 1111-1116.
10. Nishijima, Y.; Ueno, K.; Kotake, Y.; Murakoshi, K.; Inoue, H.; Misawa, H. *The Journal of Physical Chemistry Letters* **2012,** 3, (10), 1248-1252.
11. Xu, B.-B.; Wang, L.; Ma, Z.-C.; Zhang, R.; Chen, Q.-D.; Lv, C.; Han, B.; Xiao, X.-Z.; Zhang, X.-L.; Zhang, Y.-L.; Ueno, K.; Misawa, H.; Sun, H.-B. *ACS nano* **2014,** 8, (7), 6682-6692.
12. Lakowicz, J. R. *Analytical Biochemistry* **2005,** 337, (2), 171-194.

13. Takase, M.; Ajiki, H.; Mizumoto, Y.; Komeda, K.; Nara, M.; Nabika, H.; Yasuda, S.; Ishihara, H.; Murakoshi, K. *Nat Photon* **2013,** 7, (7), 550-554.
14. Nagasawa, F.; Takase, M.; Murakoshi, K. *The Journal of Physical Chemistry Letters* **2013,** 5, (1), 14-19.
15. WISE, F. W. *Acc. Chem. Res.* **2000,** 33, 733-780.
16. Berger, L. I., Chapter 12. Properties of Solids. In *CRC Handbook of Chemistry and Physics*, 90th ed.; W.M. Haynes, Ed. CRC Press: Boca Raton, FL, **2005**; pp 1-218.
17. Margaret A. Hines, G. D. S. *Advanced Materials* **2003,** 15, (1844-1849).
18. Akhtar, J.; Afzaal, M.; Vincent, M. A.; Burton, N. A.; Hillier, I. H.; O'Brien, P. *Chemical communications* **2011,** 47, (7), 1991-1993.
19. Zhang, J.; Gao, J.; Miller, E. M.; Luther, J. M.; Beard, M. C. *ACS nano* **2014,** 8, (1), 614-622.
20. Moreels, I.; Allan, G.; De Geyter, B.; Wirtz, L.; Delerue, C.; Hens, Z. *Physical Review B* **2010,** 81, (23).
21. Moreels, I.; Kruschke, D.; Glas, P.; Tomm, J. W. *Opt. Mater. Express* **2012,** 2, (5), 496-500.
22. Wang, J.; Mandelis, A.; Melnikov, A.; Hoogland, S.; Sargent, E. H. *The Journal of Physical Chemistry C* **2013,** 117, (44), 23333-23348.
23. Yue, F.; Tomm, J. W.; Kruschke, D. *Physical Review B* **2013,** 87, (19), 195314.
24. El-Ballouli, A. O.; Alarousu, E.; Bernardi, M.; Aly, S. M.; Lagrow, A. P.; Bakr, O. M.; Mohammed, O. F. *Journal of the American Chemical Society* **2014,** 136, (19), 6952-6959.
25. Knowles, K. E.; Malicki, M.; Weiss, E. A. *Journal of the American Chemical Society* **2012,** 134, (30), 12470-12473.
26. Haynes, C. L.; McFarland, A. D.; Smith, M. T.; Hulteen, J. C.; Van Duyne, R. P. *The Journal of Physical Chemistry B* **2002,** 106, (8), 1898-1902.
27. Templeton, A. C.; Pietron, J. J.; Murray, R. W.; Mulvaney, P. *The Journal of Physical Chemistry B* **2000,** 104, (3), 564-570.
28. Gesuele, F.; Sfeir, M. Y.; Koh, W. K.; Murray, C. B.; Heinz, T. F.; Wong, C. W. *Nano letters* **2011,** 12, (6), 2658-2664.
29. Yang, Y.; Rodríguez-Córdoba, W.; Lian, T. *Nano Letters* **2012,** 12, (8), 4235-4241.
30. El-Ballouli, A. a. O.; Alarousu, E.; Usman, A.; Pan, J.; Bakr, O. M.; Mohammed, O. F. *ACS Photonics* **2014,** 1, (3), 285-292.
31. Tang, J.; Kemp, K. W.; Hoogland, S.; Jeong, K. S.; Liu, H.; Levina, L.; Furukawa, M.; Wang, X.; Debnath, R.; Cha, D.; Chou, K. W.; Fischer, A.; Amassian, A.; Asbury, J. B.; Sargent, E. H. *Nature materials* **2011,** 10, (10), 765-771.
32. Patrick R. Brown, D. K., Richard R. Lunt, Ni Zhao, Moungi G. Bawendi, Jeffrey C. Grossman, and Vladimir Bulovi . *ACS nano* **2014,** 8, 5863 – 5872.
33. Fu, X.; Pan, Y.; Wang, X.; Lombardi, J. R. *The Journal of chemical physics* **2011,** 134, (2), 024707.
34. Antón, M. A.; Carreño, F.; Melle, S.; Calderón, O. G.; Cabrera-Granado, E.; Cox, J.; Singh, M. R. *Physical Review B* **2012,** 86, (15), 155305.
35. Hakami, J.; Wang, L.; Zubairy, M. S. *Physical Review A* **2014,** 89, (5).
36. Artuso, R. D.; Bryant, G. W. *Nano letters* **2008,** 8, (7), 2106-2111.
37. Wang, J.; Shan, Y.; Zhao, W.-W.; Xu, J.-J.; Chen, H.-Y. *Analytical Chemistry* **2011,** 83, (11), 4004-4011.
38. Jin, S.; DeMarco, E.; Pellin, M. J.; Farha, O. K.; Wiederrecht, G. P.; Hupp, J. T. *The Journal of Physical Chemistry Letters* **2013,** 4, (20), 3527-3533.
39. Honma, I.; Sano, T.; Komiyama, H. *The Journal of Physical Chemistry* **1993,** 97, (25), 6692-6695.
40. Anna Rumyantseva, S. K., Pierre-Michel Adam, Sergey V. Gaponenko , Svetlana V. Vaschenko, Olga S. Kulakovich, Andrey A. Ramanenka, Dmitry V. Guzatov, Dmytro Korbutyak, Volodymyr Dzhagan, Alexander

Stroyuk, and Vitaliy Shvalagin *ACS nano* **2013**, 130306134821001.

41. Savasta, S.; Saija, R.; Ridolfo, A.; Di Stefano, O.; Denti, P.; Borghese, F. *ACS nano* **2010,** 4, (11), 6369-6376.
42. Ray, P. C.; Fan, Z.; Crouch, R. A.; Sinha, S. S.; Pramanik, A. *Chemical Society Reviews* **2014,** 43, (17), 6370-6404.
43. Govorov, A. O.; Lee, J.; Kotov, N. A. *Physical Review B* **2007,** 76, (12), 125308.
44. Cushing, S. K.; Li, J.; Meng, F.; Senty, T. R.; Suri, S.; Zhi, M.; Li, M.; Bristow, A. D.; Wu, N. *Journal of the American Chemical Society* **2012,** 134, (36), 15033-15041.
45. Hutter, T.; Mahajan, S.; Elliott, S. R. *Journal of Raman Spectroscopy* **2013,** 44, (9), 1292-1298.
46. Kawawaki, T.; Tatsuma, T. *Physical Chemistry Chemical Physics* **2013,** 15, (46), 20247-20251.
47. Barceló, I.; Guillén, E.; Lana-Villarreal, T.; Gómez, R. *The Journal of Physical Chemistry C* **2013,** 117, (44), 22509-22517.
48. Kishimoto, H.; Takahama, K.; Hashimoto, N.; Aoi, Y.; Deki, S. *Journal of Materials Chemistry* **1998,** 8, (9), 2019-2024.
49. Deki, S.; Aoi, Y.; Asaoka, Y.; Kajinami, A.; Mizuhata, M. *Journal of Materials Chemistry* **1997,** 7, (5), 733-736.
50. Moreels, I.; Lambert, K.; Smeets, D.; De Muynck, D.; Nollet, T.; Martins, J. C.; Vanhaecke, F.; Vantomme, A.; Delerue, C.; Allan, G.; Hens, Z. *ACS Nano* **2009,** 3, (10), 3023-3030.
51. Jacek Jasieniak, * Marco Califano,‡ and Scott E.Watkins†. *ACS nano* **2011,** 5.
52. Beranek, R. *Advances in Physical Chemistry* **2011,** 2011.
53. Chakrapani, V.; Baker, D.; Kamat, P. V. *Journal of the American Chemical Society* **2011,** 133, (24), 9607-9615.
54. Hamadanian, M.; Reisi-Vanani, A.; Majedi, A. *Materials Chemistry and Physics* **2009,** 116, (2–3), 376-382.
55. Rockafellow, E. M.; Stewart, L. K.; Jenks, W. S. *Applied Catalysis B: Environmental* **2009,** 91, (1–2), 554-562.
56. Hardman, S. J. O.; Graham, D. M.; Stubbs, S. K.; Spencer, B. F.; Seddon, E. A.; Fung, H.-T.; Gardonio, S.; Sirotti, F.; Silly, M. G.; Akhtar, J.; O'Brien, P.; Binks, D. J.; Flavell, W. R. *Physical Chemistry Chemical Physics* **2011,** 13, (45), 20275-20283.
57. Okuhata, T.; Kobayashi, Y.; Nonoguchi, Y.; Kawai, T.; Tamai, N. *The Journal of Physical Chemistry C* **2015,** 119, (4), 2113-2120.
58. Halas, N. J.; Lal, S.; Chang, W.-S.; Link, S.; Nordlander, P. *Chemical Reviews* **2011,** 111, (6), 3913-3961.
59. Kobayashi, Y.; Nonoguchi, Y.; Wang, L.; Kawai, T.; Tamai, N. *The Journal of Physical Chemistry Letters* **2012,** 3, (9), 1111-1116.
60. Liu, Y.; Gibbs, M.; Puthussery, J.; Gaik, S.; Ihly, R.; Hillhouse, H. W.; Law, M. *Nano letters* **2010,** 10, (5), 1960-1969.

Appendix

A5.1 Photo-electrochemical measurement

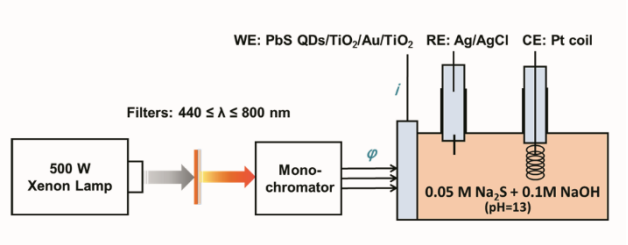

Figure A5.1. The photo-electrochemical measurement device.

A5.2 Extinction of PbS QDs sensitized plasmonic substrate

Extinction of PbS QDs sensitized plasmonic substrate was measured layer by layer. Gold presented plasmonic peak around wavelength of 570 nm, when covered with the 2nd TiO_2 layer, red-shift plasmon peak was observed because the dielectric constant of environment was increased by titanium dioxide.

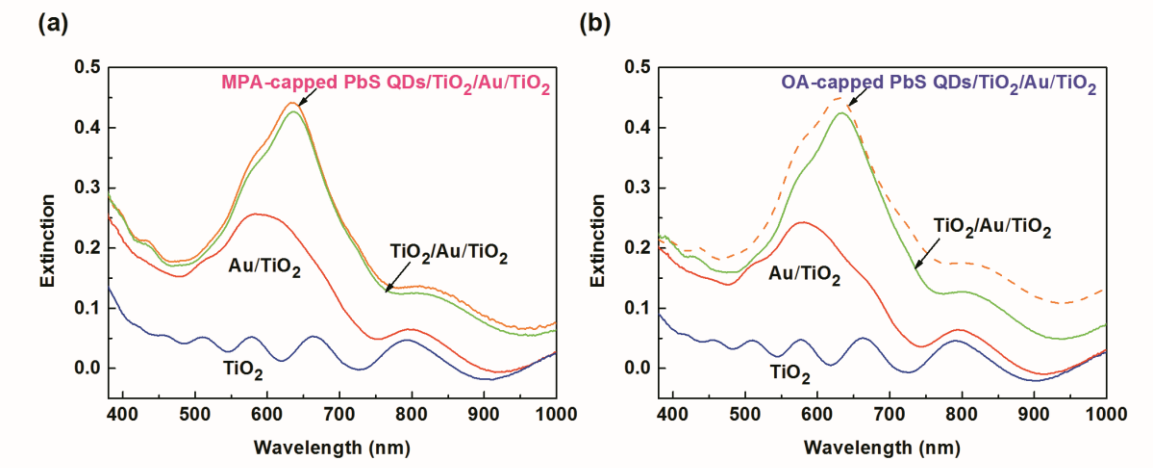

Figure A5.2. Extinction spectrum of (a) MPA- and (b) OA-capped PbS QDs sensitized substrate (PbS particle density: 1.2 x 10^{13} cm^{-2}; PbS mole number density: 0.82 and 2.77 $nmol/cm^{-2}$ for MPA- and OA-capped PbS QDs, respectively).

A5.3 Potential-dependent on-off action response

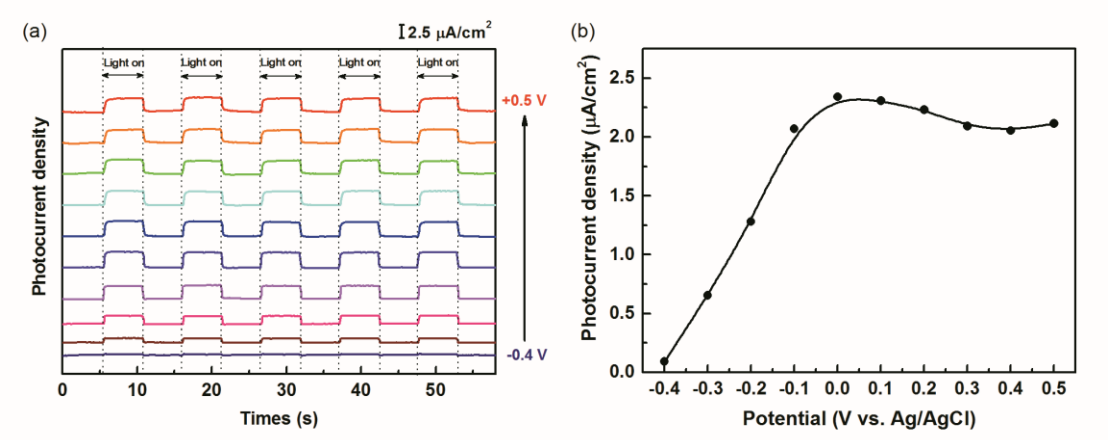

Figure A5.3. Potential-dependent (a) on-off action response of OA-capped PbS QDs/TiO_2 substrate, and (b) photocurrent density. Potential range: -0.4 ~ +0.5 V with 0.1 V interval (vs. Ag/AgCl sat.KCl), electrolyte: 0.05 M Na_2S+0.1 M NaOH, irradiation wavelength range: 540~800 nm, light intensity: 1.7 mW/cm^2, PbS particle density: 6 x 10^{15} cm^{-2}, PbS mole number density: 1.38 μmol/cm^{-2}.

A5.4 Cyclic voltammetry graph

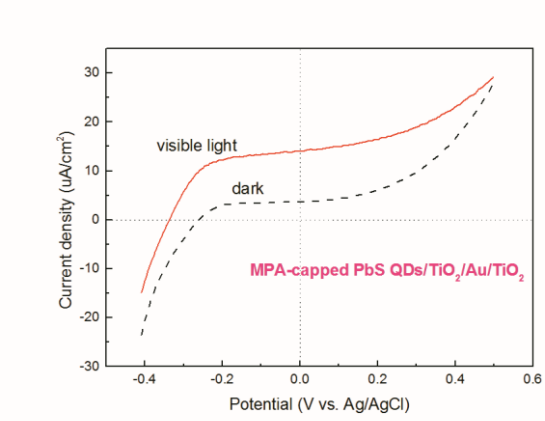

Figure A5.4. Comparison of I-V characteristics of MPA-capped PbS QDs sensitized TiO_2/Au/TiO_2 substrate in the dark (dark dash line) and under visible light with a wavelength above 380 nm with light intensity of 24.8 mW/cm^2 (red solid line) in aqueous electrolyte (0.05 M Na_2S in 0.1M NaOH) scanned at 50 mV/s in the anodic direction from -0.4 V to +0.5 V. PbS particle density: 7.2 x 10^{12} /cm^{-2}; PbS mole number density: 0.49 nmol/cm^{-2}.

Chapter 6

Enhanced Photoenergy Conversions using Size-Controlled PbS Quantum Dots by Highly Localized Electronic Excitation

6.1 Introduction

Colloid quantum dots (QDs) sensitized photocurrent generation system has attracted much attention for next photoenergy devices based on very unique the tunable electrical and optical properties controlled by size-dependent quantum confinement. Lead sulfide (PbS) QDs, for example, are of interest in solar applications owing to their small bandgap of 0.41 eV and large Bohr exciton radius of 18 nm, which together allow bandgap tuning over the full solar spectral range. Multiple exciton generation (MEG)[1-3] -related intrinsic properties of colloid PbS QDs with various sizes have been intensely studied on dynamic aspect including inter- or intraband relaxation processes of biexciton quantum yield[4, 5] or fluorescence blinking,[6, 7] Auger process[8] or Auger recombination,[9-12] phonon-assisted intraband relaxations,[13, 14] however, MEG-induced photoelectric conversion of PbS QDs has been limitedly reported to date and the apparent enhancement was generated only within ultraviolet or near-ultraviolet visible light range.[15] The benefit of the MEG excitation to produce relatively high density carriers also has not clarified yet.

Plasmonic photovoltaic devices based on noble metal nanoparticles (NPs) is alternative approach to advance the photoenergy conversion owing to highly localized surface plasmon resonance (LSPR). The localized near-field generated by Au NPs is able to be enhanced by well coupling with PbS QDs[16] and uplift the photoelectric conversion not only in near-infrared but in short visible light range.[17] Also, LSPR has been validated to modify the absorption of semiconductor nanostructures, such as breaking forbidden transitions between discrete quantum levels in a CdSe nanorods[18] and single-walled carbon nanotube.[19] As lead chalcogenides have distinct characteristics in symmetry breaking on the optical transitions based on quantum confinement[20] or hot electron-hole pair induced transient Stark effect,[21] it is rational to expect that the LSPR progress absorption of PbS QDs and consequently expand

photoelectrical response in a wavelength range with energy exceeding the threshold of MEG based on spatially localized high-dense excitation..

In this chapter, a novel system is created to reveal photo-electrochemical responses of size-controlled PbS QDs by coupling LSPR generated by Au NPs with more than two times of bandgap energy of QDs. Enhanced incident photon-current conversion efficiency at a wide wavelength region from near ultraviolet to near infrared demonstrates the validity of plasmon enhancement on the quantized particles with wide variety of sizes based on multiple exciton generation.

6.2 Experimental

6.2.1 Photo-Electrochemical Measurement

Incident photon to current efficiency (IPCE) spectra were measured using a three-electrode system. Illumination from an Xenon lamp (USHIO Spax Inc.) was cut off for visible light by using 350 and 800 nm filters (SCH-50s-44Y and CLDF-50s, SIGMA KOKI Co., Ltd.), and then passed through a grating monochromator (M10, Bunkoukeiki). A power meter (VEGA rohs, OPHIR PHOTONICS) was used to measure the incident power through the monochromator for the photocurrent measurement. Steady-state on-off photocurrent responses were monitored by shutter controller (SC10, THOR LABS) and were recorded with a potentiostat (HSV-110, Hokuto Denko) connected between a counter electrode of Pt coil and the working electrode in the electrolyte of 0.05 M Na_2S+ 0.1 M NaOH aqueous solution. Potentials were polarized from -0.5 to +0.5 V (against a Ag/AgCl (sat.KCl) reference electrode).

6.2.2 Calculation for IPCE and EF

The incident photon-current conversion efficiency (IPCE) of the PbS QDs sensitized substrates as a working electrode is calculated by the following formula, where I and φ are respectively the photocurrent density and power intensity density at a wavelength of λ.

$$\text{IPCE (\%)} = \frac{1240 \cdot I}{\lambda \cdot \varphi} \times 100$$

The enhancement factor (EF) was introduced. In the present experiment, as the loading amounts of PbS QDs both on the substrates with and without Au are carefully controlled to be the same, all of

$$\text{Enhancement Factor} = \frac{\text{IPCE}_{\lambda,\text{w/Au}}}{\text{IPCE}_{\lambda,\text{w/oAu}}}$$

6.3 Results and discussion

6.3.1 Comparison of enhanced IPCE spectra using distinct sizes of PbS QDs

The characteristics of the plasmonic enhancement at the visible wavelength region were compared using size-dependent colloid PbS QDs (Figure 6.1). Firstly, for TiO_2 substrate, all these three different size of QDs produce photocurrent response under visible light irradiation. Absorption of a photon with high energy more than a semiconductor's bandgap results in an electron and hole, each with excess kinetic energy above their respective band edge. When this initial excited electron has sufficient energy in excess of the bandgap energy, it is able to scatter with a valence band electron, boosting it across the bandgap to the conduction band to form a second electron-hole pair while relaxing back toward its conduction band edge (Figure 6.5b and c). This inverse Auger process is the so-called multiple exciton generation (MEG).[22] The energy threshold for MEG is based on momentum and energy conservation, but momentum conservation can be relaxed and yield lower threshold for relatively small QDs because of strong quantum confinement (for example, 2.6 E_g for PbS-1220 while 2.4 E_g for PbS-1140[12]). Here we roughly use an empirical threshold of 2.6 times of the bandgap energy for PbS QDs,[23] giving 4.42 eV (281 nm), 2.86 eV (434 nm), and 2.34 eV (530 nm) for OP-728, OP-1101 and OP-1344, respectively (marked in green areas, Figure 6.1). In this sense, the largest PbS QDs (OP-1344) with the smallest bandgap benefit from a lower MEG threshold within the visible light region compared to the middle-size QDs (OP-1101), and thus produce apparent photo-electrical response in this MEG region; in contrast, for the smallest QDs (OP-728), the threshold is in the ultraviolet region and only the strong quantum confinement improves the generation of photocurrent.

For PbS QDs-sensitized TiO_2/Au/TiO_2 substrate, PbS QDs generated great enhancement than the TiO_2 substrate in the localized surface plasmon resonance range of 1.8~2.5 eV (marked as yellow area).

Our previous work[17] has confirmed that dielectric PbS QDs are capable of enhancing the nearby electric field generated by Au NPs and consequently improving photoelectrical response across a wide visible light range. Enhancement factor (EF) was calculated as the IPCE ratio of the substrate with gold to the substrate without gold at a certain wavelength. Large EF was obtained in the LSPR region and size-dependent enhancement was observed. For example, at wavelength of 520 nm, EF is 3.1, 8.4 and 9.4 for OP-728, OP-1101 and OP-1344 respectively. Such difference is considered coming from size-dependent coupling between PbS QDs and LSPR. PbS QDs confine and enhance the near-field generated by LSPR in the gap between Au NPs (orange areas, Figure 6.5); and the larger the size, the greater the enhancement because of higher scattering efficiency.[16] Also, the near-field of a plasmonic Au NP can break forbidden transitions selection rules of semiconductor nanostructure and thus enhances absorption.[18] As LSPR enjoys a better overlap with $2E_g$ of OP-1344 and OP-1101 rather than OP-728, reasonably, modification in absorption by the enhanced near-filed is also expected especially for OP-1344 sensitized system (wide green arrows, Figure 6.5f).

Moreover, the overlap between MEG and LSPR region also benefits the large PbS QDs (OP-1344) of a higher enhancement. Efficient electron transfer must be appreciably faster than both the electronic relaxation time between the first two excited states ($1P_e$-$1S_e$) in PbS quantum dots as well as biexciton lifetime of Auger recombination in order to outpace the cooling process. Lifetime of electron transfer from excited PbS QDs into TiO_2 NPs has been estimated to be ~6 fs,[24] tremendously more rapid than 1.75 ps[13] for the intraband relaxation and 65 ps[10] for the Auger recombination of PbS QDs with a similar size as OP-1344, indicating multiple exciton can be collected on a faster time scale than exciton annihilation. Notably, when PbS QDs approach to Au NPs and give rise to enhanced near-field, all the dynamics processes will reasonably be modified, resulting in boosted electron injection[25] (widen orange, light orange and red arrows in Figure 6.5d, e and f) and manipulated multiexciton emission.[26] As the exact determination of absorption in PbS QDs not only from irradiation light within a single layer domain but also from excited LSPR is fairly a challenge, unfortunately, the corresponding absorbed photon–to–current efficiency (APCE) was hardly evaluated in the present.

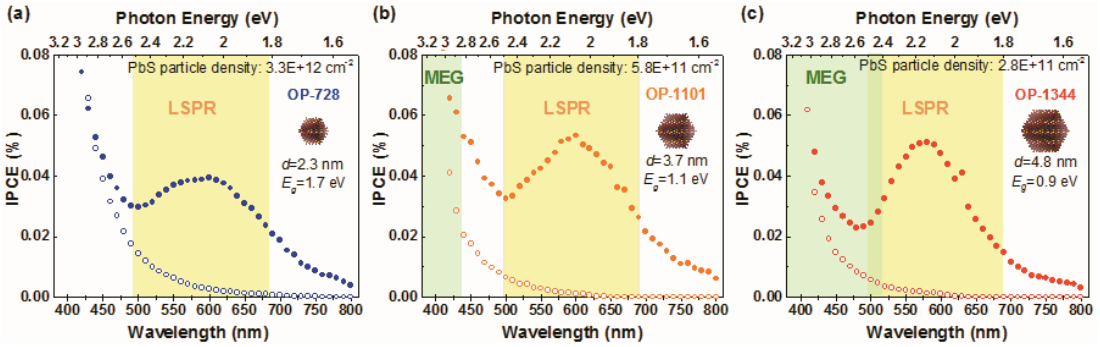

Figure 6.1. IPCE comparison of (a) OP-728, (b) OP-1101 and (c) OP-1344 PbS QDs sensitized TiO_2 and TiO_2/Au/TiO_2 substrates measured at -0.1 V in electolyte of 0.05 M Na_2S+0.1 M NaOH. PbS particle densities within a single layer domain are 3.3 x 10^{12}, 5.8 x 10^{11} and 2.8 x 10^{11} cm^{-2}, respectively. The mole number density of PbS is around 0.5 nmol/ cm^{-2} for all.

Further examinations were performed to evaluate the coupling effect by Au NPs with increasing loading amounts PbS QDs by measuring the enhanced IPCE of TiO_2/Au/TiO_2 and TiO_2 substrates (Figure A6.1) and the resulted EF (Figure 6.2). As the quantity of PbS QDs increased up to a loading of 1.1 x 10^{13}, 2.3 x 10^{12} and 1.1 x 10^{12} cm^{-2} respectively for OP-728, OP-1101 and OP-1344 on both TiO_2/Au/TiO_2 and TiO_2 substrates, the IPCE increased as a whole over the observed wavelength region. The IPCE increment of TiO_2/Au/TiO_2 in the LSPR wavelength region first kept increasing then presented saturated (Figure A6.1); and the EF first increased then declined with a raising loading amount (Figure 6.2), suggesting a low loading amount improve the coupling between PbS QDs with Au NPs. The maximum of EF was obtained as 15, 59 and 47 for OP-728, OP-1101 and OP-1344 at 600 nm, respectively, with PbS QDs density of 3.3 x 10^{12}, 5.8 x 10^{11} and 2.8 x 10^{11} cm^{-2} (the mole number density of PbS is all around 0.5 nmol/ cm^{-2}). Considering the numbers of PbS moles covering the flat substrate with close-packing a single layer of 9.3 x 10^{13}, 3.4 x 10^{13} and 2.0 x 10^{13} cm^{-2}, roughly 20% coverage of PbS QDs is appropriate to prepare the plasmon-enhanced photocurrent generation system. This best coverage is consistent to our previous report.[17] The reason that a sparse QDs distribution improve the enhancement was ascribed to distance-dependent plasmon coupling.[27] As increasing the loading amount, a monolayer distribution becomes difficult due to the roughness of the surface (SEM images in Chapter 2) so that multilayer is sensibly inevitable, which means the piled up PbS QDs cannot well couple with Au NP with a distance exceeding the LSPR effective spatial region.

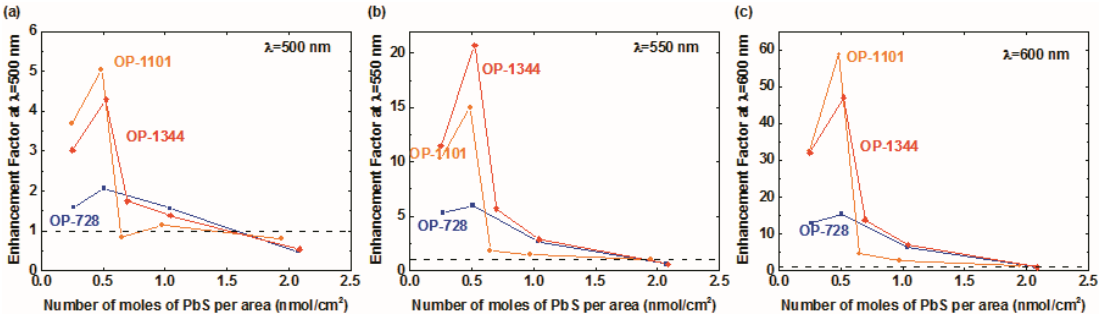

Figure 6.2. Comparison of loading amount dependent enhancement factor of PbS QDs at different wavelength light irradiation of (a) 500 nm, (b) 550 nm and (c) 600 nm.

6.3.2 Wavelength-dependent output power density

In order to thoroughly compare the size-induced coupling effect, further assessments were executed by measuring collected photocurrents under various polarized potentials. Figure 6.3 shows the collected photocurrent densities of OP-728, OP-1101 and OP-1344 sensitized TiO_2 and plasmonic substrates measured under polarized potential from -0.8 to 0.5 V (vs. Ag/AgCl) with light irradiation of 550 nm . As potential polarized to positive direction, significant photocurrent density (J) increased from zero then presented a saturated tendency, regardless of QDs' size, irradiation wavelength or whether coupling with Au NPs. The Fermi level controlled by polarized potential play an essential role in charge separation and recombination of PbS QDs sensitized system. In the inverse potential region more negative than the flat band position of TiO_2 (cal. U_{FB}=−0.7 V in electrolyte with pH=13), the recombination of excited electron-hole pairs is promoted (Figure 6.5, grey arrows), leading to the inhibition of electron injection collected as photocurrent; on the contrary, as the Fermi level is downshifted in the potential region more positive than U_{FB}, the Potential gradient in TiO_2 is enlarged (Figure 6.5), benefiting the electron injection into TiO_2 and restricting the recombination. When the competition between injection and recombination processes achieve a balance, basically unchanged photocurrents are collected.

Compared to the other two PbS QDs, OP-1344 sensitized TiO_2 produced a relatively fast balance within 0.2 V (potential interval between the saturated potential of -0.3 V and the onset potential of photocurrent collection at -0.5 V) (Figure A6.3 and Table A6.1). One possible explanation is the dynamic aspect, as has been mentioned above, that electron transfer is adequately fast than hot carriers

cooling so that hot electrons created by excitation with light energy exceeding the bandgap are able to be injected into TiO_2 from higher energy level (orange arrows, Figure 6.5) without relaxing into the bottom of CB. Such effect is more noteworthy for OP-1344 because the relatively smaller E_g and slower intraband cooling rate[12, 13] as a result of the comparatively weaker Coulomb interaction induced in larger size. Another conceivable account is the apprent dissimilarity for the promotion of MEG, for example at the excitation wavelength of 450 nm (2.76 eV) with the energy critical for OP-1101 (2.45 E_g) but sufficient large for OP-1344 (2.99 E_g) to generate multiexcitons (Figure 6.5b and c), meaning that it is OP-1344 rather than OP-1101 that prefer a surge of electron injection at excitation wavelength below 550 nm (red narrows in Figure 6.5b and c).

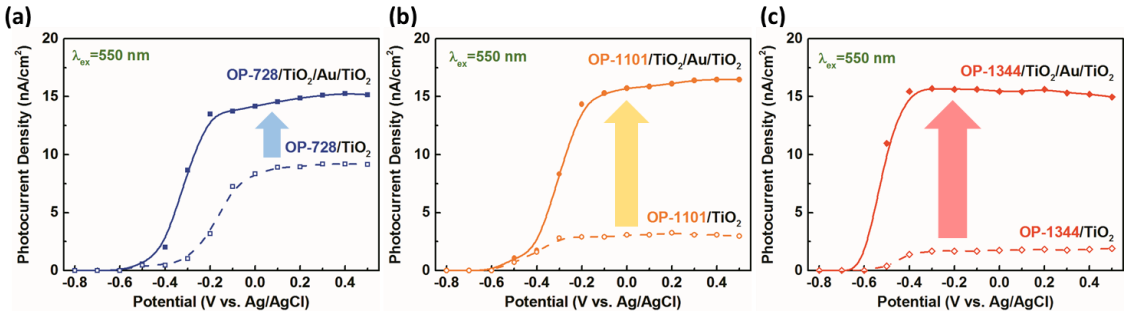

Figure 6.3. Comparison of *J-V* characteristics of (a, d) OP-728, (b, e) OP-1101 and (c, f) OP-1344 PbS QDs sensitized TiO_2 (dashed line and hollow symbols) and TiO_2/Au/TiO_2 (solid line and solid symbols) substrates scanned from negative to positive potential in electolyte of 0.05 M Na_2S+0.1 M NaOH at irradiation of 550 nm. PbS particle densities within a single layer domain are 1.7 x 10^{12}, 2.9 x 10^{11} and 1.3 x 10^{11} cm^{-2}, respectively. The mole number density of PbS is all around 0.25 nmol/ cm^{-2}. Photocurrent density was normalized according to irradiating light intensity.

In the case of PbS QDs-Au NPs coupling system, enhanced photocurrent were collected within the LSPR region (500 ~700 nm) for all the PbS QDs unrelated to the size diversity, validating that LSPR undeniably modify election injection and enhance photocurrent collection of PbS QDs sensitized photoelectrochemical cell. What is worthy to be noticed is that the balance between charge separation and recombination was promoted to be attained by coupling OP-1344 with Au NPs, within 0.1 V (potential interval between the saturated potential of -0.4 V and the onset potential of photocurrent collection at -0.5 V). Such phenomenon indicates that LSPR assisted MEG manipulate the absorption and efficiently improve photoelectric conversion response of the well-coupled system.

Further comparison of size-dependent *J-V* characteristics was performed by evaluating the yielded power density, which was calculated as simple area integral of photocurrent density across the whole potential region from -0.8 to +0.5 V (Figure A6.4) based on *J-V* curve evaluation for a two-electrode system. A typical comparison at excitation wavelength of 550 nm is presented in Figure 6.4a, illustrating the apparent obtainment of output power density by OP-1344 coupled Au NPs system with 16.54 nW · cm^{-2}, larger than 12.76 and 13.78 nW · cm^{-2} by OP-728 and OP-1101, respectively, as summarized in Table 6.1. The relationship between output power density and excitation wavelength presented in Figure 6.4b demonstrates distinct enhancement by OP-1344 in the plasmonic wavelength range. Enhancement factor (EF_{power}) presents the calculated output power density ratio across the whole potential range, giving increment as excitation in the high wavelength region owing to the LSPR.

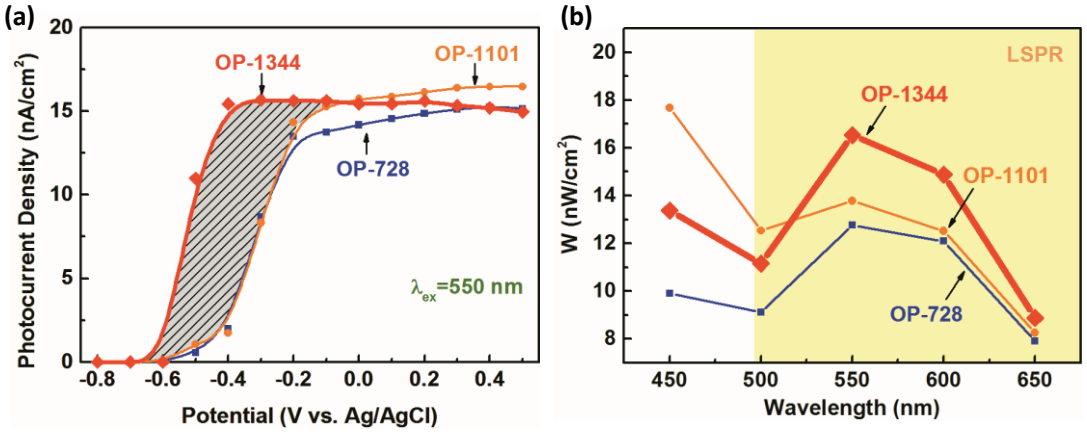

Figure 6.4. (a) *J-V* characteristics of size-dependent PbS QDs-sensitized plasmonic electrode irradiated by visible light with wavelength of 550 nm. Grey area presents the enhanced output power density by OP-1344. (b) Wavelength-dependent output power density (*W*) of size-controlled PbS QDs-sensitized TiO_2/Au/TiO_2 electrode.

Table.6.1. Calculated power density of size-dependent PbS QDs-sensitized electrodes irradiated by various wavelengths

PbS QDs	λ_{ex} (nm)	Power density (JV in nW・cm^{-2})		EF_{power}
		TiO_2	TiO_2/Au/TiO_2	
OP-728	450	10.15	9.91	1
	500	7.41	9.12	1.2
	550	6.60	12.76	1.9
	600	3.64	12.09	3.3
	650	1.91	7.91	4.1
OP-1101	450	8.51	17.68	2.1
	500	4.17	12.53	3.0
	550	1.76	13.78	7.8
	600	0.589	12.52	21.3
	650	0.235	8.26	35.1
OP-1344	450	15.96	13.37	0.8
	500	7.68	11.15	1.5
	550	3.19	16.54	5.2
	600	1.03	14.88	14.4
	650	0.38	8.87	23.3

Power density was simply calculated by the area integral of photocurrent density at each potential (see Figure A6.4 in Appendix). EF_{power} presents the calculated power density ratio across the whole potential region from -0.8 to +0.5 V.

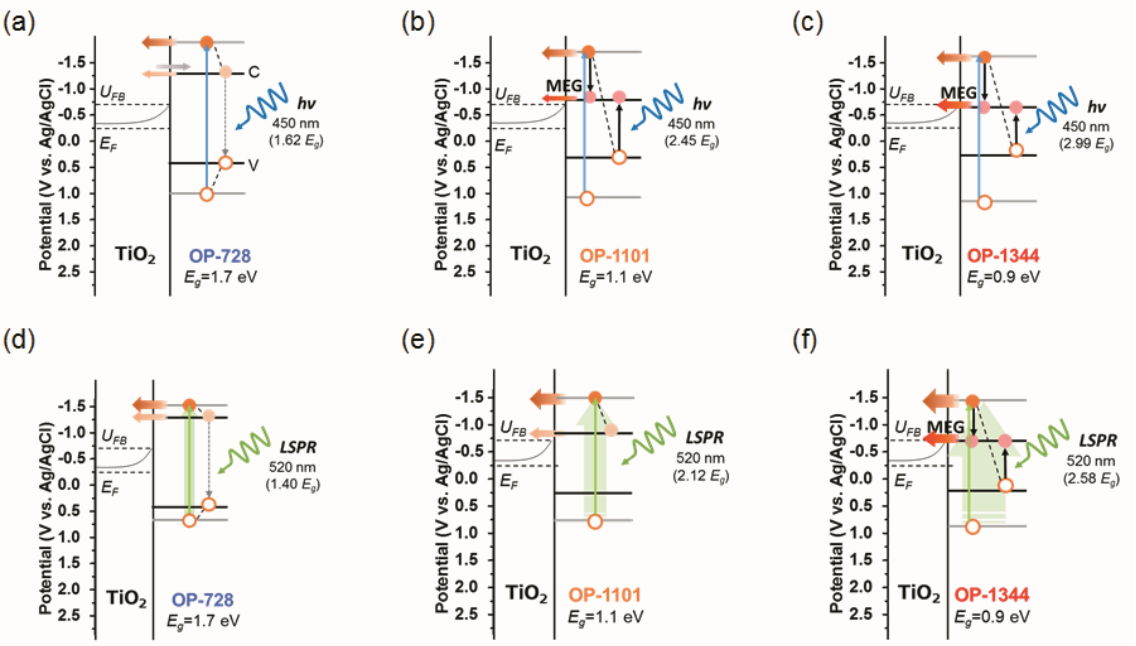

Figure 6.5. Schematic illustration of size-dependent PbS QDs sensitized bare TiO_2 under excitation of 450 nm (a, b and c) and TiO_2/Au/TiO_2 under LSPR excitation of 520 nm (d, e and f). Excitation by blue (450 nm, 2.76 eV, blue solid arrows) or green (520 nm, 2.38 eV, green solid arrows) visible light generated hot electrons (filled orange circles) and holes (empty orange circles) at higher energy levels (grey lines) than conduction band (labeled C) or valence band (labeled V). Cooled electrons (filled light orange circles) or holes relaxed to CB or VB via intraband relaxation (dashed lines) and a fraction undergo MEG (b, OP-1101 at 450 nm; c and f, OP-1344 at 450 and 520 nm; black arrows) to create biexciton (filled pink circles). Hot electron injection into TiO_2 from higher energy level without

intraband relaxation (orange arrows), cooled electron injection from conduction band (light orange arrows), bi-electron injection via MEG from conduction band (red arrows) and electron-hole pair recombination (grey thick arrow and grey dotted arrows). The existence of Au NPs (d, e and f, yellow areas) generate near-field by LSPR under excitation of 520 nm. PbS QDs confine and enhance the near-field in the gap between Au NPs (orange areas); the larger the size, the greater the enhancement because of higher scattering efficiency. The enhanced near-filed manipulate QDs' absorption (wide green arrows) and facilitate electron injection (widen orange, light orange and red arrows).

6.4 Conclusions

In summary, size-controlled PbS QDs with bandgap energy from infrared to visible light were utilized to sensitize plasmonic photoelectrochemical cell. Enhanced photoelectrical conversion efficiency was observed by coupling PbS QDs with Au NPs. Relatively large size of PbS QDs-sensitized plasmonic electrode produced higher enhancement across a wide wavelength range and produced a larger output power density based on *J-V* characteristics, which is ascribed to both the modified absorption by the enhanced electromagnetic field generated by the LSPR. The shift of the onset potential of the photocurrent can be induced by enhanced high-density carrier injection owing to multiple exciton generation in the LSPR wavelength region. It is predicted therefore that the current functional QDs-based plasmonic photoelectrochemical cell will be the subject of future investigations on effective energy conversion materials involving multiple exciton generation.

References

1. Sukhovatkin, V.; Hinds, S.; Brzozowski, L.; Sargent, E. H. *Science* **2009,** 324, (5934), 1542-1544.
2. Semonin, O. E.; Luther, J. M.; Choi, S.; Chen, H.-Y.; Gao, J.; Nozik, A. J.; Beard, M. C. *Science* **2011,** 334, (6062), 1530-1533.
3. Yuan, M.; Liu, M.; Sargent, E. H. *Nature Energy* **2016,** 1, 16016.
4. Gesuele, F.; Sfeir, M. Y.; Koh, W. K.; Murray, C. B.; Heinz, T. F.; Wong, C. W. *Nano Letters* **2012,** 12, (6), 2658-2664.
5. Choi, Y.; Sim, S.; Lim, S. C.; Lee, Y. H.; Choi, H. *Scientific Reports* **2013,** 3, 3206.
6. Maturova, K.; Nanayakkara, S. U.; Luther, J. M.; van de Lagemaat, J. *Nano Letters* **2013,** 13, (6), 2338-2345.
7. Correa, R. E.; Dauler, E. A.; Nair, G.; Pan, S. H.; Rosenberg, D.; Kerman, A. J.; Molnar, R. J.; Hu, X.; Marsili, F.; Anant, V.; Berggren, K. K.; Bawendi, M. G. *Nano Letters* **2012,** 12, (6), 2953-2958.
8. Geiregat, P.; Houtepen, A.; Justo, Y.; Grozema, F. C.; Van Thourhout, D.; Hens, Z. *The Journal of Physical Chemistry C* **2014,** 118, (38), 22284-22290.
9. Padilha, L. A.; Stewart, J. T.; Sandberg, R. L.; Bae, W. K.; Koh, W.-K.; Pietryga, J. M.; Klimov, V. I. *Accounts of*

Chemical Research **2013,** 46, (6), 1261-1269.

10. Stewart, J. T.; Padilha, L. A.; Qazilbash, M. M.; Pietryga, J. M.; Midgett, A. G.; Luther, J. M.; Beard, M. C.; Nozik, A. J.; Klimov, V. I. *Nano Letters* **2012,** 12, (2), 622-628.
11. Midgett, A. G.; Luther, J. M.; Stewart, J. T.; Smith, D. K.; Padilha, L. A.; Klimov, V. I.; Nozik, A. J.; Beard, M. C. *Nano Letters* **2013,** 13, (7), 3078-3085.
12. Nootz, G.; Padilha, L. A.; Levina, L.; Sukhovatkin, V.; Webster, S.; Brzozowski, L.; Sargent, E. H.; Hagan, D. J.; Van Stryland, E. W. *Physical Review B* **2011,** 83, (15), 155302.
13. El-Ballouli, A. a. O.; Alarousu, E.; Usman, A.; Pan, J.; Bakr, O. M.; Mohammed, O. F. *ACS Photonics* **2014,** 1, (3), 285-292.
14. Geiregat, P.; Delerue, C.; Justo, Y.; Aerts, M.; Spoor, F.; Van Thourhout, D.; Siebbeles, L. D. A.; Allan, G.; Houtepen, A. J.; Hens, Z. *ACS Nano* **2015,** 9, (1), 778-788.
15. Sambur, J. B.; Novet, T.; Parkinson, B. A. *Science* **2010,** 330, (6000), 63-66.
16. Hutter, T.; Mahajan, S.; Elliott, S. R. *Journal of Raman Spectroscopy* **2013,** 44, (9), 1292-1298.
17. Li, X.; Suzuki, K.; Toda, T.; Yasuda, S.; Murakoshi, K. *The Journal of Physical Chemistry C* **2015,** 119, (38), 22092-22101.
18. Jain, P. K.; Ghosh, D.; Baer, R.; Rabani, E.; Alivisatos, A. P. *Proceedings of the National Academy of Sciences* **2012,** 109, (21), 8016-8019.
19. Takase, M.; Ajiki, H.; Mizumoto, Y.; Komeda, K.; Nara, M.; Nabika, H.; Yasuda, S.; Ishihara, H.; Murakoshi, K. *Nat Photon* **2013,** 7, (7), 550-554.
20. Nootz, G.; Padilha, L. A.; Olszak, P. D.; Webster, S.; Hagan, D. J.; Van Stryland, E. W.; Levina, L.; Sukhovatkin, V.; Brzozowski, L.; Sargent, E. H. *Nano Letters* **2010,** 10, (9), 3577-3582.
21. Trinh, M. T.; Sfeir, M. Y.; Choi, J. J.; Owen, J. S.; Zhu, X. *Nano Letters* **2013,** 13, (12), 6091-6097.
22. Beard, M. C.; Ellingson, R. J. *Laser & Photonics Reviews* **2008,** 2, (5), 377-399.
23. Hardman, S. J. O.; Graham, D. M.; Stubbs, S. K.; Spencer, B. F.; Seddon, E. A.; Fung, H.-T.; Gardonio, S.; Sirotti, F.; Silly, M. G.; Akhtar, J.; O'Brien, P.; Binks, D. J.; Flavell, W. R. *Physical Chemistry Chemical Physics* **2011,** 13, (45), 20275-20283.
24. Yang, Y.; Rodríguez-Córdoba, W.; Xiang, X.; Lian, T. *Nano Letters* **2012,** 12, (1), 303-309.
25. Atwater, H. A.; Polman, A. *Nat Mater* **2010,** 9, (3), 205-213.
26. Park, Y.-S.; Ghosh, Y.; Xu, P.; Mack, N. H.; Wang, H.-L.; Hollingsworth, J. A.; Htoon, H. *The Journal of Physical Chemistry Letters* **2013,** 4, (9), 1465-1470.
27. Kawawaki, T.; Takahashi, Y.; Tatsuma, T. *The Journal of Physical Chemistry C* **2013,** 117, (11), 5901-5907.

Appendix

A6.1 IPCE and EF changes depending on the amount of PbS QDs loading

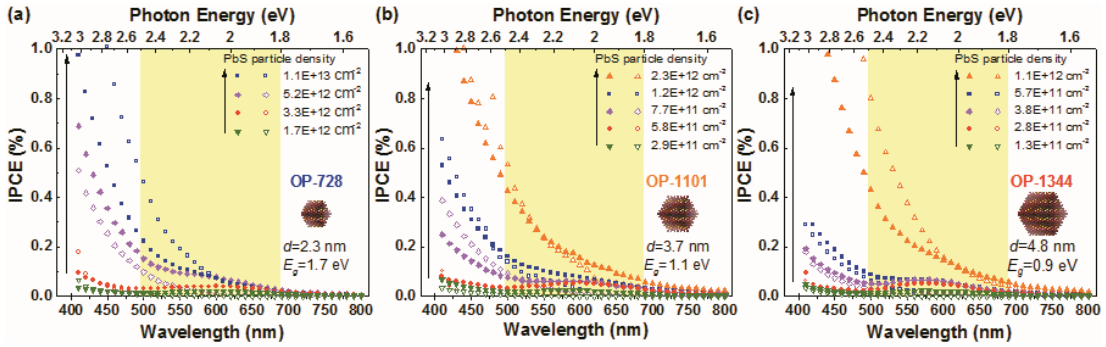

Figure A6.1. Comparison of IPCE changes depending on the loading amount of (a) OP-728, (b) OP-1101 and (c) OP-1344 sensitized TiO_2 (hollow scatter) and TiO_2/Au/TiO_2 (solid scatter) measured at -0.1 V in electolyte of 0.05 M Na_2S+0.1 M NaOH.

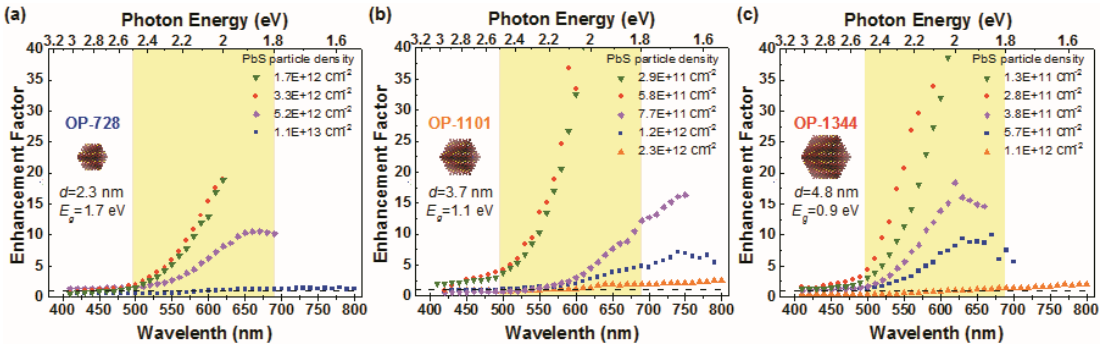

Figure A6.2. Comparison of enhancement factor changes depending on the loading amount of (a) OP-728, (b) OP-1101 and (c) OP-1344 measured at -0.1 V in electolyte of 0.05 M Na_2S+0.1 M NaOH.

A6.2 Potential-dependent collected photocurrent density

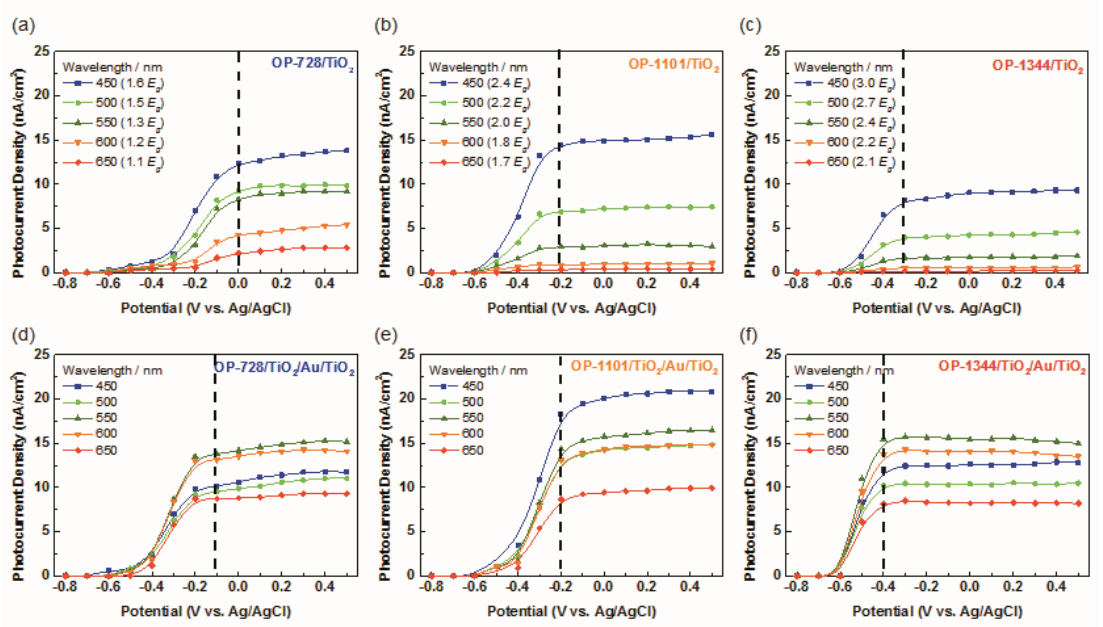

Figure A6.3. Comparison of *J-V* characteristics of (a, d) OP-728, (b, e) OP-1101 and (c, f) OP-1344 PbS QDs sensitized TiO_2 and TiO_2/Au/TiO_2 substrates scanned from negative to positive potential in electolyte of 0.05 M Na_2S+0.1 M NaOH at different wavelength light irradiation. Dashed lines present the saturated potential, V_{sat}. PbS particle densities within a single layer domain are 1.7 x 10^{12}, 2.9 x 10^{11} and 1.3 x 10^{11} cm^{-2}, respectively. The mole number density of PbS is all around 0.25 nmol/ cm^{-2}. Photocurrent density was normalized according to irradiating light intensity.

Table A6.1. Size-dependent onset, saturated potential and their difference of PbS QDs-sensitizedTiO_2 and TiO_2/Au/TiO_2 (V vs. Ag/AgCl)

PbS QDs	TiO_2			TiO_2/Au/TiO_2		
	V_{onset}	V_{sat}	V_{dif}	V_{onset}	V_{sat}	V_{dif}
OP-728	-0.6	-0.1	0.5	-0.6	-0.2	0.4
OP-1101	-0.5	-0.2	0.3	-0.5	-0.2	0.3
OP-1344	-0.5	-0.3	0.2	-0.5	-0.4	0.1

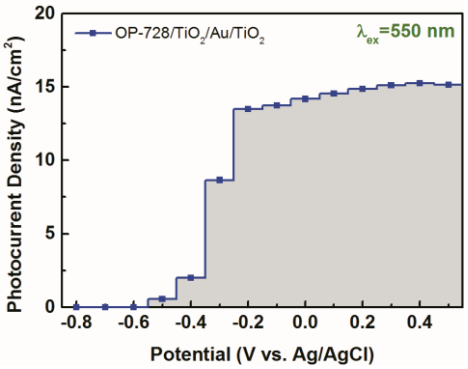

Figure A6.4. Calculated power density as the area integral of photocurrent density at each potential (grey area).

A6.3 Extinction spectra with increasing Loading amount

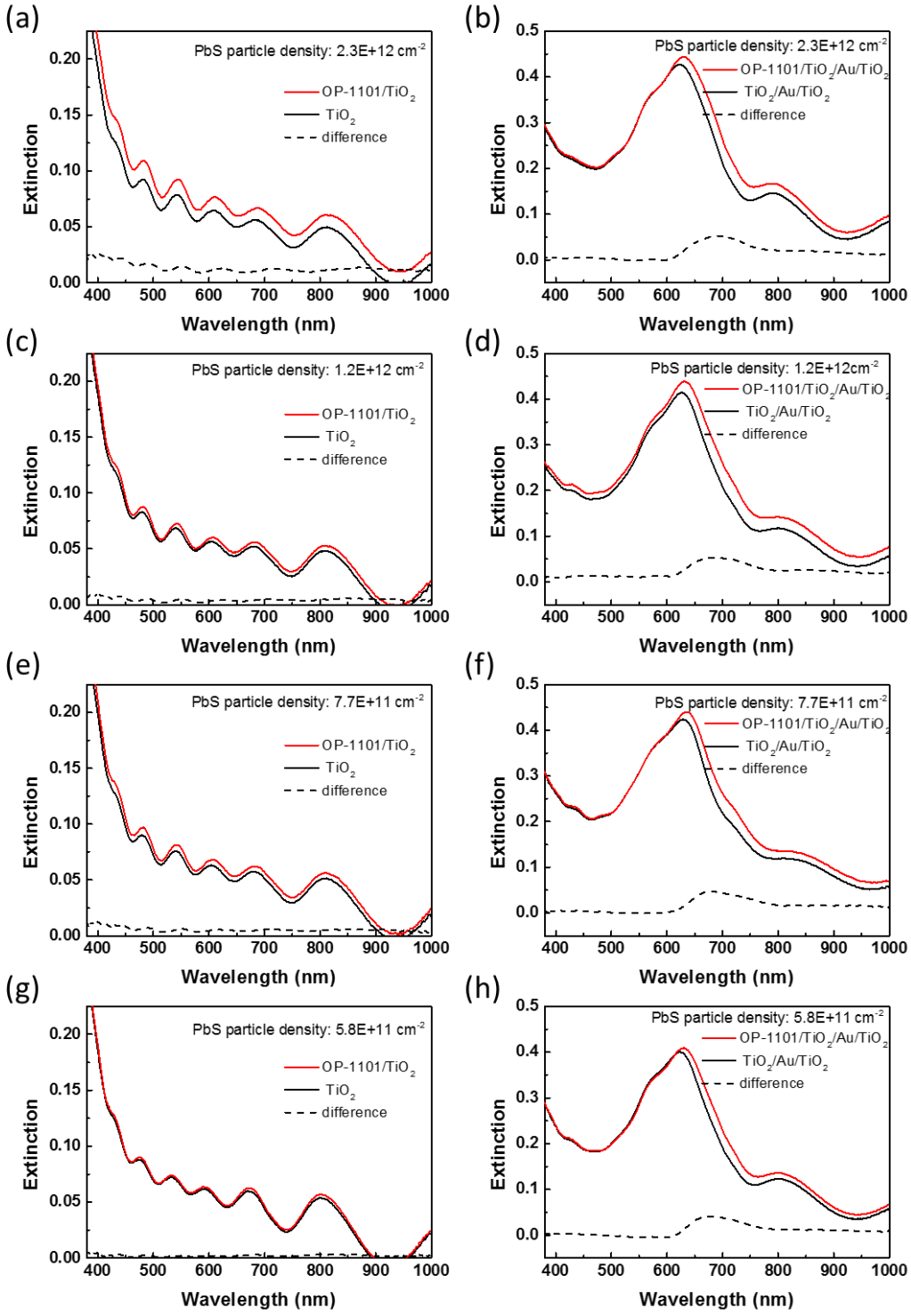

Figure A6.5. Extinction spectra of OP-1101 sensitized (left column) TiO_2 and (right column) $TiO_2/Au/TiO_2$ with increasing loading amount.

Chapter 7

Improved Interaction via Formation of Strong Coupling between Size and Shape-Controlled PbS Quantum Dots and Au Nanostructures

7.1 Introduction

Light–matter interactions can be split into two principal regimes, the weak-coupling and the strong coupling regime. Strong coupling occurs when the emitter–photon interaction becomes larger than the combined atomic dipole decay rate and the cavity field decay rate.[1-3] Then a coherent periodic energy exchange between the emitter and the photon in the form of Rabi oscillations replace the irreversible spontaneous emission process of the emitter, resulting in spectroscopic anti-crossings between the atom-like emitter and cavity-mode dispersion relations and is characterized by the vacuum Rabi splitting.[4]

The strong interaction of quantum emitters with surface plasmon resonance is of fundamental interest for understanding light matter interactions. Plasmonic nanostructures hold the promise of attaining the strong coupling regime as the resonance energy is able to be simply tuned by designing the shape or size of noble metal structure.[5] Recent experiments revealed strong coupling between individual plasmonic structures and multiple organic molecules[6-10] or quantized semiconductor nanostructure.[11-16] A “bowtie” shaped antenna, where two metallic triangles facing tip-to tip are separated by a small gap, produces a large electromagnetic field confined to the area near the gap as “hot spots”, which enable to detect molecules by surface-enhanced Raman scattering (SERS),[17] to evaluate enhanced fluorescence decay,[18] and to reveal Fano resonance line shape in optical spectrum.[19]

In this chapter, PbS QDs was drop-casted onto the surface of Au bowtie nanostructures which were designed in diverse size and resonance energy by electron beam lithography, then the substrate was measured by dark-field scattering spectrum and image mapping. Split scattering peaks with energy difference up to 300 meV were observed for the coupling system, demonstrating the plasmon-QDs interaction present strong coupled characteristics.

7.2 Experimental

7.2.1 Electron Beam Lithography and Fabrication of Gold Bowties.

Prior to fabrication, ITO glass (thickness of 150 ± 20 nm, sheet resistance ≦ 15 Ω/sq, surface roughness Ra < 1 nm, Kuramoto Co., Ltd) were well cleaned sequentially with trichloroethylene in ultrasonic for 10 min, 50 ºC of acetone water bath for 10 min, and ozone aching for 20 min. Then resist solution (ZEON, ZEP520A:ZEPA = 2:1) was spin-coated on the well-washed ITO substrate at a speed of 4000 rpm for 60 sec, followed by baking at 150°C on a hotplate for 3 min. The coated glasses were loaded into an electron beam lithography system (ELS-F125, Elionix Inc.) and was exposed to define the shape of bowties with the beam current of 50 pA and the dose energy of 750 μC cm^{-2}. The design consisted of matrices of bowties, with each matrix hosting 108 bowties. Each bowtie was separated by 5 μm from its neighboring partner to guarantee no interaction. The substrates were developed by immersing into the solution of ZED-N50 for 60 sec and ZMD-B for 10 sec, respectively. The substrate was deposited with a 30 nm adhesion layer of Au by utilizing helicon sputtering (MPS-4000C1/HC1, ULVAC), followed by immersion in solution of ZDMAC and acetone under ultrasonic to remove unnecessary metal layer. The morphology of the Au bowties was measured by a SEM (ERIONIX ELS-F125) using a 125 kV electron beam with a magnification of 200,000x.

7.2.2 Sensitization of PbS QDs:

OP-682 (1^{st} exciton peak of 682 nm) hexane diluted solution was drop-casted onto Au bowtie/ITO substrate to cover 2 cm^2 square substrate. PbS particle number density was calculated to be 1.52E+13 cm^{-2} approaching a single layer.

7.2.3 Dark-field Microspectroscopy

Scattering spectra of every single bowtie with and without QDs were measured with an inverted microscope (OLYMPUS IX-71) equipped with a dark field condenser (U-UCD 8-2), a top lens (NA=0.9, U-TLD), an objective lens (60x, NA=0.70, WD=0.1-1.3 mm, LUCPlanFLN), a polarizer (U-UCD 8-2) and a halogen lamp (IX-HLSH1000, OLYMPUS). A spectrograph with a grating of 150 g/mm, BLZ=800 (ISOPlane SCT-320, Princeton Instruments) and a CCD camera were used to disperse scattered photons and register spectrum. Spectrum of each Au bowtie nanostructure was recorded one by one under exposure of 10 s with a slit width of 5 μm. Image of all the nanostructures was captured under exposure of 1 s with a slit width of 50 μm.

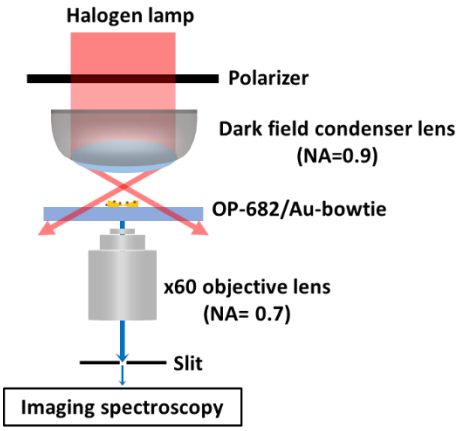

Figure 7.1 Schematic of the scattering spectrum and imaging measurement

7.3 Results and discussion

Scattering spectrum and image of every single bowtie was measured by dark field microspectroscopy. Figure 7.2 shows the image mapping of all the Au bowties as designed, showing increased scattering intensity as the side length (L) of bowtie increased. Deposition a great amount of PbS QDs by drop casting forms areas of varying thickness with stacks as the solvent evaporates, so that the random

stacks on the bowtie surface or near the structure hinder the observation.

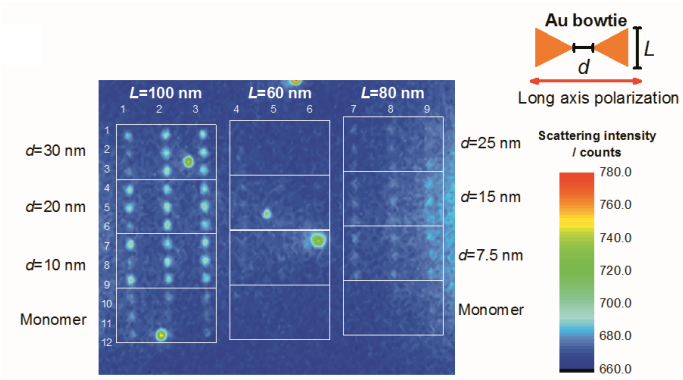

Figure 7.2. Scattering image of Au bowtie arrays with parallel polarization of the bowtie structure under light exposure of 1s and slit of 50 μm.

The scattering spectrum of a typical Au bowtie (Figure 7.3, orange; #37 in Figure 7.2) demonstrates the bowtie possesses a longitudinal bright mode at ≈ 1.75 eV (orange dashed line in Figure 7.3a) owing to dipolar coupling of the two parts of each bowtie.[20] The exciton energy of PbS QDs (Figure 7.3, navy dashed line) demonstrate that the optical transition of the QDs is in resonance with the plasmon excitations of the bowties. Strong coupling between PbS QDs and the localized surface plasmon create two separated scattering peaks (Figure 7.3, black) characterized as hybridized states of typical Rabi splitting with the energy of 290 meV (Figure 7.3b). Scattering spectra of Au bowties with tuned gaps were given in Figure S7.1, showing red-shifted longitudinal dipolar bright mode as the gap is decreased owing to strengthened dipolar interaction.[21] Strong coupling was also observed for bowties with different gaps or side lengths (Figure A7.2). Apparent dependence on the Rabi splitting energy observed in distinct bow tie structures reflect coupling strength determined by the cavity volume of LSPR and the oscillator strength of the exciton of PbS QDs. Smaller gap distance provides smaller cavity volume to interact with the PbS excitons, leading to the strong coupling state with higher Rabi splitting. Changes in the number of PbS QDs could also contribute to the change in the coupling energy. Further control of the deposition of PbS QDs or divergence between bowties even with the same

designing parameters could lead to higher energy in the Rabi splitting.

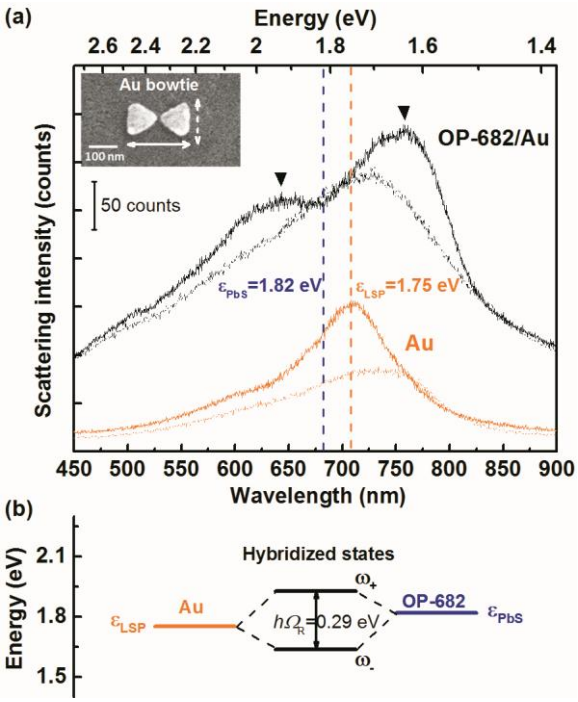

Figure 7.3. Strong coupling of plasmon and quantum emitters. (a) Scattering spectrum of Au bowtie nanostructure with side length of 100 nm and gap of 10 nm (column 3 row 7 in Figure 7.2) before (orange) and after the deposition of OP-682 (black) under parallel (solid line) and perpendicular (dotted line) polarization with light exposure of 10 s and a slit of 5 μm; fluorescence spectrum of OP-682 on ITO glass (navy) PbS particle density: 2.4 x 10^{12} cm^{-2}. Inset is the SEM image of the bowtie nanostructure with magnification of 200,000x. The dashed lines present the scattering maximum of Au bowtie (orange) and the emission maximum of PbS QDs (navy), respectively. (b) Energy scheme of strong coupling system of PbS QDs and Au bowtie, which form hybridized states with Rabi splitting energy of 0.29 eV.

7.4 Conclusion

A system that PbS QDs coupled to Au bowtie nanostructures were fabricated by utilizing electron beam lithography to form various size of Au nano-bowties. Size-dependence LSPR was confirmed by dark-field scattering spectrum at room temperature. The plasmon-QDs interaction present strong coupling when the LSPR approximate to the fluorescence maximum of PbS QD. Rabi splitting was observed with energy difference close to 300 meV, demonstrating the novel system of PbS QDs strongly coupled with plasmons. Extended photon absorption bands produce by the coupling will provide novel routes for effective photoenergy conversions.

References

1. Chance, R. R.; Prock, A.; Silbey, R. *The Journal of Chemical Physics* **1974,** 60, (7), 2744-2748.
2. Gersten, J.; Nitzan, A. *The Journal of Chemical Physics* **1981,** 75, (3), 1139-1152.
3. Drexhage, K. H.; Kuhn, H.; Schäfer, F. P. *Berichte der Bunsengesellschaft für physikalische Chemie* **1968,** 72, (2), 329-329.
4. Tame, M. S.; McEnery, K. R.; Ozdemir, S. K.; Lee, J.; Maier, S. A.; Kim, M. S. *Nat Phys* **2013,** 9, (6), 329-340.
5. Törmä, P.; Barnes, W. L. *Reports on Progress in Physics* **2015,** 78, (1), 013901.
6. Vasa, P.; Wang, W.; Pomraenke, R.; Lammers, M.; Maiuri, M.; Manzoni, C.; Cerullo, G.; Lienau, C. *Nat Photon* **2013,** 7, (2), 128-132.
7. Nagasawa, F.; Takase, M.; Murakoshi, K. *The Journal of Physical Chemistry Letters* **2014,** 5, (1), 14-19.
8. Koh, A. L.; Fernández-Domínguez, A. I.; McComb, D. W.; Maier, S. A.; Yang, J. K. W. *Nano Letters* **2011,** 11, (3), 1323-1330.
9. Hutchison, J. A.; Schwartz, T.; Genet, C.; Devaux, E.; Ebbesen, T. W. *Angewandte Chemie International Edition* **2012,** 51, (7), 1592-1596.
10. Schwartz, T.; Hutchison, J. A.; Genet, C.; Ebbesen, T. W. *Physical Review Letters* **2011,** 106, (19), 196405.
11. Bellessa, J.; Symonds, C.; Laverdant, J.; Benoit, J.-M.; Plenet, J. C.; Vignoli, S. *Electronics* **2014,** 3, (2), 303.
12. Bellessa, J.; Bonnand, C.; Plenet, J. C.; Mugnier, J. *Physical Review Letters* **2004,** 93, (3), 036404.
13. Reithmaier, J. P.; Sek, G.; Loffler, A.; Hofmann, C.; Kuhn, S.; Reitzenstein, S.; Keldysh, L. V.; Kulakovskii, V. D.; Reinecke, T. L.; Forchel, A. *Nature* **2004,** 432, (7014), 197-200.
14. Andersen, M. L.; Stobbe, S.; Sorensen, A. S.; Lodahl, P. *Nat Phys* **2011,** 7, (3), 215-218.
15. Kotni Santhosh, O. B., Lev Chuntonov, Gilad Haran. *Nature Communications* **2016,** in press.
16. Ming-Jay, Y.; Na Young, K.; Yoshihisa, Y.; Neil, N. *New Journal of Physics* **2015,** 17, (2), 023064.
17. Hatab, N. A.; Hsueh, C.-H.; Gaddis, A. L.; Retterer, S. T.; Li, J.-H.; Eres, G.; Zhang, Z.; Gu, B. *Nano Letters* **2010,** 10, (12), 4952-4955.
18. Lu, G.; Li, W.; Zhang, T.; Yue, S.; Liu, J.; Hou, L.; Li, Z.; Gong, Q. *ACS Nano* **2012,** 6, (2), 1438-1448.
19. Lee, B.; Park, J.; Han, G. H.; Ee, H.-S.; Naylor, C. H.; Liu, W.; Johnson, A. T. C.; Agarwal, R. *Nano Letters* **2015,** 15, (5), 3646-3653.
20. Duan, H.; Fernández-Domínguez, A. I.; Bosman, M.; Maier, S. A.; Yang, J. K. W. *Nano Letters* **2012,** 12, (3), 1683-1689.
21. Fromm, D. P.; Sundaramurthy, A.; Schuck, P. J.; Kino, G.; Moerner, W. E. *Nano Letters* **2004,** 4, (5), 957-961.

Appendix

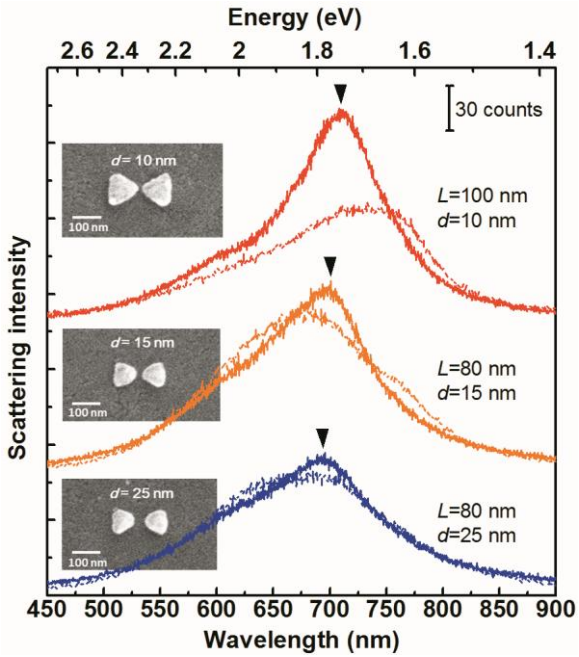

Figure A7.1. Scattering spectra of Au bowtie structures (*L*= 100 nm, *d*=10 nm (red), *L*= 80 nm, *d*=10 nm (orange), and *L*= 80 nm, *d*=25 nm (blue)). Polarization angles of incident light to the long axis of the dimers (solid lines) and the short axis of the dimers (dashed lines). Black inverted triangles show LSP resonance energy when incident light was illuminated parallel to the dimer axis. Insets are SEM image with magnification of 200,000x.

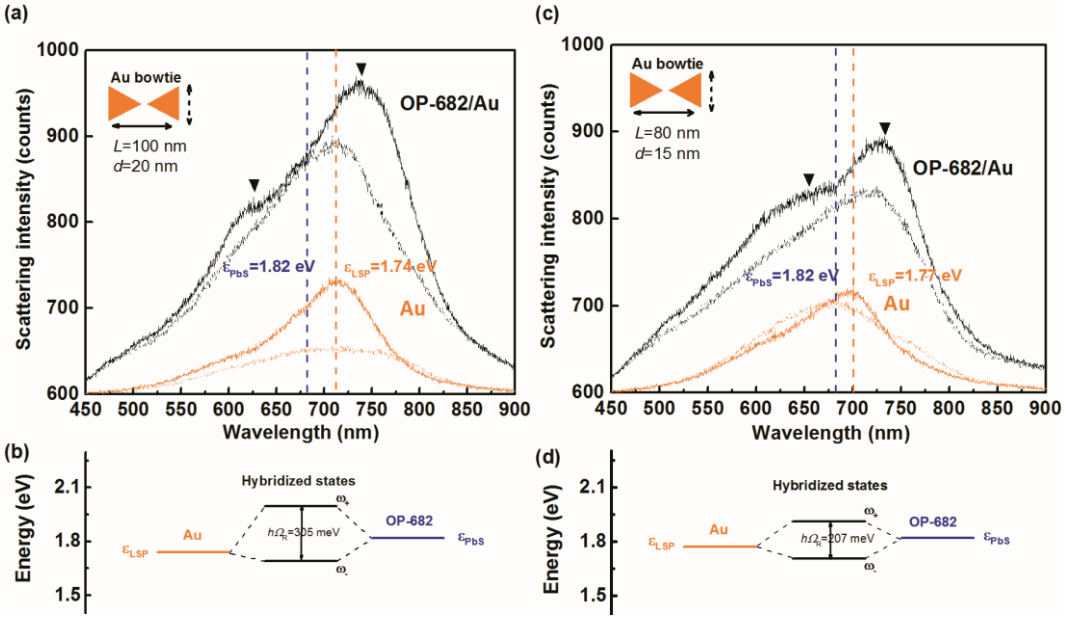

Figure A7.3. Strong coupling of PbS QDs and Au bowties with parameters of (a) *L*=100, *d*=20 and (c) *L*=100, *d*=20 and energy scheme of the corresponding Rabi splitting energy of (b) 305 and (d) 207 meV, respectively.

Chapter 8

General Conclusion

In this thesis, plasmonic gold nanostructures with controlled size and shape were well designed to couple with lead sulfide quantum dots (PbS QDs) varied in size and bandgap energy from near infrared to visible light. In Chapter 2, optical and electronic properties of size-controlled PbS QDs were characterized. The plasmonic photoelectrochemical cell with size-controlled PbS QDs were also characterized by SEM-EDS, absorption and emission spectroscopy. Photoluminescence of PbS QDs sensitized TiO_2/Au/TiO_2 present both plasmon enhancement and quenching effect compared to PbS QDs/TiO_2. Electrochemical luminescence of OP-1101 and OP-682 on TiO_2/Au/TiO_2 show apparent potential-dependent photoluminescence and simultaneous photocurrent, confirming that LSPR enhanced exciton generation and modified recombination. The variation of the Fermi level controlled by the electrode potential resulted in the charge separation efficiency, leading to the change in the efficiency of electron-hole separation and recombination in PbS QDs. The potential dependence provide the information on the band diagram of PbS QD/TiO_2 interface predicted by the optical and electronic properties of size-controlled PbS QDs in solutions. Fluorescence imaging of OP-682/TiO_2/Au/TiO_2 present the potential-dependent alternation of photoluminescence showing inhomogeneous distribution.

In Chapter 3, highly arrayed Au nanodimer was fabricated by angle-resolved nanosphere lithography (AR-NSL) as the detection matrix of surface-enhanced Raman spectroscopy. Size-controlled OP-728, OP-750 and OP-1101 was respectively sensitized for the Au-NSL substrate and the capping ligand of oleic acid (OA) with distinct vibrational spectrum was characterized owing to the enhanced near-field by coupling PbS QDs with Au NPs. The binding mode between oxygen atom of carboxylate head and Pb atoms was determined as bridging bidentate for all PbS QDs varied in size according to Raman shift of the anti- and symmetric stretching of COO^-. Shifted LO phonon mode of PbS QDs was observed because of relaxation of q=0 selection rule by phonon confinement. Potential-dependent variations of vibrational modes were investigated and explained by considering the electron transfer and static Coulomb interaction between OA molecule and Au surface. The FDTD simulation

indicates electromagnetic mechanism plays significant role in the enhancement.

In Chapter 4, simultaneous electrochemical surface-enhanced Raman scattering and photoelectric response measurement was utilized to reveal electron-hole pair separation of OP-1344/TiO_2/Au/TiO_2 electrode in electrolyte containing sulfide redox couple (S^{2-}/S_n^{2-}). Raman intensity of polysulfur vibrations and photocurrent were observed at the positive polarization, because the variation in the Fermi level controlled by potential altered the potential gradient in TiO_2 and subsequently influences the efficiency of electron-hole separation in PbS QDs. Effective hole scavenging from PbS QDs by S^{2-} at the interfaces was successfully monitored by the present method.

In Chapter 5, the surface modification of long-chain molecules OA surrounding OP-750 was exchanged into short-chain molecules of 3-mercaptopropionic acid (MPA), and the ligand exchange process was found to reduce the core size of QDs via the absorption spectrum (MP-537). These two different size of PbS QDs with designed loading amounts were respectively deposited on TiO_2 and TiO_2/Au/TiO_2 substrates, then their photoelectric response under visible light irradiation were measured by three-electrode photo-electrochemical system. Significantly enhanced photocurrent conversion efficiency was obtained by MP-537 rather than OP-750 both in the plasmonic wavelength range as well as in near-UV range, owing to metallic resonance induced by strong quantum confinement and the enhanced electric field.

In Chapter 6, OP-728, OP-1101 and OP-1344 was respectively sensitized for the TiO_2/Au/TiO_2 solar cell, enhanced photoelectrical conversion efficiency was observed across a wide wavelength range and distinct output power was attained by the largest QDs (OP-1344) than the other two sizes of PbS QDs, although OP-1344 present the weakest quantum confinement with almost equal conduction band positions compared with TiO_2. The remarkable shift of the onset potential of the photocurrent can be induced by enhanced high-density carrier injection owing to multiple exciton generation in the LSPR wavelength region.

In Chapter 7, a system that OP-682 coupled to Au nano-bowties, which were fabricated by electron beam lithography, was constructed and measured by dark-field scattering spectrum. The QDs-plasmon interaction behave strong coupling when the LSPR approximate to the fluorescence maximum of PbS QDs, forming hybridized states characterized as Rabi splitting.

This thesis demonstrates the validity of integrating PbS QDs and LSPR of Au nanostructures to control the interaction between photons and electrons. The LSPR played a crucial role in enhancing photoelectric conversion and output power by modifying the absorption and exciting MEG, and therefore could provide insights in further developments of the charge separation processes to exceed the Schottky-Queisser limit of semiconductor QDs,

Acknowledgements

I'd like to offer my sincerest gratitude to my supervisor, Prof. Kei Murakoshi, who has been a pillar of support during the period of my studies in Japan and has provided many opportunities to broaden my horizons. His wisdom, knowledge, inspiration and patience has been crucial to getting me through my PhD.

Many thanks to Associate Prof. Satoshi Yasuda and Assistant Prof. Hiro Minamimoto for their expert guidance, without which I would face many difficulties in conference presentation. The early years working with Ryo Futashima, Kentaro Suzuki and Takahiro Toda allowed me to explore the field of surface plasmon and photoelectric conversion, without which Chapter 5, 6 and my first publication would be very different. Takahito Yoshii has been very supportive for my measurements by surface-enhanced Raman scattering, without which Chapter 3 and 4 could be impossible. Atsuyori Ohnuki has shared much experience about fluorescence, dark field scattering and imaging without which I would not have been able to do chapter 2 and 7. I'd like to express my thanks to Prof. Yasuchika Hasegawa, Assistant Prof. Takayuki Nakanishi and Dr. Junseob Lee for the aid of guidance and equipment, without which near infrared fluorescence could not be characterized.

A big thank goes to Prof. Paul O'Brien and Dr. Paul McNaughter for their collaboration on the QDs synthesis as well as the plentiful support for the exhausting "crazy characterization" via SEM-EDS during my short visit to the University of Manchester. A lot of thanks to Ghulam Murtaza, my generous landlord in Manchester, and his friends who shared delicious Pakistan foods and happy time with me. Many thanks also AGS office for the funding provision for my visits to United Kingdom and the Netherlands, as well as MEXT for the scholarship supporting my 3-year overseas study in Japan, which provide so many opportunities to let me enjoy diverse cultures and landscapes.

The good advice and support from our secretary, Rumi Akiyama, and all colleagues in Physical Chemistry Laboratory have been invaluable on both the personal and academic levels, for which I am extremely grateful. In my first year, I'm very fortunate to have had the support from Dr. Jian Hu and his wife Wen Mao, without them I would be fairly struggling both for experiments and abroad life. In every situation over the years, Hua Li, Ruiting Li, Liyan Lou and Yang Bai have known exactly what to say to me to keep me going. All the way through the PhD, Dr. Yuanyuan Kang has been a good friend to sharing experience with me. In the months writing in the office, Jinjiang Zhang and Dr. Ruifeng Zhou, both arrived in the lab in my last year, are the best companion with whom I shared and enjoyed conversations.

None of this would have been possible without the ongoing support of my mum and my husband, who have endured more than should be reasonably expected with my emotions, long working hours, and in later years, lack of communication.